ROBOTIC ANTENNA METROLOGY RANGE CALIBRATION, UNCERTAINTY EVALUATION, AND SCAN GENERATION TO IMPROVE PERFORMANCE AND FLEXIBILITY

by

Benjamin L. Moser

© **Copyright by Benjamin L. Moser, 2023**

All Rights Reserved

A thesis submitted to the Faculty and the Board of Trustees of the Colorado School of Mines in partial fulfillment of the requirements for the degree of Doctor of Philosophy (Mechanical Engineering).

Golden, Colorado

Date _____

Signed: _____

Benjamin L. Moser

Signed: _____

Dr. Andrew J. Petruska
Thesis Advisor

Golden, Colorado

Date _____

Signed: _____

Dr. Carl Frick
Department of Mechanical Engineering
Department of Mechanical Engineering

ABSTRACT

Robotic positioning systems have recently been introduced in state-of-the-art antenna ranges for use during antenna metrology, a process with rigorous performance requirements to produce accurate field strength and polarization measurements. However, existing implementations rely on expensive and view-limited positional feedback systems, contain poorly defined pose (end effector position and rotation) uncertainties with impacts to final scan quality, and fail to fully utilize the motion capabilities of the robots by directly replicate the scanning motions of traditional antenna positioning systems with few degrees-of-freedom. These current constraints on robotic antenna ranges limit their adoption and flexibility. To enhance robotic antenna range performance and flexibility, we developed kinematics software and algorithms oriented toward high-DoF, multi-robot antenna range cells performing relative positioning tasks. We demonstrate the ability to reproduce the transforms of canonical scans, although antenna scanning with the implementation of these methods has not yet been evaluated due to current equipment limitations.

The purpose of this work was to (1) establish and experimentally verify calibration approaches for the manipulator types found in current robotic antenna ranges, (2) characterize the post-calibration pose uncertainty of these manipulators, and (3) implement a framework for efficient antenna scan generation that incorporates secondary objectives. Through two experimental studies on a high-precision 7 DoF hybrid robotic configuration for high-frequency (80 GHz- 500 GHz) antenna scanning, we demonstrated improvements in positioning accuracy for complex manipulators and generated post-calibration pose uncertainty estimates with a parameterized measurement uncertainty fit. Pose error reductions of 46.7% and 67.2% from the un-calibrated experimental manipulator model were found in the first and second study, respectively. Jacobians and uncertainty models were incorporated into an inverse kinematics pipeline to generate a variety of canonical scan types using full manipulator motion and simulate scan motion. This approach permits larger scan geometries to be performed when compared to an existing implementation, typified by spherical scan geometry expanded from a maximum radius of $1\,m$ to a $4\,m$. Secondary objectives are minimized in a hierarchical manner, with joint excursion reduced by an average of 34.6%. The produced scans offered improved performance for maximum scan geometry and joint excursion when compared to existing implementation. These studies collectively advance the state-of-the-art of antenna metrology by enhancing multi-arm robotic positioning systems at the National Institute of Standards and Technology (NIST) and supports NIST's mission to provide traceable antenna calibration services for all sectors in the United States.

TABLE OF CONTENTS

ABSTRACT . . . iii

LIST OF FIGURES . . . ix

LIST OF TABLES . . . xii

LIST OF ABBREVIATIONS . . . xiii

ACKNOWLEDGMENTS . . . xiv

DEDICATION . . . xv

CHAPTER 1 INTRODUCTION . . . 1

1.1 Robotic Antenna Ranges: State-of-the-Art Implementations . . . 3

1.2 Kinematic Modelling & Calibration . . . 4

1.3 Pose Uncertainty . . . 6

1.4 Pose Selection & Path Planning . . . 7

1.5 Synopsis & Purpose . . . 8

CHAPTER 2 UNIFIED PARAMETERIZATION AND CALIBRATION OF SERIAL, PARALLEL, AND HYBRID MANIPULATORS . . . 9

2.1 Abstract . . . 9

2.2 Introduction . . . 9

2.3 Materials and Methods . . . 14

2.3.1 Calibration Methodology Overview . . . 14

2.3.2 Pose-Error Minimization Framework . . . 14

2.3.2.1 Objective and Error Formulation . . . 14

2.3.2.2 Jacobian Packing . . . 15

2.3.2.3 Parameter Update . . . 16

2.3.3 Parallel Manipulator Parameterization and Kinematics . . . 17

2.3.3.1 Serial Chain Parameterization . . . 17

2.3.3.2 Forward Kinematics . . . 18

2.3.3.3 Inverse Kinematics . . . 19
2.3.4 Parallel Manipulator Calibration . . . 22
2.3.4.1 Jacobian Packing . . . 22
2.3.4.2 Constraint Matrix Construction . . . 23
2.3.4.3 Pose-by-Pose Jacobian Generation . . . 24
2.3.5 Pose Uncertainty Estimation . . . 26
2.3.6 Dependence on Data Set Size . . . 27
2.3.6.1 Expected Jacobians . . . 27
2.3.6.2 Covariance Component Evolution . . . 28
2.3.6.3 Estimated Data Set Size . . . 29
2.4 Experimental Evaluations . . . 30
2.4.1 Simulated Hybrid Manipulator Description . . . 30
2.4.1.1 Kinematic Model and Parameter Identification . . . 30
2.4.2 Simulated Pose Data . . . 31
2.4.2.1 Measurement Uncertainty . . . 31
2.4.2.2 Impact of Data Set Size on Pose Uncertainty . . . 31
2.4.3 Simulated Hybrid Manipulator Calibration . . . 32
2.4.4 Experimental Manipulator Description . . . 34
2.4.4.1 Encoder Information . . . 34
2.4.4.2 Identification of Coordinate Systems . . . 35
2.4.4.3 Kinematic Model and Parameter Identification . . . 36
2.4.5 Experimental Pose Data Collection . . . 37
2.4.5.1 Frame Reconstruction and Uncertainty . . . 38
2.4.6 Experimental Hybrid Manipulator Calibration . . . 39
2.4.7 Comparison to Alternate Calibration Methods . . . 40
2.5 Discussion . . . 41
2.5.1 Alternate Calibration Methods . . . 41

2.5.2 Application Overview . . . 42
2.5.3 Uncertainty Conclusions . . . 43
2.5.4 Future Work . . . 43
2.6 Conclusions . . . 44
2.7 Point-Quaternion Links . . . 44
2.8 Supplementary Case Study Information . . . 45
CHAPTER 3 CALIBRATING UNCERTAINTY IN ROBOT KINEMATICS AND POSE MEASUREMENTS WITH EXPECTATION-MAXIMIZATION . . . 48
3.1 Abstract . . . 48
3.2 Introduction . . . 48
3.3 Methods . . . 51
3.3.1 Uncertainty Propagation . . . 51
3.3.2 Data Acquisition and Processing . . . 51
3.3.2.1 Direct Drive Laser Tracker Kinematics . . . 51
3.3.2.2 Point Bundles . . . 53
3.3.3 Frame Generation and Covariance . . . 53
3.3.3.1 Point Bundle Residuals . . . 53
3.3.4 Expectation-Maximization Algorithm . . . 54
3.3.4.1 Expectation - Uncertainty-Weighted Kinematic Calibration . . . 54
3.3.4.2 Maximization - Covariance Estimation . . . 55
3.4 Studies . . . 57
3.4.1 System Configuration . . . 57
3.4.1.1 Robotic Manipulator . . . 57
3.4.1.2 Metrology Instruments and Configuration . . . 58
3.4.1.3 Coordinate Systems . . . 58
3.4.1.4 Target Poses . . . 58
3.4.2 Simulated Study . . . 59
3.4.2.1 Uncertainties . . . 59

3.4.2.2 Fitting Results . . . 59
3.4.3 Experimental Study . . . 60
3.4.3.1 Data Collection & Analysis . . . 60
3.4.3.2 Fitting Results . . . 61
3.5 Discussion . . . 62
3.6 Conclusion . . . 63
CHAPTER 4 ROBOTIC ANTENNA RANGE SCAN GENERATION WITH HIERARCHICAL OBJECTIVE MINIMIZATION AND MEASUREMENT ORDER OPTIMIZATION . . . 64
4.1 Abstract . . . 64
4.2 Introduction . . . 64
4.3 Methods . . . 68
4.3.1 Dual Manipulator Relative Jacobian . . . 68
4.3.2 Hierarchical Inverse Kinematics Implementation . . . 69
4.3.3 Hierarchical Objectives . . . 70
4.3.3.1 Pose Error Objective and Joint Limit Constraint . . . 70
4.3.3.2 Joint Excursion Objective . . . 71
4.3.3.3 Metrology Measurement Uncertainty Objective . . . 71
4.3.4 Asymmetrical Travelling Salesman Problem Ordering . . . 72
4.3.4.1 Weight Generation . . . 72
4.3.5 Command Streaming . . . 73
4.4 Studies . . . 73
4.4.1 System Configuration . . . 73
4.4.2 Simulated Study . . . 74
4.5 Discussion . . . 75
4.6 Conclusion . . . 76
CHAPTER 5 CONCLUSIONS & FUTURE DIRECTIONS . . . 77
5.0.1 Contributions . . . 77
5.0.2 Future Work . . . 78

REFERENCES 80

APPENDIX A RECURSIVE ANALYSIS OF COMPLEX MECHANISMS 90

APPENDIX B ROBOTIC ANTENNA RANGE CONTROL 91

LIST OF FIGURES

Figure 2.1 CAD representation of a complex hybrid manipulator similar to that simulated for calibration approach validation. Hybrid manipulators can be used to extend the fine end-effector positioning of parallel manipulators over a large workspace. 10

Figure 2.2 Robotic manipulators representative of those described in this work. Displayed as (A) parallel manipulator, (B) serial manipulator, and (C) hybrid manipulator. 11

Figure 2.3 Notation representing the hybrid manipulator. Standard serial links are represented in green, with parallel members $\mathbf{M}_1$ and $\mathbf{M}_2$ formed from serial links in blue. Adjustable pose offsets are represented by dashed lines, while serial links are solid. Strictly serial links $\mathbf{L}_1$ and $\mathbf{L}_2$ share parameters across each serial chain. The length of links $M_{1,2}$ and $M_{2,2}$ and the joint angles of links L_1 and L_2 are actuated (active joints, $\boldsymbol{\theta}$). All rotation joints within parallel members $\mathbf{M}_1$ and $\mathbf{M}_2$ are unactuated (passive joints, $\boldsymbol{\psi}$). 18

Figure 2.4 Evolution of the trace of expected pose-error covariance with respect to data set size. Values are displayed as a percentage of the expected pose-error covariance found at the minimum necessary calibration data set of twelve 6 DoF poses for the hybrid manipulator. Median values are listed above each distribution. 100 trials were conducted for each N value to generate the actual distributions (blue). Distributions predicted by (2.44) are pictured in red, and show convergence with actual results as $N \to \infty$. 32

Figure 2.5 Validation data set error distributions for simulated hybrid manipulator calibration. Measurement uncertainty is added to each data point as described in Section 2.4.2. Initial error distributions (red, A) are significantly higher than calibrated error distributions (blue, B). Error distributions on the same validation data set without measurement uncertainty (green, C) indicate that the calibration procedure reduces error below the measurable uncertainty threshold. Median values are listed above each distribution, and a log axis scale is used to present the different magnitudes of data presented. 33

Figure 2.6 Experimental 7 DoF hybrid robotic manipulator constructed from a 6-RRRPRR parallel manipulator with offset R-R joints mounted on a precision rotary stage. Spherical laser tracker target positions are marked with red. Laser tracker is not in view and is positioned approximately 2 meters from the manipulator without visual obstructions. . . . 35

Figure 2.7 Mean uncertainty distributions for the collected data set of 800 point measurements (3 DoF) and the resultant 200 reconstructed frames (6 DoF) used in the experimental calibration of Section 2.4.6. Mean uncertainties are defined as the square root of the trace of a covariance matrix divided by its degrees of freedom (2.40). In the case of the 6 DoF frame reconstruction, the position terms and rotation terms are considered separately to illustrate the relative magnitude of the components. Median values are listed above each distribution. 37

Figure 2.8 Experimental error distributions for validation data set of 60 poses. Significantly larger pose-error distributions exist for the parallel manipulator in both position and rotation using manufacturer calibration (red) when compared to equivalent calibrated quantities (blue). Median values are listed above each distribution. 40

Figure 3.1 7 Degree of Freedom (DoF) hybrid robot manipulator used as the basis for simulated and experimental studies. We fit kinematic parameters and a laser tracker uncertainty model simultaneously using an EM algorithm. World frame is aligned axially with rotary stage motion and referenced to 5 statically mounted SMRs indicated with blue dashed line. End effector frame is referenced to 5 SMRs indicated with red solid line. A laser tracker (out of frame) is positioned to provide visibility of all targets. 49

Figure 3.2 An example of the rotation of a direct-drive metrology instrument (${}^{B}\boldsymbol{R}_{L}$) to achieve measurement of a point denoted by the red sphere. A similar direct drive laser tracker system is used to collect point measurements within this work. 52

Figure 3.3 Representation of the measurement frames in which point measurement error is evaluated to fit uncertainty model. Solid dots indicate the point positions calculated with the fitted kinematic model, while the crosses indicate the associate real measurement collected. Each residual is individually evaluated in the projected measurement frame projected from the metrology system. 54

Figure 3.4 RMS pose-error distributions for experimental kinematic calibration study calculated from best-fit 6 DoF frames generated from measured point bundles. The calibration data set of 141 points (blue, A) and validation data set of 61 points (green, B) have similar means and distributions. Median values are listed above each distribution, and a log axis scale is used to present the different magnitudes of data presented. 61

Figure 3.5 Grouped point measurement residuals from experimental study reported in measurement frames and normalized by dividing by point-wise measurement distance to allow direct comparison to fitted α variance. 62

Figure 4.1 Visual representation of current scanning configurations on the LAPS system. Existing scan implementations constrain motion to reproduce positioner motion of specialized antenna manipulators along the indicated axes, using a small subset of available joints during operation. Extreme joint angles, visible on the spherical example, ultimately limit possible scan sizes in these configurations. Our inverse kinematics solution approach removes this constraint, resulting in larger possible scan sizes with lower joint excursion. 66

Figure 4.2 Holistic Jacobian generation for two individual manipulators is accomplished by introducing static offsets and relative rotations without the use of an inverted link notation. Relative transforms can be efficiently calculated using this technique, with secondary objectives introduced by using the larger null space present with holistic control. 69

Figure 4.3 Visual representation of scanning configurations calculated with the hierarchical inverse kinematics framework. When compared to existing scan implementations shown in Figure 4.1, lower total joint motion is used to reach each pose. The absence of extreme joint angles permits faster motion with larger scan sizes. 74

Figure A.1 Vidual representation of the analysis of complex manipulator cases. By identifying and evaluating low-level parallel components (I), serial-equivalent representations of these components can be used to facilitate analysis of nested parallel structures (II). Additional manipulator links added to the distal or proximal ends of the manipulator are evaluated in standard serial fashion (III). 90

Figure B.1 Screen capture of the front panel of the LabView unified robotics antenna range control program. 91

Figure B.2 Robotic antenna range control architecture. The LabView interface permits user control of critical components of the antenna range in a unified manner by integrating equipment SDKs. 92

LIST OF TABLES

Table 2.1 Mathematical Notation Summary. 13

Table 2.2 Simulated Manufacturing Error Intervals. 30

Table 2.3 Simulated Data Standard Deviations. 31

Table 2.4 Actuated Joint Encoder and Variance Information. 34

Table 2.5 Alternate Calibration Method Comparison. 41

Table 2.6 Link Type Abbreviations. 45

Table 2.7 Symbolic Jacobian Definitions. 45

Table 2.8 Simulated Hybrid Manipulator Parameters. 46

Table 2.9 Experimental hybrid manipulator parameters. 47

Table 3.1 Notation summary. Matrix size is displayed in brackets before description and subscripts provide contextual definitions. 50

Table 3.2 Robot Encoder Specification 57

Table 3.3 Simulated Study Uncertainty Parameters 59

Table 3.4 Simulated Manufacturing Error Intervals. 59

Table 3.5 Measurement Acquisition Failures 60

Table 3.6 Experimental Study Fitted Uncertainty Parameters 61

Table 4.1 Notation summary. Matrix size is displayed in brackets before description and subscripts provide contextual definitions. 68

Table 4.2 Antenna Scan Configurations 74

Table 4.3 Simulated Antenna Scan Results 75

LIST OF ABBREVIATIONS

Antenna Under Test	AUT
Consumer-off-the-Shelf	COTS
Degrees	deg
Degrees-of-Freedom	DoF
Expectation-Maximization	EM
Nonlinear Least Square	NLS
Parallel Kinematic Machine	PKM
Quadratic Programming	QP
Sequential Quadratic Programming	SQP
Software Development Kit	SDK
Vector Network Analyzer	VNA
Weighted Least-Squares	WLS

ACKNOWLEDGMENTS

I would like to acknowledge the funding provided from the NIST PREP program for making this research possible.

I am deeply grateful for my graduate research advisor, Dr. Andrew Petruska, for his guidance, insight, and encouragement that were crucial to shaping my studies. His expertise and passion for research is something I will always strive to replicate. I would also like to extend my appreciation my NIST PREP sponsor, Dr. Josh Gordon, for research assistance and valuable feedback on my work. Through mentorship for antennas and standards topics, he has greatly impacted the directions and applications of my research.

I am also thankful to the members of my thesis committee for their time, expertise, and critical insights. Their constructive feedback has greatly improved the quality of my research.

I would like to recognize the members of the Robo-Bio graduate group - although our disciplines varied, I deeply appreciated the insights and supportive feedback for my research. I will always fondly remember our time together.

For all my friends and family, I could not have done it without you! Your love and support has been invaluable to me during my time as a "forever student." Thank you for all your chats, reviews, and rubber ducking.

For the little victories.

CHAPTER 1
INTRODUCTION

Antenna metrology is the process of measuring and characterizing the signal emitted by an antenna at frequencies of interest. Measurements of signal strength and polarization are collected at a variety of relative positions and combined to understand the performance of an antenna. Although increasingly sophisticated simulation software can facilitate antenna design and evaluation, experimental measurement of antennas as manufactured is necessary to validate designs and ensure that they meet application specifications and comply with relevant standards. Antenna metrology is critical in ensuring that antenna systems meet the required level of performance and reliability for modern communications applications in our increasingly-connected world.

Historically, antenna metrology has relied on evaluating antennas in the far-field where the radiation pattern is fully developed, but at low frequencies require larger measurement ranges difficult or impossible to environmentally control. Methods to convert antenna measurements in the near-field to the desired far-field patterns were pioneered in the 1960's, permitting the calculation of absolute gain and polarization on compact, interior antenna ranges with tightly controlled environments [1]. Each set of measurements must be collected across a simple geometry to permit mathematical expansion. Referred to as 'canonical scans', these include planar, cylindrical, and spherical patterns centered around an antenna under test (AUT) [2]. Positioning accuracy requirements for each scan geometry vary, but are typically represented as a fraction of the smallest wavelength measured (e.g. $\frac{\lambda}{100}$). Many existing installations use specialized fixtures and mechanisms to allow for repeated measurements of the tested antenna over a specific scan surface. The antenna positioning mechanisms traditionally used in these applications are specialized and low-DoF, only capable of moving over a specific scan geometry with a single non-trivial configuration for each desired pose. Therefore, traditional antenna ranges lack flexibility, requiring multiple large and specialized installations to support desired scan configurations.

A recent evolution in antenna metrology is the incorporation of robotic positioning systems, which present major advantages in the areas of scan geometry and flexibility by allowing for a large number of measurement frequencies and antenna designs to be supported on a single installation [3]. By utilizing multiple industrial manipulators in an antenna range, multiple canonical near-field scan types can be performed with comparable performance to traditional antenna range systems [4–6]. The industrial robot components used in contemporary systems feature wide commercial availability and attractive work volumes, but are characterized by highly precise motion with accuracy dependent on installation and

manufacturing variables. For the purposes of antenna metrology positioning accuracy, represented by the 6 degree-of-freedom position and rotation pose of the AUT-Probe transform, is critical. A variety of approaches have been developed to increase pose accuracy to meet the needs of antenna metrology scans, such as external feedback correction [7] or adjusting the near-field expansion to account for non-ideal antenna measurement positions [8]. Kinematic calibration, a process in which a mathematical model describing the motion of a robot is fitted to reduce pose-error, is prevalent throughout the robotics community and offers an 'offline' alternative to active, external feedback approaches, but has not been extensively applied to commercial or research robotic antenna ranges. Quantifying the benefits to positioning performance of common manipulator types found in robotic antenna ranges can address performance concerns and facilitate wider adoption within the antenna metrology community.

Traditional antenna metrology positioning systems, such as stacked Cartesian stages for planar scans and roll-over-azimuth mechanisms for spherical scans, often provide straightforward pose uncertainty evaluations due to the simple construction and motion. In contrast, robotic manipulators contain numerous documented sources of uncertainty, such as joint hysteresis, bending effects, thermal expansion, and discrete encoder counts coupled in a highly non-linear manner. However, robotic antenna ranges present an atypical case for industrial manipulators, featuring significantly lower duty cycles in a controlled environment. Providing a deeper understanding of robot pose uncertainty in antenna ranges is critical, as the final antenna measurement uncertainty is directly impacted by the position uncertainty of each antenna measurement. Investigation and characterization of the principle components of robotic pose uncertainty for this use case can provide insights into measurement frequency limitations and guide future facility design choices.

While robotic antenna ranges have demonstrated comparable scanning performance to traditional antenna ranges, they are constrained by this legacy. Popular configuration of robotic manipulators for antenna metrology purposes feature multiple industrial robots operating together in a high-DoF configuration. Contemporary robotic antenna range implementations are over-actuated for the 6 DoF positioning tasks found in antenna scanning. Current scanning configurations do not fully utilize the combined motion capabilities of their constituent manipulators. Rather, motion for canonical scans is constrained to replicate that of the traditional specialized manipulators, leaving many actuated joints in static or quasi-static positions through the duration of the scan. The full capabilities of robotic systems as applied to the specific positioning requirements of antenna metrology have not yet been realized, with state-of-the-art systems relying on basic industrial robotic capabilities. Implementing methods to reach desired AUT-Probe transforms that integrate combined robotic motion can provide expanded antenna metrology capabilities to robotic antenna ranges, particularly with respect to maximum scan geometry.

Furthermore, minimizing secondary objectives that impact antenna metrology quality, e.g. joint bending or pose measurement uncertainty, has the potential to improve final antenna scan quality by reducing measurement time and cable bending.

The purpose of this work is to develop, implement, and evaluate robotics-oriented software and algorithms to advance the state-of-the-art of robotic antenna metrology by improving positioning performance and versatility. Quantitative assessment in these areas on modern robotic antenna range hardware and configurations will expand the capabilities of existing antenna ranges and guide effective construction and operation of next-generation antenna ranges. The following chapters provide studies of robotic antenna range components, including kinematic modelling and calibration (Chapter 2), validation of position measurement uncertainty of position feedback or position measurements to characterize pose uncertainty (Chapter 3), demonstration of inverse kinematics solutions for canonical antenna metrology scans (Chapter 4), and conclusions and future research directions (Chapter 5). A summary of the publications and presentations related to this research has been prepared (Appendix A).

1.1 Robotic Antenna Ranges: State-of-the-Art Implementations

The use of industrial robotic components in the field of antenna metrology is a recent development, and a growing number of examples in research and commercial settings are documented in contemporary literature. Despite similarities in actuator components and control, we differentiate between traditional positioning systems composed of stacked rotary or linear stages and robotic antenna ranges incorporating industrial manipulators on the basis of controllable DoF and commercial availability. Traditional antenna positioning systems feature low (2-3) controlled DoF positioned in orthogonal directions of motion, and are constructed expressly for antenna metrology purposes by low-volume, specialized manufacturers to perform individual scan geometries [9]. In contrast, robotic antenna ranges use consumer-off-the-shelf (COTS) industrial manipulator components intended for general use and high (7-13) combined DoF. The use of these manipulators enhances antenna metrology by reducing facility costs and permitting all canonical near-field scan types to be performed in a single installation. The field of antenna metrology has been fundamentally changed by the introduction of robotic antenna ranges.

Robotic antenna ranges are typically composed of multiple commercially-available robotic manipulators which work together to perform antenna scan types, with several distinct configurations existing in contemporary installations. For high frequency measurements (40 GHz-500 GHz) requiring high accuracy but smaller scan geometries, a single robot arm is coupled with secondary positioning components such as linear and rotary stages or parallel manipulators to permit AUT motion [4–6, 10, 11]. Lower frequency measurements (8 GHz - 40 GHz) require larger scan geometries with reduced accuracy requirements and

utilize a configuration with two robot arms, one of which is mounted on a linear stage [12, 13]. Very large scanning geometries for *in situ* evaluation of mounted antennas are made possible by attaching a robot arm to a vertical linear stage and manually positioning the manipulators in a workspace [14].

Robotic antenna ranges have been tested with comparable performance to traditional antenna ranges for extrapolation, planar, and spherical test cases. External pose feedback, typically from a laser tracker system, is used to compensate for position errors [4, 14] and facilitate antenna alignment [7]. Current antenna ranges apply position offsets using the controller kinematic model equal to measured error, often requiring several compensation steps before convergence is reached due to mismatch in motion frames and robotic kinematics. Additionally, view angle limitations for the position feedback system require the use of secondary targets to permit feedback over an entire scan. In some cases, the final robot joint values required to reach a desired position are stored as a "compensation grid" for a particular scan, serving as a limited lookup table to bypass native controller motion [5]. Software compensation for non-ideal poses for the near-field expansion has also been explored, but similarly requires active position measurements during the scanning process [8, 15]. Positioning accuracy remains a major factor in limiting the performance of robotic antenna ranges due to the inflexible and expensive methods currently used to achieve desired performance.

Antenna scans produced by current robotic antenna ranges are designed to reproduce the motion of traditional antenna positioning systems, constraining many of the robotic joints to static positions during a scan [13]. Although presenting easy integration with native industrial robot controller capabilities [16], this limits the maximum scan geometry sizes possible on standard robotic range configurations. This is particularly visible in spherical measurement cases, where contemporary robotic antenna ranges exhibit a maximum radius of approximately $1\,m$ [4, 17]. Non-canonical scanning techniques have been proposed to address these limitations [18], but retain the limitations of prior implementations. Very recent work has presented novel scan types based on sparse sampling techniques that do not mimic the motion of traditional manipulators [19], instead using spline-based motion over a spherical scan geometry. The limitations presented by directly implementing legacy scanning profiles onto robotic antenna ranges reduce their flexibility and require changes to expand their use.

1.2 Kinematic Modelling & Calibration

Various approaches to describing the kinematics of serial mechanisms with different properties related to minimality, continuity, and ease of implementation are found throughout literature. Representations based on the Denavit-Hartenberg (DH) parameterization [20] are commonly found in industry due to the relative simplicity and established status, but are poorly posed to handle joints with near-parallel frames of

motion. Alternate representations, notably the Hayati parameterization [21], have been used to update the underlying DH model to better handle these behaviors. The later Product of Exponentials (POE) representation [22] has seen widespread adoption in academia due to the smooth and continuous nature of the links. Alternate forms [23] have been proposed to simplify implementation by using local geometric terms.

Kinematic calibration can broadly be described as adjusting a parameterized representation of a robot to minimize identified error terms. The calibration of serial robots, or manipulators formed by a series of successively connected links, is a mature field with well-established results across a variety of implementations. Although identified as a non-linear optimization problem for non-trivial industrial manipulators, first-order approximations can be used during calibration without loss of final accuracy [24]. This approach has been used to minimize pose error in closed-loop manipulator cases [25] and extended to open-loop measurement cases by creating an implicit link constraint with a pose measurement [26]. This approach replaced older techniques that relied on precision machined surfaces and fixtures to generate a tractable parameter identification problem [27]. Analytical Jacobians for this purpose are easy to compute for serial robots [28] and increase accuracy while reducing computation time compared to numerical approximation.

Much greater variation exists in the modelling of parallel manipulators throughout literature. This is illustrated in the Stewart-Gough configuration, which is commonly used in high load 6 DoF applications such as tire testing [29] and flight simulation [30]. Common representations rely on the assumption of perfect spherical and universal joints to simplify the modelling process [31–34] or use rotationally-symmetric terms to form unique geometric solutions [35, 36]. Some works with parallel mechanisms of increased complexity [37] have used the serial link notations outlined above, but application-specific notation is still common.

The large number of possible configurations and representations used with parallel manipulators has resulted in a lack of consensus on the calibration of such mechanisms. Physical motion constraints on a system [38] or the addition of redundant joint instrumentation [39] can provide avenues for calibration by reducing the problem to a serial case, but require modifications that are difficult or impossible to add to existing systems. Serial pose error minimization techniques have been extended in several cases to the calibration of parallel manipulators, but are limited by the use of the finite difference method used to generate the Jacobians [33], which requires repeated evaluation of the manipulator forward kinematics. Other work has generated analytical Jacobians limited to specified geometry [34, 40]. Although recent publications have adopted laser tracker metrology systems to provide highly accurate pose measurements to enhance established calibration processes [41, 42], the underlying kinematic models are not extensible to

more general parallel manipulators. The lack of a general representation has resulted in ongoing publication of research analyzing specific new designs [43, 44].

1.3 Pose Uncertainty

Pose error, which encodes the difference between the desired and actual AUT-Probe position, in robot manipulators is caused by a variety of factors, with common features identified in literature as encoder resolution [24], manipulator hysteresis and stiffness [45–48], and temperature effects [49–51]. In a typical uncalibrated serial manipulator, it has been proposed that geometric errors account for 90% of the total pose error of the system [52]. Analysis of Stewart Platform mechanisms has demonstrated that parallel manipulators share similar magnitudes of pose error due to geometric errors for a given scale of manipulator [53]. Non-geometric terms can be identified and calibrated to enhance accuracy, with encoder offset error noted as a large source of error [54]. The identifiability of non-geometric terms related to joint and link stiffness in general cases is questioned in later work, as the impacts of each error source vary dramatically based on manipulator construction [55]. More recently, parameterized stiffness models have been developed and validated experimentally to compensate for some non-geometric effects [56]. Un-parameterized error sources are incorporated into the parameterized set during the minimization process, producing a best fit to the available data.

Modern robotic antenna positioning systems typically rely on high accuracy measurement devices such as laser trackers [4] or multi-camera arrays [57] to reduce pose error during the antenna characterization process. It is important to understand the uncertainty associated with these measurements, as they are used to directly determine position state for many robotic antenna positioning tasks [4, 14] or incorporated into final kinematic parameter fits by calibration [58]. Laser trackers are commonly used for contact-free position measurements such as those desired for antenna metrology. These metrology instruments generate polar measurements with well-characterized uncertainty components; uncertainty terms associated with the resolution of encoder terms dominate those of the radial distance measurement and transient environmental impacts [59].

The propagation of uncertainty within a calibration process is vital to informing the final quality of the calibration, but has been minimally explored. Uncertainty incorporated into the measurements used to drive the calibration process propagates into parameter uncertainty, which then impacts final pose accuracy. Monte Carlo analysis techniques have been applied to determine the scale of these uncertainties in a typical serial manipulator [60], but favor computationally intensive methods of calculating the uncertainty propagation. The linearized kinematic model of a robot manipulator can be used with measurement uncertainty models to provide insight into the final uncertainty characteristics of the device

without computationally expensive simulations. It is expected that the residuals of a calibration process incorporating measurements with known uncertainty shapes can be used to parameterize measurement uncertainty over the calibrated robot workspace. Due to the large component of robot pose uncertainty related geometric terms, the post-calibration performance of a robotic manipulator is of interest.

1.4 Pose Selection & Path Planning

The inverse kinematics problem, which finds the robot joint positions necessary to reach a desired AUT-Probe transform, must be solved for each of the robots to reach poses during antenna scanning. Basic inverse kinematics tasks are well-documented in literature [28], and are integrated into industrial manipulator controllers. Analytical inverse kinematics solutions exist for some manipulator types and are found by directly analyzing the geometry of a manipulator to create a series of equations that can be solved to find appropriate joint configurations. Numerical inverse kinematics solutions are found by performing a minimization problem to find valid joint configurations. Historically, this process has been implemented through the use of Jacobian pseudo-inverse methods, which use first order Gauss-Newton fitting with locally linearized kinematics to find a solution [28, 61]. This process can exhibit poor performance due to the presence of joint limits and fail to converge. The TRAC-IK algorithm increases the likelihood of success by incorporating random restarts from different valid joint configurations. To better handle joint constraints, this method also introduces parallel runs of an SQP-based inverse kinematics, which offers significantly better convergence rates at the cost of increased computation time, and Jacobian pseudo-inverse inverse kinematics [62]. Improvements to final execution time have been demonstrated through the use of analytical gradients [63].

When considered in a combined manner, common robotic antenna range manipulator configurations are over-actuated for reaching the 6 DoF poses required for general canonical scans. The redundant DoF present can be used to optimize for other tasks while solving the inverse kinematics problem[64]. A large body of literature outlines hierarchical optimization, in which tasks of lower priority are optimized without interfering with tasks of higher priority by projecting them into the null space of all preceding tasks. Hierarchies for equality tasks can be implemented using Jacobian psuedoinverse methods [65–67]. Inequality tasks require the use of active set minimization methods, such as SQP [68–70]. Hierarchical optimization methods have been effectively used to drive complex motion in high-DoF robots such as humanoid robots [70–72].

Robotic antenna ranges often feature multiple manipulators moving in a coordinated fashion in a shared workspace, leading to the possibility of collision. Current use cases represent a near-ideal case for collision avoidance, with offsets between robot end effectors enforced during canonical scanning and

uncluttered anechoic chamber environments. In cases with more complex positioning, a significant body of work exists that addresses collision-free path planning. Many classic approaches become intractable as the dimensionality of the configuration space increases. Modern high-DoF planning techniques are dominated by probabilistically complete path planning approaches, particularly Randomly-Exploring Rapid Tree (RRT) methods [73]. Numerous extensions of the RRT path planning exist, many of which are tailored to specific robot configurations [74, 75].

1.5 Synopsis & Purpose

In summary, the use of robotic positioning systems in antenna metrology ranges promises to increase flexibility in terms of supported scan geometries and frequencies, but currently relies on nominal manufacturer kinematic models, produces limited scanning configurations based on specialized manipulators, and cannot utilize full collaborative motion. Kinematic calibration techniques can dramatically improve positioning accuracy, reducing the reliance on inaccurate kinematic models and expensive external feedback systems. Uncertainty propagation techniques can be used with the linearizations developed for calibration purposes to permit effective understanding of final pose uncertainty. Sophisticated inverse kinematics controllers can utilize the large solution space for high-DoF mechanisms commonly found in robotic antenna metrology to minimize secondary objectives and facilitate collaborative motion.

The goal of this work was to advance the state-of-the-art of robotic antenna metrology by combining and applying contemporary robotic techniques for enhanced positioning, uncertainty characterization, and scan geometry generation. A gap in knowledge exists in the antenna metrology community regarding these topics, resulting in increased costs, reduced measurement frequency ranges, and lower scanning geometry flexibility. This work has the potential to facilitate a paradigm shift in the antenna positioning and metrology. Three areas of research were identified and completed in support of this goal:

1. Establish the feasibility of implementing kinematic calibration for increased positioning accuracy over all manipulator types found in contemporary robotic antenna ranges.

2. Model and validate pose measurement uncertainty for laser tracker metrology instruments commonly used in antenna ranges and extend the results to post-calibration pose uncertainty.

3. Quantify improvements to canonical antenna scan patterns generated with an efficient inverse kinematics pipeline in a collaborative manner.

CHAPTER 2

UNIFIED PARAMETERIZATION AND CALIBRATION OF SERIAL, PARALLEL, AND HYBRID MANIPULATORS

Reproduced with permissions from Robotics, 2021 by MDPI. Copyright retained by authors, Creative Commons CC by 4.0 license.

Benjamin L. Moser [1], Joshua A. Gordon [2] and Andrew J. Petruska [3]

2.1 Abstract

In this work, we present methods allowing parallel, hybrid, and serial manipulators to be analyzed, calibrated, and controlled with the same analytical tools. We introduce a general approach to describe any robotic manipulator using established serial-link representations. We use this framework to generate analytical kinematic and calibration Jacobians for general manipulator constructions using null space constraints and extend the methods to hybrid manipulator types with complex geometry. We leverage the analytical Jacobians to develop detailed expressions for post-calibration pose uncertainties that are applied to describe the relationship between data set size and post-calibration uncertainty. We demonstrate the calibration of a hybrid manipulator assembled from high precision calibrated industrial components resulting in 91.1 μm RMS position error and 71.2 μrad RMS rotation error, representing a 46.7% reduction compared to the baseline calibration of assembly offsets.

2.2 Introduction

Kinematic calibration is the process in which a parameterized mathematical model used in planning and control operations is adjusted to minimize pose-error. Parallel manipulators, or Parallel Kinematic Machines (PKM), of varying degrees of freedom (DoF) are well-suited for high load applications requiring precision motion and have been utilized in applications such as pick-and-place [43], drone manipulators [76], and space telescope mirror adjustment [77]. Parallel manipulators are advantageous with respect to physical properties of manipulator stiffness and deflection, but have a significantly reduced workspace volume relative to serial manipulators. Hybrid manipulators incorporating elements from both parallel and

[1]PhD Candidate in Mechanical Engineering at Colorado School of Mines in Golden, CO. Primary author responsible for study conceptualization, system hardware/software design, experimental design, overseeing and conducting data collections, analyses, results interpretation, and manuscript preparation.
[2]Group Leader for the Electromagnetic Fields Group at the National Institute of Standards and Technology in Boulder, CO. Responsible for project administration, system hardware acquisition, and manuscript revisions
[3]Associate Professor and Director of M^{3}Robotics Laboratory in Mechanical Engineering at Colorado School of Mines in Golden, CO. Advisor to primary author. Responsible for project administration, study conceptualization, results interpretation, and manuscript revision.

serial manipulators combine these positive attributes and have been proposed for novel mechanism design [78], near-field antenna measurements [4] and medical robots [79]. Although the majority of the parallel mechanisms in the literature incorporate coincident passive joints in the form of universal or spherical joints at the top and bottom of a prismatic leg similar to the popular 6 DoF Stewart–Gough configuration [29, 30], recent work has modified the design to use offset universal joints to increase stiffness and reduce manufacturing constraints [80]. This 6-RRRPRR parallel manipulator configuration with offset R-R joints, with individual parallel members constructed of rotary (R) and prismatic (P) joints listed in order, requires more general kinematic and calibration approaches than typically used with Stewart Platform designs due to the removal of the geometric simplifications permitted by the coincident passive joints and is of particular interest within this work. We present constraint-based approaches to solve the kinematics and calibration problems for strictly parallel manipulators and hybrid parallel-serial manipulators, such as the example pictured in Figure 2.1, with the general construction shown in Figure 2.2.

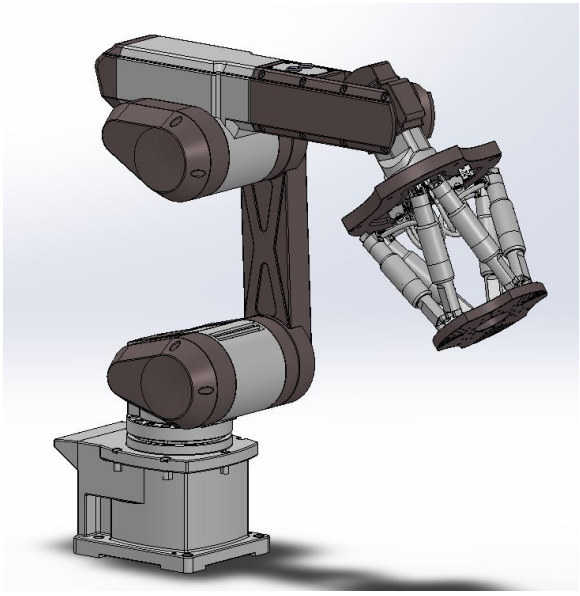

Figure 2.1 CAD representation of a complex hybrid manipulator similar to that simulated for calibration approach validation. Hybrid manipulators can be used to extend the fine end-effector positioning of parallel manipulators over a large workspace.

Parallel manipulators are advantageous with respect to physical properties of manipulator stiffness and deflection, but present significantly more challenges in analysis than serial manipulators due to the large number of kinematic parameters required to describe the manipulator and the large forward kinematic solution space [81]. Common planning operations, such as inverse and forward kinematics, are difficult to compute due to the possibility of singularities existing in the manipulator workspace, and the characteristic constraint-driven motion introduces difficulties in calibration. The calibration and kinematic evaluation of

complex parallel manipulators typically relies on varying degrees of geometric simplifications and external measurements. Efficient forward kinematic calculation has been achieved through the use of special construction geometry, inverse-kinematic-residual minimization, algebraic solutions, and polynominal methods [31, 32, 82, 83]. Hybrid manipulator kinematics encounter similar problems to strictly parallel manipulators, with closed-form solutions detailed for specific construction geometries such as stacked 3 DoF parallel manipulators [78].

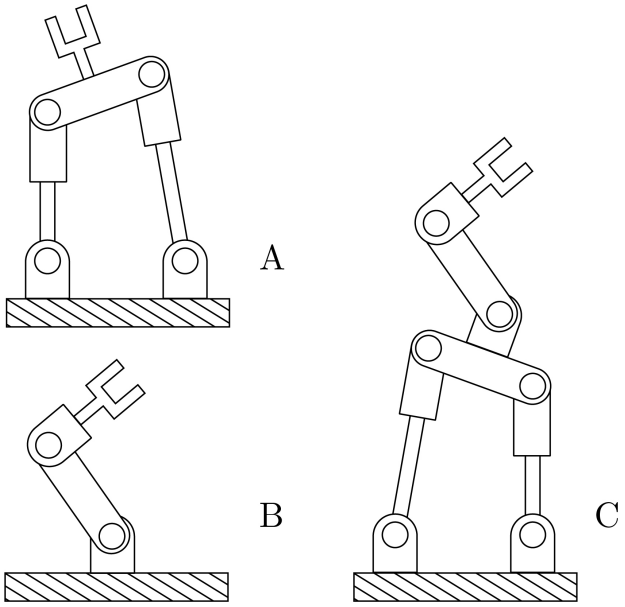

Figure 2.2 Robotic manipulators representative of those described in this work. Displayed as (**A**) parallel manipulator, (**B**) serial manipulator, and (**C**) hybrid manipulator.

Parallel manipulator calibration has been achieved using classic second-order constrained optimization techniques to simultaneously solve passive joint positions and kinematic parameters [84]. Although similar methods are implemented for kinematic workspace analysis and design [85, 86], the problem complexity grows rapidly with manipulator design. Subsequent calibration literature uses first-order fitting and addresses mechanism constraints by restricting physical motion of the manipulator [38, 87], adding redundant joint instrumentation [39, 88, 89], or using inverse-kinematics solutions [34] and forward-kinematics solutions [33] to generate approximate passive joint information. Approaches that require manipulator modifications, such as physical motion restriction or joint instrumentation, are undesirable as they are difficult or impossible to add to existing manipulators. Accordingly, we focus on methods that approximate the passive joint information that can be extended to hybrid manipulators incorporating passive joint features.

The inverse-kinematic-residual approach to calibration minimizes the difference between a measured prismatic leg length and an estimate created from the inverse-kinematics solution at a desired pose [34]. This method can be described as a position-vector-minimization implementation of loop closure methods with the approximate passive joint information [88]. This calibration approach benefits from high-accuracy measurement methods, such as laser tracker metrology systems [41, 42], and has been extended to solve the inverse-kinematics and calibrate a 6-RRRPRR parallel manipulator with offset R-R joints [77, 90]. Recent work typically utilizes Product-of-Exponentials (POE) link representation [22], with successful calibrations demonstrated on a 3 DoF parallel manipulator and a 6 DoF Stewart Platform [91].

Pose-error Jacobian minimization methods based on forward-kinematics solutions are commonly used in serial manipulator calibrations in which an end-effector measurement is used to create a virtual closed kinematic chain [25]. The pose-error minimization embeds the passive joint estimate within the Jacobian to holistically minimize the difference between a measured pose and a forward-kinematics solution generated with the current parameter set. Analytical Jacobian formulations exist for standard Stewart Platform leg geometry [40], but not for general manipulators. The difficulty associated with determining analytical Jacobians has led to the use of computationally intensive and less accurate direct perturbation methods to find an approximate Jacobian [33, 92] or the use of heuristic optimization methods to minimize pose-error such as the Nelder–Mead [93]. Recent work using pose-error minimization has focused on specialized manipulators with relatively low mechanical complexity. Mechanism-specific analytical Jacobians have been developed in 3 DoF [94] and 5 DoF [95] cases and implemented with regularization techniques and genetic algorithm fitting to allow for pose-error calibration.

Although standard Least-Squares fitting methods are common throughout literature, the noisy measurements have been identified as having large impacts on calibration quality due to low parameter identifiability [88]. Alternate approaches for handling the low parameter identifiability of parallel manipulators have been demonstrated in manipulator-specific or representation-specific cases, such as ridge regression, truncated singular value decomposition, and null space conditioning [96–98]. These techniques can positively impact the quality of the final calibration and have been compared in [91].

Post-calibration manipulator uncertainty analysis has been sparsely identified in the literature. Monte Carlo techniques have been implemented on parallel manipulator for analysis, but remain computationally expensive for comprehensive workspace analysis [99]. The uncertainty minimization calibration approach demonstrated by [89] utilizes a priori covariance estimates based on construction specifications for kinematic parameters and encoders as inputs. As the covariance estimates were inflated arbitrarily to maintain congruence with expected manufacturing tolerances, final pose uncertainty cannot reliably be obtained from this approach.

The manipulator-specific approach to model derivation and analysis found in state-of-the-art literature for parallel manipulators starkly contrasts with the mature body of work for general serial manipulators, and the common inverse-kinematic-residual minimization approaches are problematic to extend to holistic hybrid manipulator calibration. The myriad of possibilities for the construction of novel parallel and hybrid manipulators exacerbates the lack of consensus in the robotics field concerning their kinematics and calibration, driving the need for a simple and generalized representation capable of implementation across the variety of manipulators found in the industry and research sectors.

This paper's contribution can be broken into three distinct areas. First, we present a general approach to describing any robotic manipulator with the same mathematical framework as serial-chain manipulators. Second, we provide general analytical methods to construct both kinematic and calibration Jacobians for any robot manipulator. Third, we leverage these methods to quantify the post-calibration pose uncertainty for any robot manipulator based on measurement uncertainty, which has not been previously done. This work extends the state-of-the-art by allowing parallel, hybrid, and serial manipulators to be analyzed, calibrated, and controlled with the same analytical tools.

Table 2.1 Mathematical Notation Summary.

Symbol	**Description**
$\mathbf{R}$	$[3 \times 3]$ Rotation matrix
$\mathbf{d}$	$[3 \times 1]$ Cartesian displacement vector
$\mathbf{T}$	$[4 \times 4]$ Homogeneous transformation matrix
$\boldsymbol{\tau}$	Vector-based transform parameterization
$\mathbf{e}$	Pose-error vector
$\mathbf{J}$	Calibration Jacobian
$\mathcal{C}$	Constraint Jacobian
ϕ	Vector of all kinematic parameters
θ	Vector of all actuator inputs
ψ	Vector of all passive joints
v	Subscript denoting velocity Jacobian
N	Number of measurement poses within a data set
P	Number of ϕ terms for a link
L	Number of links representing a manipulator

This paper is structured as follows. In Section 2.3, we review the nonlinear least squares based kinematic calibration framework as implemented on serial robots and detail how a parallel manipulator can be represented using serial parameterization and simplified numerical kinematics solutions. A method to enforce mechanical constraints on a Jacobian level via null-space is introduced as a component of the inverse kinematics method. The analytical velocity Jacobian for a parallel manipulator is presented. We then extend the constraint propagation to generate a unified calibration Jacobian for hybrid manipulators

allowing for simultaneous calibration. We additionally present a detailed uncertainty analysis based on this calibration method and develop guidelines for uncertainty-aware calibrations. In Section 2.4, we demonstrate this method on a simulated and real world hybrid manipulator, respectively. In Section 2.5, we discuss calibration performance and possible extensions of our work. For convenience, the notion used throughout this paper is summarized in Table 2.1. Matrix size is displayed in brackets before description and subscripts provide contextual definitions.

2.3 Materials and Methods

2.3.1 Calibration Methodology Overview

We develop general pose-error Jacobians for kinematics and calibration by applying existing serial manipulator link definitions and Jacobian formulations to individual kinematic chains between the distal and proximal frames of a parallel manipulator. By segregating the Jacobian information related to active joints, passive joints, and kinematic parameters, we construct constraint matrices between all kinematic chains within the manipulator. We condition the pose-error Jacobians with the null space of these constraint matrices to only permit updates that do not introduce error between the distal frames of each kinematic chain. This produces a single Jacobian for the entire parallel manipulator, permitting it to be used for fitted kinematic and calibration solutions.

The calibration approach in this section is described in a general manner. Analytical definitions of pose-error Jacobians exist for many serial robotic link representations, and are straightforward to calculate if not available. The advantages of individual parameterizations vary and are dependent on the final application.

2.3.2 Pose-Error Minimization Framework

Calibration procedures aim to reduce discrepancies in expected and measured poses for a robot manipulator. We extend an established calibration framework that minimizes a 6 DoF pose-error calculated at a number of measured poses by adjusting the nominal kinematic model parameters of a manipulator [25]. We detail the basic principles and operation of this framework to provide contextual basis for our extensions starting in Section 2.3.3.

2.3.2.1 Objective and Error Formulation

Calibration can be expressed as the general optimization problem

$$\arg\min_{\phi} \|\mathbf{E}\|^2, \tag{2.1}$$

where $\mathbf{E}$ is a general representation of a pose-error vector at all points within a measurement data set. A robust error model is required to evaluate the performance of the kinematic model and permit effective calibration. The position error $\Delta\mathbf{p}$ is calculated as

$$\Delta\mathbf{p} = \mathbf{d}_{\mathrm{m}} - \mathbf{d}_{\mathrm{c}}, \tag{2.2}$$

where $\mathbf{d}$ represents a vector containing the Cartesian position of the robot manipulator end-effector with subscript denoting as the value being either obtained through a measurement (m) or calculation (c) via the mathematical model.

Small rotational errors can be represented as a differential orthogonal rotation [25], however, this approach poorly represents large rotational errors. To provide more robust calibration behavior, we implement an angle-axis based alternative that linearizes the rotation error for all error magnitudes as

$$e^{[\Delta\mathbf{\Omega}]_\times} = \mathbf{R}_{\mathrm{e}} = \mathbf{R}_{\mathrm{m}}\mathbf{R}_{\mathrm{c}}^{\top}, \tag{2.3}$$

where $\mathbf{R}$ represents the rotation matrix representation of the robot manipulator end-effector using the subscript notation defined above. The angle-axis equivalent $\Delta\mathbf{\Omega}$ is calculated from the rotation error ($\mathbf{R}_e$) using standard conversion methods [100].

These error components are packed into a pose-error vector as

$$\mathbf{e} = \begin{bmatrix} \Delta\mathbf{p} \\ \Delta\mathbf{\Omega} \end{bmatrix}, \tag{2.4}$$

where $\Delta\mathbf{p}$ is the position error and $\Delta\mathbf{\Omega}$ is the rotation error. The calculation of this error vector between transforms is referenced in this work as $\mathbf{e}\left(\mathbf{T}_1, \mathbf{T}_2\right)$, although the inputs are typically contextually inferred.

2.3.2.2 Jacobian Packing

Pose-error evolution with respect to the manipulator kinematic parameters $\boldsymbol{\phi}$ is described in a linear manner by analytical Jacobians. When evaluated at a pose with known actuator positions $\boldsymbol{\theta}$, each calibrated parameter produces a [6×1] vector of the relationship between the 6 DoF error term and perturbations to the respective kinematic parameter. As a single error term exists for each measured pose, the vectors corresponding to all kinematic parameters are horizontally concatenated in a common Jacobian packing method [25]. For convenience, parameters associated with an individual serial link are grouped, resulting in the block Jacobian for a single pose of

$$\mathbf{J}_\phi = \left[\underbrace{\left[\frac{\partial\mathbf{e}}{\partial\phi_{1,1}} \cdots \frac{\partial\mathbf{e}}{\partial\phi_{1,P}} \right]}_{\text{Link 1}} \cdots \underbrace{\left[\frac{\partial\mathbf{e}}{\partial\phi_{L,1}} \cdots \frac{\partial\mathbf{e}}{\partial\phi_{L,P}} \right]}_{\text{Link L}} \right], \tag{2.5}$$

where the Jacobian blocks corresponding to links with P parameters are displayed. Blocks corresponding to any number of links can be concatenated to permit calibration of any possible serial manipulator construction. Symbolic definitions for pose-error Jacobian components for the link parameterizations used within this work are provided in Appendix 2.8.

Multiple pose measurements are required for convergence of the pose-error minimization solution during calibration of nontrivial robotic manipulators. To accommodate any number of measurements, pose-error terms (2.4) and the concatenated kinematic parameter Jacobian (2.5) are vertically concatenated for N points as

$$\mathbf{J}_\Phi = \begin{bmatrix} \mathbf{J}_{\boldsymbol{\phi},1} \\ \mathbf{J}_{\boldsymbol{\phi},2} \\ \vdots \\ \mathbf{J}_{\boldsymbol{\phi},N} \end{bmatrix}, \quad \mathbf{E} = \begin{bmatrix} \mathbf{e}_1 \\ \mathbf{e}_2 \\ \vdots \\ \mathbf{e}_N \end{bmatrix}. \tag{2.6}$$

Here, a Jacobian representing all measured poses is expressed with an uppercase Φ, while a Jacobian representing any single measured pose is expressed with a lowercase ϕ.

2.3.2.3 Parameter Update

Manipulator kinematic parameters ϕ can be found to minimize the pose-error using the Gauss–Newton approach to nonlinear least squares with $\mathbf{J}_\Phi$ and $\mathbf{E}$. Successive $\Delta\phi$ steps on a set of all measured poses are calculated as

$$\Delta\phi = \mathbf{J}_\Phi^\dagger \mathbf{E}, \tag{2.7}$$

where $\dagger$ indicates the pseudoinverse of a matrix. Within this work, the pseudoinverse is calculated using Singular Value Decomposition (SVD) of the Jacobian matrix as

$$\mathbf{A}^\dagger = \mathbf{V}\boldsymbol{\Sigma}^{-1}\mathbf{U}^\top, \tag{2.8}$$

where $\mathbf{U}, \boldsymbol{\Sigma}, \mathbf{V}$ are standard SVD components [101]. Small singular values within $\boldsymbol{\Sigma}$ corresponding to poorly identifiable kinematic parameters can result in the calculation of extremely large terms within the pseudoinverse generation process. These parameters are ignored by replacing the terms within $\boldsymbol{\Sigma}^{-1}$ that correspond with singular values with condition numbers above a specified threshold with 0 [102]. This produces a similar step to Levenberg–Marquardt fitting with a fixed damping parameter.

The step is added to the existing ϕ and the process is repeated until convergence conditions are met. More robust stepping algorithms such as the Levenberg–Marquardt method [103] or Sequential Quadratic Programming [104] can also be used to generate steps in cases where high parameter sensitivity results in nonconvergent behavior for standard Gauss–Newton steps, but implementation details for these algorithms is outside of the scope of this work and may require additional gradients to be developed. The constrained

Jacobians produced in this work are applied for a variety of analytical purposes outside of fitting techniques, and are a primary focus of this work.

2.3.3 Parallel Manipulator Parameterization and Kinematics

To calibrate parallel manipulators simultaneously with serial links within the framework detailed above, an analogous Jacobian is required that captures the sensitivities of the kinematic parameters of the manipulator with respect to the final pose. A parallel manipulator is represented as a special serial link which returns a single transform provided a set of active joint inputs, with kinematic behavior mathematically represented by standard serial links.

Actively controlled joint parameters corresponding to the linear or rotary actuators of a robotic manipulator are denoted by $\boldsymbol{\theta}$, while passively driven joint parameters such as unpowered bearings or slides driven by the constraints of the manipulator are denoted by $\boldsymbol{\psi}$. Static offsets that describe the manipulator (for example mechanical linkages and metrology systems used during calibration) are incorporated in this work with general symbol τ, which represents a parameterized transform in vector format that can be calibrated as a typical link within the presented framework.

2.3.3.1 Serial Chain Parameterization

Parallel manipulators are constructed from several serial chains connected in a manner that constrains their motion. These serial chains, termed parallel members within this work, are often underactuated due to the presence of one or more unpowered joints. A parallel member is represented using a standard serial link models positioned by pose offsets τ to align the distal and proximal frames of the complete parallel manipulator in the home position. Shown with appropriate notation in Figure 2.3, each parallel member $\mathbf{M}$ can have any number of links. Individual serial links within the parallel member serial chains are denoted as $M_{j,k}$, in which the first subscript denotes the parent parallel member and the second the relative position of the link within the parallel member.

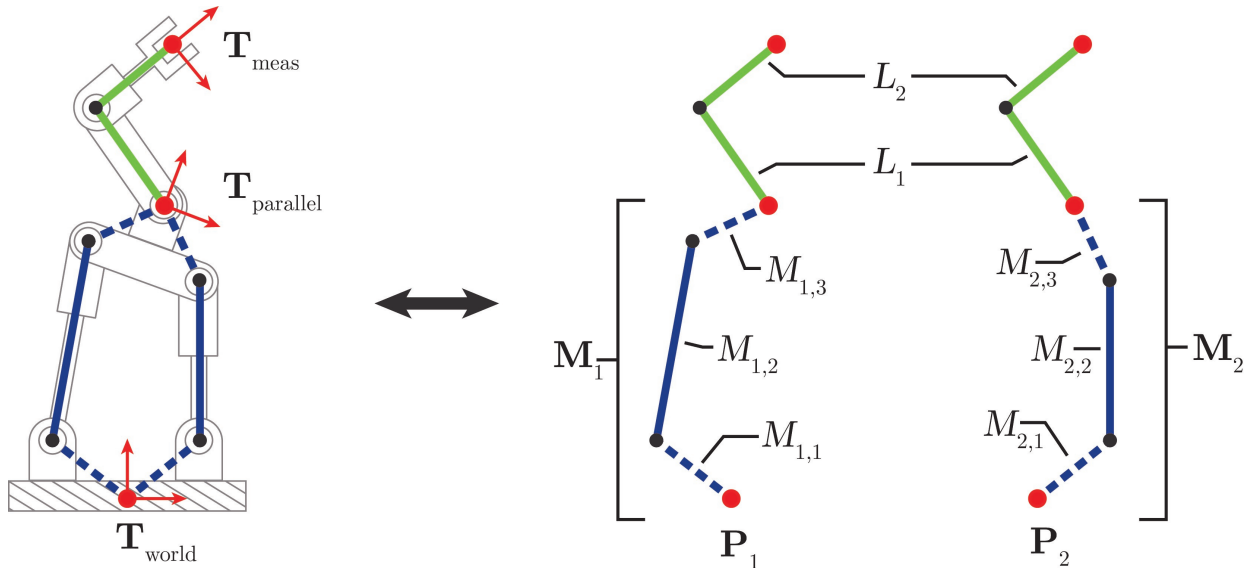

Figure 2.3 Notation representing the hybrid manipulator. Standard serial links are represented in green, with parallel members $\mathbf{M}_1$ and $\mathbf{M}_2$ formed from serial links in blue. Adjustable pose offsets are represented by dashed lines, while serial links are solid. Strictly serial links $\mathbf{L}_1$ and $\mathbf{L}_2$ share parameters across each serial chain. The length of links $M_{1,2}$ and $M_{2,2}$ and the joint angles of links L_1 and L_2 are actuated (active joints, $\boldsymbol{\theta}$). All rotation joints within parallel members $\mathbf{M}_1$ and $\mathbf{M}_2$ are unactuated (passive joints, $\boldsymbol{\psi}$).

The pose of a hybrid manipulator can be described by constructing a serial chain $\mathbf{P}$ composed of any one parallel member and the strictly serial links of the manipulator. In each possible serial chain, the distal and proximal ends of the parallel member as well as the complete hybrid manipulator must remain coincident in any valid configuration as displayed in Figure 2.3. These frame constraints are used to capture the sensitivities of the complete manipulator and allow for calibration.

2.3.3.2 Forward Kinematics

The constraints that drive the passive joints of a parallel manipulator introduce additional nonlinearities into the forward kinematics problem, resulting in numerous valid analytical solutions for any set of input $\boldsymbol{\theta}$ [105]. We avoid the complexity of analytical solutions by implementing a nonlinear least squares inverse kinematics fitting method with the serial chain representation of the parallel manipulator to generate a valid transform for a parallel manipulator. This method allows a single valid solution within the desired workspace to be found quickly in cases with a singularity-free work envelope and a nearby pose approximation. Collision checking for fitted solutions can be conducted quickly due to the proximity to the initial feasible pose.

The forward kinematics fitting process adjusts pose estimate vector $\boldsymbol{\tau}$, corresponding to $\mathbf{T}_{\text{parallel}}$ in Figure 2.3, and passive joint parameters ψ to yield a valid final transform for the parallel manipulator.

This process can be expressed as the optimization problem for the M parallel members as

$$\begin{aligned} \underset{\tau,\,\psi}{\arg\min} \quad & \|\mathbf{E}_{\mathrm{f}}\|^2 \\ \text{subject to} \quad & \mathbf{e}\left(\mathbf{T}_1, \mathbf{T}_m\right) = 0 \;\forall\; m \in \mathbf{M}, \end{aligned} \tag{2.9}$$

where each $\mathbf{T}$ is the transform calculated for an individual parallel member indicated via subscript with associated input set $(\boldsymbol{\phi}, \boldsymbol{\theta}, \boldsymbol{\psi})$. Without loss of generality, we choose a point and quaternion $(\boldsymbol{p}\&\boldsymbol{q})$ formulation of pose to generate singularity-free Jacobians over a small number of parameters. Pose-error terms (2.4), between the distal transform of each parallel member at $\boldsymbol{\psi}$ and the pose guess $\boldsymbol{\tau}$, are minimized to find a convergent forward kinematics solution. The errors for each of the M parallel members of the manipulator are vertically concatenated similar to (2.6) into a single $[6M\times1]$ error vector as

$$\mathbf{E}_{\mathrm{f}} = \begin{bmatrix} \mathbf{e}_1 \\ \mathbf{e}_2 \\ \vdots \\ \mathbf{e}_M \end{bmatrix}. \tag{2.10}$$

The forward kinematic error $\mathbf{E}_{\mathrm{f}}$ is minimized by constructing Jacobian $\mathbf{J}_{\mathrm{f}}$ to adjust both pose estimate and passive joint parameters simultaneously as

$$\mathbf{J}_{\mathrm{f}} = \begin{bmatrix} \mathbf{J}_\tau & \mathbf{J}_{\psi,1} & \dots & \mathbf{0} \\ \vdots & \vdots & \ddots & \vdots \\ \mathbf{J}_\tau & \mathbf{0} & \dots & \mathbf{J}_{\psi,M} \end{bmatrix}, \tag{2.11}$$

where $\mathbf{J}_\tau$ used in this work is provided in Appendix 2.7 and $\mathbf{J}_\psi$ are the horizontally concatenated serial chain velocity Jacobians for the passive joints of the parallel members identified by the second subscript. As active joint values θ are fixed for any given forward kinematics problem, the velocity Jacobian $\mathbf{J}_\theta$ terms are not included. Kinematic parameters $\boldsymbol{\phi}$ are used to generate the error terms, but are absent from this Jacobian formulation as they are not adjusted in this process.

The update step for the fitting process is calculated similarly to (2.7) as

$$\begin{bmatrix} \Delta\boldsymbol{\tau} \\ \Delta\psi \end{bmatrix} = \mathbf{J}_{\mathrm{f}}^{\dagger}\mathbf{E}_{\mathrm{f}}. \tag{2.12}$$

The forward kinematics fitting process terminates when error is reduced below a specified threshold or updates are no longer reducing error by a secondary threshold. To ensure convergence to the expected pose, it is preferable to use a more accurate initial estimate for $\boldsymbol{\tau}$ based on nominal inputs or metrology measurements.

2.3.3.3 Inverse Kinematics

Determining the active joint parameters $\boldsymbol{\theta}$ to reach a specific pose is necessary for motion planning. We extend the inverse kinematics fitting methods developed in the previous section to formulate a constrained

velocity Jacobian that describes a linear relationship between active and passive joint angles and end-effector pose. This allows valid input combinations close to the starting position of the manipulator for a desired pose to be found with nonlinear least squares methods.

The passive joint parameters ψ of a parallel manipulator are required to fully characterize its motion. Provided a valid starting configuration for the parallel manipulator and a desired pose $\mathbf{T}_{\text{des}}$, an identical pose-error $\mathbf{e}$ is calculated using (2.4) for each parallel member. The inverse kinematics fitting process is formulated as

$$\begin{aligned} \underset{\theta,\psi}{\arg\min} \quad & \|\mathbf{e}\left(\mathbf{T}_{\text{des}}, \mathbf{T}_{\text{parallel}}\right)\|^2 \\ \text{subject to} \quad & \mathbf{e}\left(\mathbf{T}_1, \mathbf{T}_m\right) = 0 \; \forall \; m \in \mathbf{M}, \end{aligned} \tag{2.13}$$

where both active and passive joint values are adjusted to reach the desired pose. A valid starting configuration indicates that the distal frames of all constituent parallel members are coincident as displayed by $\mathbf{T}_{\text{parallel}}$ in Figure 2.3.

At a coincident configuration the difference in parallel member final pose (2.10) must be zero, allowing for the relationship between parallel member parameter changes and coincident frame motion to be modelled. The pose estimate Jacobian (2.11) is reframed as a constraint to maintain a coincident frame and expanded to incorporate the active joints of the parallel member θ as

$$\mathcal{C} = \begin{bmatrix} \mathbf{J}_\tau & -\mathbf{J}_{\theta,1} & \dots & \mathbf{0} & -\mathbf{J}_{\psi,1} & \dots & \mathbf{0} \\ \vdots & \vdots & \ddots & \vdots & \vdots & \ddots & \vdots \\ \mathbf{J}_\tau & \mathbf{0} & \dots & -\mathbf{J}_{\theta,M} & \mathbf{0} & \dots & -\mathbf{J}_{\psi,M} \end{bmatrix}. \tag{2.14}$$

To yield a valid coincident pose for the parallel manipulator for a parameter update step (2.7), it must have form

$$\mathcal{C} \begin{bmatrix} \Delta\boldsymbol{\tau} \\ \Delta\theta \\ \Delta\psi \end{bmatrix} = \mathbf{0}, \tag{2.15}$$

which can also be expressed as,

$$M\Delta\mathbf{J}_\tau\boldsymbol{\tau} = \mathbf{J}_\theta\Delta\theta + \mathbf{J}_\psi\Delta\psi, \tag{2.16}$$

where $\mathbf{J}_\theta$ and $\mathbf{J}_\psi$ are the horizontally concatenated Jacobian blocks of M parallel members.

Any change in the coincident frame pose representation $\boldsymbol{\tau}$ directly impacts the total pose-error of the parallel manipulator as defined in (2.4) to an arbitrary frame of interest as

$$\Delta\boldsymbol{e} = \mathbf{J}_\tau\Delta\boldsymbol{\tau}. \tag{2.17}$$

By substitution and matrix manipulation,

$$\Delta \boldsymbol{e} = \frac{1}{M} \begin{bmatrix} \mathbf{J}_\theta & \mathbf{J}_\psi \end{bmatrix} \begin{bmatrix} \Delta\theta \\ \Delta\psi \end{bmatrix}, \tag{2.18}$$

where it becomes apparent that a scaling factor of $\frac{1}{M}$ is necessary to condition the parallel member Jacobians for use in a constrained parallel manipulator.

Nota Bene: this approximation is only valid in cases where the parallel manipulator begins in a constrained state with zero constraint error and does not inherently enforce the constraint with an arbitrary parameter step. The addition of this scaling factor only ensures that the weighting found during the forward kinematics process is expressed during the calibration process, removing the need to generate a specific $\boldsymbol{\tau}$ constraint.

The relationship (2.18) is used in the inverse kinematic fitting process. By considering the active and passive joints of each parallel member of a parallel manipulator separately, a composite velocity Jacobian for independent parallel member motion is defined as

$$\mathbf{J}_{\mathrm{v}} = \frac{1}{M} \begin{bmatrix} \mathbf{J}_\theta & \mathbf{J}_\psi \end{bmatrix}, \tag{2.19}$$

where M represents the number of parallel members that define a parallel manipulator and $\mathbf{J}_\theta$ and $\mathbf{J}_\psi$ are the active and passive joint parameter Jacobians of all constituent parallel members concatenated in the link-wise manner described in (2.5).

While representing the motion of many separate serial chains, the $\mathbf{J}_{\mathrm{v}}$ in (2.19) does not yet capture the constraints of the complete parallel manipulator as each chain can move without impacting the others. For any valid pose, the end-effector frames for each of the parallel members serial chains must remain coincident; no pose-error can exist between them. This constraint is enforced by using the previously calculated Jacobians $\mathbf{J}_\theta$ and $\mathbf{J}_\psi$. To match the column order of (2.19), the constraint matrix for each Jacobian is constructed separately but with identical block structure. The constraint matrix associated with $\mathbf{J}_\theta$ is

$$\mathcal{C}_\theta = \begin{bmatrix} \mathbf{J}_{\theta,1} & -\mathbf{J}_{\theta,2} & \mathbf{0} & \dots & \mathbf{0} \\ \mathbf{J}_{\theta,1} & \mathbf{0} & -\mathbf{J}_{\theta,3} & \dots & \mathbf{0} \\ \vdots & \vdots & \vdots & \ddots & \vdots \\ \mathbf{J}_{\theta,1} & \mathbf{0} & \mathbf{0} & \dots & -\mathbf{J}_{\theta,M} \end{bmatrix}, \tag{2.20}$$

where the second Jacobian subscript identifies the parallel member each block is associated with. The passive joint parameter constraint matrix $\mathcal{C}_\psi$ is generated by substituting the appropriate $\mathbf{J}_\psi$ components for the parallel members into the structure. The individual constraint matrices are combined for final use as

$$\mathcal{C}_{\mathrm{v}} = \begin{bmatrix} \mathcal{C}_\theta & \mathcal{C}_\psi \end{bmatrix}, \tag{2.21}$$

where the column dimension matches that of $\mathbf{J}_{\mathrm{v}}$.

To ensure that no constraint error is generated by updates to θ and ψ, a null space is constructed from the combined constraint matrix and propagated to the combined parallel manipulator velocity Jacobian $\mathbf{J}_{\mathrm{v}}$ as

$$\mathbf{J}_{\mathrm{v}|\mathcal{C}}^{\dagger} = \mathcal{N}\left(\mathcal{C}_{\mathrm{v}}\right)\left(\mathbf{J}_{\mathrm{v}}\mathcal{N}\left(\mathcal{C}_{\mathrm{v}}\right)\right)^{\dagger}, \tag{2.22}$$

where $\mathcal{N}\left(\mathcal{C}_{\mathrm{v}}\right)$ indicates the null space of the input constraint matrix. It should be noted that the null space of a matrix is not unique - any valid null space can be multiplied by a real value to yield another valid solution [106]. The construction of (2.22) can use any valid null space.

For use in the inverse kinematics of hybrid manipulators, this must be converted via a second pseudo-inverse operation to standard form $\mathbf{J}_{\mathrm{v}|\mathcal{C}}$ or calculated in the alternate form

$$\mathbf{J}_{\mathrm{v}|\mathcal{C}} = \left(\mathbf{J}_{\mathrm{v}}\mathcal{N}\left(\mathcal{C}_{\mathrm{v}}\right)\right)\mathcal{N}\left(\mathcal{C}_{\mathrm{v}}\right)^{\dagger}. \tag{2.23}$$

The constrained velocity Jacobian is used to successively calculate parameter steps as shown in (2.7), with the process terminating once $\|\mathbf{E}\|^2$ has fallen below a set tolerance or additional exit conditions are met. If the fitting process fails to converge, the feasibility of the pose should be evaluated. As passive joints are updated during every forward kinematic calculation, components of the constrained velocity Jacobian related to ψ are removed before step calculation, leaving only the desired θ components.

2.3.4 Parallel Manipulator Calibration

The constraint methods implemented for inverse kinematic calculations of parallel manipulators can be used to create a pose-error Jacobian for calibrated kinematic parameters. By imposing kinematic constraints to each of the parallel members of a manipulator, we assemble complete parameterized kinematic information and condition it such that the parallel manipulator acts as a virtual serial link in hybrid manipulator cases.

2.3.4.1 Jacobian Packing

The passive joints of a parallel manipulator are responsible for the characteristic closed-loop kinematics but are seldom fitted with encoders in commercial units. Should the joint angles of one parallel members be completely known, the calibration problem can be solved by a standard serial approach as implemented in [89]. To remove the need for fitting a platform with additional encoders, our work considers these passive joints as an additional set of unknown parameters to be solved for on a pose-by-pose basis. The Jacobians

linked to kinematic parameter and passive joints are emplaced into a composite calibration Jacobian $\mathbf{J}_{\text{cal}}$ as

$$\mathbf{J}_{\text{cal}} = \begin{bmatrix} \mathbf{J}_{\phi,1} & \mathbf{J}_{\psi,1} & \mathbf{0} & \dots & & \mathbf{0} \\ \mathbf{J}_{\phi,2} & \mathbf{0} & \mathbf{J}_{\psi,2} & \dots & & \mathbf{0} \\ \vdots & \vdots & \vdots & \ddots & \vdots & \vdots \\ \mathbf{J}_{\phi,N} & \mathbf{0} & \mathbf{0} & \dots & & \mathbf{J}_{\psi,N} \end{bmatrix}, \tag{2.24}$$

where the second subscript identifies the pose to which the Jacobian is related. Kinematic parameters associated with the standard serial links are separated from those associated with each parallel members and recombined as

$$\mathbf{J}_{\phi,i} = \begin{bmatrix} \mathbf{J}_{\phi,\text{serial}} & \mathbf{J}_{\phi,\text{parallel}} \end{bmatrix}. \tag{2.25}$$

2.3.4.2 Constraint Matrix Construction

The calibration Jacobian matrix $\mathbf{J}_{\text{cal}}$ captures the kinematics of each serial chain within the hybrid robotic manipulator, but ignores the physical constraints that drive the passive joints within the manipulator. Each of the individual parallel members within the parallel manipulator share distal and proximal frames; zero pose-error (2.4) exists between any constituent serial chain at any valid set of joint parameters $\boldsymbol{\theta}$ and $\boldsymbol{\psi}$. Any kinematic parameter $\boldsymbol{\phi}$ changes made during calibration must not violate this zero pose-error constraint. By conditioning $\mathbf{J}_{\text{cal}}$ with the null space of linearized kinematic parameter constraints $\mathcal{C}_\phi$ and passive joint constraints $\mathcal{C}_\psi$, valid parameter steps are enforced.

The format presented in (2.20) is implemented as to calculate $\mathcal{C}_\phi$ and $\mathcal{C}_\psi$ for N pose measurements. These component constraint matrices are packed into a composite matrix in a manner similar to (2.24) with structure

$$\mathcal{C}_{\text{cal}} = \begin{bmatrix} \mathbf{0} & \mathcal{C}_{\phi,1} & \mathcal{C}_{\psi,1} & \mathbf{0} & \dots & \mathbf{0} \\ \mathbf{0} & \mathcal{C}_{\phi,2} & \mathbf{0} & \mathcal{C}_{\psi,2} & \dots & \mathbf{0} \\ \vdots & \vdots & \vdots & \ddots & \vdots & \\ \mathbf{0} & \mathcal{C}_{\phi,N} & \mathbf{0} & \mathbf{0} & \dots & \mathcal{C}_{\psi,N} \end{bmatrix}, \tag{2.26}$$

where the subscripted number indicates the pose with which each Jacobian is associated with. As the serial link kinematic parameters cannot cause error between the parallel members end frames, zeros matrices corresponding to the columns of these parameters are appended to the left hand side of the matrix to match the dimensionality of the standard serial link Jacobians present in (2.24).

When used with hybrid robotic manipulators, the Jacobians used to generate the constraint matrices must represent the error evolution of the distal frames of the parallel members that compose a parallel manipulator rather than that of the hybrid manipulator. Should multiple parallel manipulators be present in the hybrid manipulator, additional sets of constraints are required.

Similarly to the inverse kinematics case, the constrained pseudo-inverse is calculated as

$$\mathbf{J}^{\dagger}_{\mathrm{cal}|\mathcal{C}} = \mathcal{N}\left(\mathcal{C}_{\mathrm{cal}}\right)\left(\mathbf{J}_{\mathrm{cal}}\mathcal{N}\left(\mathcal{C}_{\mathrm{cal}}\right)\right)^{\dagger}. \tag{2.27}$$

While it is necessary to incorporate the passive joint parameters and associated constraints to properly capture the dynamics of a parallel manipulator, the forward kinematics process (Section 2.3.3.2) must be run to acquire updated pose information at the beginning of each calibration loop. To prevent redundant parameter updates, the portions of the pseudoinverse related to these passive ψ parameters are removed as

$$\mathbf{J}^{\dagger}_{\Phi|\mathcal{C}} = [\mathbf{I}\ \ \mathbf{0}]\,\mathbf{J}^{\dagger}_{\mathrm{cal}|\mathcal{C}}, \tag{2.28}$$

where $\mathbf{I}$ is a full-rank identity matrix appropriately sized to match the number of ϕ terms and zeros are appended to reach proper matrix dimensions. In the case where the Jacobian for a single measured pose is generated, notation $\mathbf{J}_{\phi|\mathcal{C}}$ is used. Using the reduced Jacobian form a calibration step is calculated according to (2.7) and added to the parameter estimate from the previous step.

2.3.4.3 Pose-by-Pose Jacobian Generation

In the case of D DoF data collection, the dimensions of the $\mathbf{J}_{\mathrm{cal}}$ and the associated $\mathcal{C}_{\mathrm{cal}}$ are defined as

$$[DMN \times \big(\mathrm{length}\left(\boldsymbol{\phi}\right) + U\mathrm{length}\left(\boldsymbol{\psi}\right)\big)], \tag{2.29}$$

where N is the total number of measured poses and U is the number of parallel manipulator poses requiring a unique $\boldsymbol{\psi}$ solution. For purely random pose selection $N = U$, and the linear growth of the system dictates that $DM > \mathrm{length}\left(\boldsymbol{\psi}\right)$ for the problem to remain defined with a sufficiently large number of pose measurements. If this condition does not exist, multiple pose measurements must be collected for each $\boldsymbol{\psi}$ solution by retaining the parallel manipulator pose while moving the strictly serial links such that $N > U$. The column of shared kinematic parameters ϕ of the strictly serial links results in a linked constraint matrix that does not permit direct simplification, demanding computationally expensive null space and pseudoinverse calculations for (2.27).

To permit the problem to remain computationally tractable for general calibration purposes, we present a method for enforcing the constraint framework on a pose-by-pose basis. Efficient Jacobian generation is accomplished by isolating the parallel manipulators of a hybrid manipulator and analyzing them individually. Serial Jacobians for kinematic parameters ϕ and passive joints ψ are generated for each of the M parallel members and horizontally concatenated to form composite Jacobians $\mathbf{J}_{\phi}$ and $\mathbf{J}_{\psi}$. All Jacobians generated during this process *only* consider the parallel manipulator-values are relative to the proximal frame of the parallel manipulator. These Jacobians are then combined to form unconstrained calibration

Jacobian

$$\tilde{\mathbf{J}}_{\text{cal}} = \frac{1}{M}\begin{bmatrix}\mathbf{J}_\phi & \mathbf{J}_\psi\end{bmatrix}. \tag{2.30}$$

The constraint Jacobians are constructed in the manner proposed in (2.20) as

$$\tilde{\mathcal{C}}_{\text{cal}} = \begin{bmatrix}\mathcal{C}_\phi & \mathcal{C}_\psi\end{bmatrix}. \tag{2.31}$$

The existence of a valid solution for passive joints is required to be present at the time of Jacobian generation. These solutions are generated during each epoch of the calibration process using the forward kinematics approach, and splits the fitting problem to allow for faster operation.

Unlike the prior solution approach, the constraint must be applied in a manner that yields a constrained Jacobian rather than the pseudoinverse calculated in (2.27) and (2.28) as

$$\tilde{\mathbf{J}}_{\phi|\mathcal{C}} = \tilde{\mathbf{J}}_{\text{cal}}\mathcal{N}(\tilde{\mathcal{C}}_{\text{cal}})([\mathbf{I}\ \ \mathbf{0}]\,\mathcal{N}(\tilde{\mathcal{C}}_{\text{cal}}))^{\dagger}, \tag{2.32}$$

where $\mathbf{I}$ is a full-rank identity matrix appropriately sized to match the number of ϕ terms and zeros are appended to reach proper matrix dimensions.

The Jacobian $\tilde{\mathbf{J}}_{\phi|\mathcal{C}}$ generated in this manner is in the parallel manipulator local frame and must be transformed to reflect the geometric position of the manipulator within the hybrid manipulator before use [107]. As implemented, this process transforms the Jacobian with rows corresponding to position and rotation error terms (2.4) as

$$\mathbf{J} = \begin{bmatrix}\mathbf{J_p}\\ \mathbf{J_\Omega}\end{bmatrix} \tag{2.33}$$

to desired world frame, designated as frame 0 within this work, from local proximal and distal frames $\ell - 1$ and ℓ as

$$\mathbf{J}_{\text{world}} = \begin{bmatrix}{}^0\mathbf{R}_\ell & \mathbf{0}\\ \mathbf{0} & {}^0\mathbf{R}_\ell\end{bmatrix}\begin{bmatrix}\mathbf{J_p} - \left[{}^\ell\mathbf{d}_{\ell\to L}\right]_\times \mathbf{J_\Omega}\\ \mathbf{J_\Omega}\end{bmatrix}, \tag{2.34}$$

where the associated rotation matrices $\mathbf{R}$ and position offsets $\mathbf{p}$ are calculated using the other links of the hybrid manipulator.

The Jacobians for each constituent link in the manipulator are horizontally concatenated to yield the final calibration Jacobian. This process, although appearing to be a minor alteration to the methods described in Section 2.3.4 ensures that constrained calibration can be accomplished with sufficiently large pose data sets on manipulators with large numbers of passive joints that require fitting by reducing Jacobian dimensions to

$$[DN \times \text{length}\,(\boldsymbol{\phi})]. \tag{2.35}$$

The Jacobians generated in this manner have been validated to match those generated using numerical parameter perturbation methods.

2.3.5 Pose Uncertainty Estimation

A major contribution of this work is extending the constrained Jacobians described in this work to estimate the pose uncertainty of a calibrated robotic manipulator. We detail the process for propagating covariance matrix representations of known measurement uncertainty in the pose-error (2.4) space and manipulator encoder resolutions at any pose. This is of particular interest in model-based positioning control cases with high accuracy requirements.

Residual pose uncertainty after a calibration is driven in part by measurements with uncertainty being incorporated into the least-squares fitting process. The measurement uncertainties are propagated into the final fitted parameters via the developed calibration Jacobians (2.28) as

$$\mathbf{\Sigma}_{\phi} = \mathbf{J}^{\dagger}_{\Phi|\mathcal{C}} \mathbf{\Sigma}_{p} \left(\mathbf{J}^{\dagger}_{\Phi|\mathcal{C}} \right)^{\top}, \tag{2.36}$$

where Σ_{ϕ} is the covariance matrix for the calibrated kinematic parameters ϕ arranged to match the column order of $\boldsymbol{J}_{\mathrm{cal}|\mathcal{C}}$. The covariance matrix $\mathbf{\Sigma}_{p}$ is constructed by diagonally inserting the covariance matrices for all pose measurements used in the calibration diagonally as

$$\mathbf{\Sigma}_{p} = \begin{bmatrix} \Sigma_{p,1} & & \mathbf{0} \\ & \ddots & \\ \mathbf{0} & & \Sigma_{p,N} \end{bmatrix}, \tag{2.37}$$

where $\mathbf{\Sigma}_{p,n}$ indicates the (DoF $\times$ DoF) covariance matrix associated with an individual pose measurement. In this work, pose covariance matrix is (6×6), with elements ordered to match the pose-error vector (2.4) as $[\boldsymbol{p}_{\mathrm{x}}, \boldsymbol{p}_{\mathrm{y}}, \boldsymbol{p}_{\mathrm{z}}, \mathbf{\Omega}_{\mathrm{x}}, \mathbf{\Omega}_{\mathrm{y}}, \mathbf{\Omega}_{\mathrm{z}}]$. Each of these components is expressed in the units of m^2 and rad^2 for position and rotation error terms, respectively.

Parameter uncertainty information is extended back into error space for measured poses using covariance propagation techniques [101] with general form

$$\mathbf{\Sigma}_{b} = \mathbf{J} \mathbf{\Sigma}_{a} \mathbf{J}^{\top}, \tag{2.38}$$

where $\mathbf{J} = \frac{\partial \mathbf{a}}{\partial \mathbf{b}}$. Pose-error uncertainty is also influenced by the use of digital encoders for joint measurement purposes, as there exists a degree of uncertainty in the final positions of any joint parameter when measured in discrete intervals. The motion of the manipulator due to these variables is described by the constrained velocity Jacobian, the combined standard uncertainty [108] as expressed by pose covariance

estimate is found as

$$\mathbf{\Sigma}_{\text{est}} = \mathbf{J}_{\phi|\mathcal{C}}\mathbf{\Sigma}_{\phi}\mathbf{J}_{\phi|\mathcal{C}}^{\top} + \mathbf{J}_{\text{v}|\mathcal{C}}\mathbf{\Sigma}_{\theta}\mathbf{J}_{\text{v}|\mathcal{C}}^{\top}, \tag{2.39}$$

where $\mathbf{\Sigma}_{\theta}$ is the covariance matrix associated with the encoder uncertainty, and $\mathbf{\Sigma}_{\phi}$ is given by (2.36) above. Mean standard deviation values are calculated from these terms as

$$\bar{\sigma} = \sqrt{\frac{\text{tr}(\mathbf{\Sigma})}{n}}, \tag{2.40}$$

where $\mathbf{\Sigma}$ is the covariance matrix to be analyzed and n is the number of measured DoF. For the pose-error vector defined in (2.4), the position and rotation components can be evaluated separately for unit-dependent operations with $n = 3$. In this work, the scalar quantity produced by using full frame information with $n = 6$ is used as a comparison metric between calibration cases, but are unsuitable for other evaluations due to the meaningless units.

2.3.6 Dependence on Data Set Size

The ultimate goal of a calibration procedure is to reduce the expected pose-error to acceptable levels for a given use case. The post-calibration performance can be described by the covariance of the residual pose-error terms, with low pose-error uncertainty desired for a calibrated model. We analyze the impacts of adding additional pose measurements with known uncertainty characteristics to a calibration data set on the estimated covariance defined in (2.39).

2.3.6.1 Expected Jacobians

There exists substantial variation in robot manipulator construction and scale across industry. Characteristics relating to the convergence of the expected Jacobians for calibrated parameters $\bar{\mathbf{J}}_{\phi|\mathcal{C}}$ and active motion parameters $\bar{\mathbf{J}}_{\text{v}|\mathcal{C}}$ are difficult to generalize with respect to total data set size and must be determined on a case-by-case basis to provide accurate results in the operational volume for the robotic manipulator in question.

A basic algorithmic approach to finding the expected Jacobians is presented in Algorithm 1 and relies on simulated pose generation using the pre-calibration manipulator. This method assumes that only small perturbations are present in the manipulator.

As a data set of N pose measurements increases in size, the expected Jacobians developed above can facilitate analysis of robotic manipulator behavior when used with the covariance matrices above. In a converged state, (2.39) can be rewritten as

$$\bar{\boldsymbol{\Sigma}}_{\text{est}} = \underbrace{\bar{\mathbf{J}}_{\phi|\mathcal{C}}\boldsymbol{\Sigma}_{\phi}\bar{\mathbf{J}}_{\phi|\mathcal{C}}^{\top}}_{\boldsymbol{\Lambda}} + \underbrace{\bar{\mathbf{J}}_{\text{v}|\mathcal{C}}\boldsymbol{\Sigma}_{\theta}\bar{\mathbf{J}}_{\text{v}|\mathcal{C}}^{\top}}_{\boldsymbol{\beta}}. \tag{2.41}$$

Estimated covariance components related to calibration uncertainty ($\boldsymbol{\Lambda}$) and encoder uncertainty ($\boldsymbol{\beta}$) have behavior driven by the calibration fit covariance $\boldsymbol{\Sigma}_{\phi}$ and encoder feedback covariance $\boldsymbol{\Sigma}_{\theta}$, respectively. Calibration uncertainty is primarily driven by uncertainty in the measurements used in the fitting process, while encoder uncertainty exists due to hardware discretization.

Convergence to the expected state is measured by taking the trace of the expected pose covariance matrices $\boldsymbol{\Lambda}$ and $\boldsymbol{\beta}$. As the eigenvalues of a covariance matrix indicate the variance in each principle direction, the trace provides a conservative evaluation method with scalar output for the expected final magnitude of (2.39).

Algorithm 1: Jacobian convergence algorithm

Input : $(\theta_{\text{rand}}, \tau_{\text{rand}})$: Simulated random poses in workspace
Output: $\left(\bar{\mathbf{J}}_{\phi|\mathcal{C}}, \bar{\mathbf{J}}_{\text{v}|\mathcal{C}}\right)$: Converged expected Jacobians
(N_{est}): Estimated number of required pose measurements

```
Initialize N such that measured DoF ≥ calibrated DoF;
while Δtr(Σ_est) > Δ_min do
    Generate N pose measurements;
    for i ∈ N do
        Calculate J_v|C (2.22);
        Calculate J_φ|C (2.27), insert into J̄_cal|C;
    end
    Calculate J̄_φ|C and J̄_v|C via element-wise mean;
    Calculate Σ_est (2.39);
    Calculate tr(Σ_est);
    if Δtr(Σ_est) > Δ_min then
        Increase poses → N = 2N;
    end
end
Return N_est = N;
```

2.3.6.2 Covariance Component Evolution

Calibrated kinematic parameter covariance $\boldsymbol{\Sigma}_{\phi}$ evolves with the number of points N. In the simple case where measurement parameter variance is completely independent, as N increases $\boldsymbol{\Sigma}_{\phi}$ evolves as

$$\boldsymbol{\Sigma}_{\phi} = \frac{1}{N}\boldsymbol{\Sigma}_{p}. \tag{2.42}$$

Covariance terms are introduced into measurement uncertainties by instrument-based term coupling or by rotating a covariance matrix into a meaningful coordinate frame. Due to the shape information that these terms impart to the covariance ellipsoid, they cannot be neglected during analysis. The incorporation of these terms is simplified by using the expected Jacobians and assuming that each pose measurement

covariance $\bar{\mathbf{\Sigma}}_{p,n}$ is static. In the measurement cases where a pose measurement covariance fluctuates, the expected covariance matrix for the pose masurements can be used. By substitution, (2.36) yields

$$\mathbf{\Sigma}_{\phi} \approx \bar{\mathbf{J}}^{\dagger}_{\mathrm{cal}|\mathcal{C}} \bar{\mathbf{\Sigma}}_{p} \left(\bar{\mathbf{J}}^{\dagger}_{\mathrm{cal}|\mathcal{C}} \right)^{\top}, \tag{2.43}$$

where $\bar{\mathbf{J}}_{\mathrm{cal}|\mathcal{C}}$ is composed of $\bar{\mathbf{J}}_{\phi|\mathcal{C}}$ vertically concatenated N times and $\bar{\mathbf{\Sigma}}_{p}$ is composed of expected pose measurement covariance matrix $\bar{\mathbf{\Sigma}}_{p,n}$ emplaced as (2.37).

As N increases, it can be shown that the expectation terms converge and the estimated covariance component related to the calibrated parameters become

$$\mathbf{\Lambda} = \frac{1}{N} \bar{\mathbf{\Sigma}}_{p}. \tag{2.44}$$

In physical manipulators with digital encoders of equal step size, covariance $\mathbf{\Sigma}_{\theta}$ of active motion parameters is an invariable quantity driven by encoder step counts. With a converged expectation for the associated Jacobian, the estimated covariance component $\boldsymbol{\beta}$ is a static term that cannot be reduced by adding additional measurements.

2.3.6.3 Estimated Data Set Size

The approximation (2.44) can be substituted into (2.41) and evaluated in a scalar manner by taking the trace of each matrix. This forms a general relationship of the estimated post-calibration covariance to the number of pose measurements as

$$N = \frac{\mathrm{tr}\left(\bar{\mathbf{\Sigma}}_{p}\right)}{\mathrm{tr}\left(\bar{\mathbf{\Sigma}}_{\mathrm{est}}\right) - \mathrm{tr}\left(\boldsymbol{\beta}\right)}. \tag{2.45}$$

An estimate for the number of data points required to reach a desired pose covariance matrix $\mathbf{\Sigma}_{\mathrm{des}}$ can be found by substituting for $\mathbf{\Sigma}_{\mathrm{est}}$ and evaluating for N. It can be inferred from the relationships above that as $N \to \infty$, $\bar{\mathbf{\Sigma}}_{\mathrm{est}} \to \boldsymbol{\beta}$. Should a desired covariance matrix with a scalar evaluation below that of $\boldsymbol{\beta}$ be entered in (2.45), a negative N will be returned indicating infeasibility.

Variation exists between robotic manipulators that can result in behavior that is poorly characterized by the proposed estimated Jacobian method. The estimated number of pose measurements described above is presented as a guideline only; the actual number of measurements required is dictated by the target manipulator construction and desired post-calibration performance. A sample application of using this methodology is presented in Section 2.4.3 below in a simulated case for validation purposes.

2.4 Experimental Evaluations

2.4.1 Simulated Hybrid Manipulator Description

Algorithm robustness and covariance characteristics are validated by simulating a 12 DoF hybrid robot composed of a 6 DoF 6-RRRPRR parallel manipulator with offset R-R joints similar to that proposed in [80] attached to the end of a midsize industrial 6 DoF serial manipulator. Nominal parameters representative of commercial products are initialized for both manipulators. A manipulator arranged in a similar configuration is displayed in Figure 2.1.

2.4.1.1 Kinematic Model and Parameter Identification

Manufacturing errors are added by perturbing the nominal parameters of the hybrid manipulator. As the tolerances for the commercial robotic manipulators, within this scope, are assumed to be relatively small, kinematic parameters ϕ are perturbed by a uniformly-distributed random amount within the intervals outlined in Table 2.2 and applied on a link-by-link basis within the model before calibration occurs. Values are designed to reflect typical machining tolerances with respect to manipulator cost and scale. Parallel manipulator manufacturing error ranges are based on estimates from prior parallel mechanism design in the literature [109]. Serial manipulator error ranges inflate these values by five times to account for approximate differences in scale. Quaternion parameters are renormalized to unit vector after perturbation. Unperturbed kinematic parameters are used during data set generation and error comparisons.

Table 2.2 Simulated Manufacturing Error Intervals.

Manipulator Type	**Position (μm)**	**Angle (°)**
Serial	± 127	± 0.5
Parallel	± 25.4	± 0.1

Due to the relative complexity of hybrid manipulators, the total number of kinematic parameters used to describe the manipulator can be very large. Although hybrid manipulators can typically be described by a relatively small subset of these parameters, this minimal set of kinematic parameters is dependent on the manipulator configuration and may be unknown. Non-minimal kinematic parameter sets include poorly identifiable parameters that must be addressed to prevent numerical instability from occurring during the calibration process. Jacobian columns associated with poorly identifiable parameters with a condition number above 500 are ignored by zeroing associated singular value components [102]. This method provides an effective way of validating the calibration performance on a variety of manipulator types without extensive parameter set adjustment. A total of 68 kinematic parameters were calibrated, of which

48 were incorporated in the parallel manipulator and evenly distributed to the constituent parallel members. A listing of the calibrated parameters within this case study is found in Table 2.8.

2.4.2 Simulated Pose Data

Repeated calibration testing is facilitated by the generation of 20,000 calibration and 2000 validation simulated pose data sets. Each data sets is randomly generated within feasible active joint space ψ created using the nominal values of the hybrid manipulator, and contain uncertainty-free measurements in the form of forward kinematics solutions in a specified world frame. For parallel manipulators, joint parameters are selected such that a collision-free pose in operational space is formed for each data point.

2.4.2.1 Measurement Uncertainty

Normally distributed error sampled from covariance matrices is added to the simulated measurement data generated within this work. The purpose of creating these uncertain measurements is two-fold: (1) To permit validation of the calibration approach and algorithms by demonstrating that perturbations corresponding to manufacturing errors can be removed from kinematic parameters, and (2) to demonstrate that the post-calibration pose uncertainty will be reduced below that of the data set measurement uncertainty.

Random covariance matrices are generated using a 6 DoF Wishart distribution sampled from an identity matrix [110]. To maintain comparable uncertainty values between trials, each covariance matrix is scaled such that its trace is equivalent in value to that of a base uncertainty case in which only variance terms displayed in Table 2.3 exist at each point. Values are arbitrarily small and chosen to be distinct from one another. The covariance matrix for each pose is ordered to match the DoF error terms found in (2.4).

Table 2.3 Simulated Data Standard Deviations.

Variable:	$\mathbf{p}_x$ **(m)**	$\mathbf{p}_y$ **(m)**	$\mathbf{p}_z$ **(m)**	$\mathbf{\Omega}_x$ **(rad)**	$\mathbf{\Omega}_y$ **(rad)**	$\mathbf{\Omega}_z$ **(rad)**
Std Dev :	4×10^{-5}	3×10^{-5}	2×10^{-5}	5×10^{-5}	6×10^{-5}	7×10^{-5}

2.4.2.2 Impact of Data Set Size on Pose Uncertainty

The relationships between expected pose uncertainty and data set size described in (2.41) and (2.44) are validated by performing Monte Carlo analysis on randomly selected subsets of the simulated data. Calibration and velocity Jacobians are generated for each selected pose along with a single random pose covariance matrix scaled such that its trace matches that of the arbitrary baseline case. The expected Jacobians in each trial are formed by taking the element-wise mean of the respective point-wise matrices.

Trial-invariant covariance matrices representing uniformly distributed encoder uncertainty are included in each trial. The trial covariance traces are combined and converted to percentages of the covariance traces found in the minimum calibration case in which only twelve 6 DoF pose measurements are present. The percentage distributions for trials at specified data point intervals are compared to the baseline encoder uncertainty levels and expected covariance trace values in Figure 2.4.

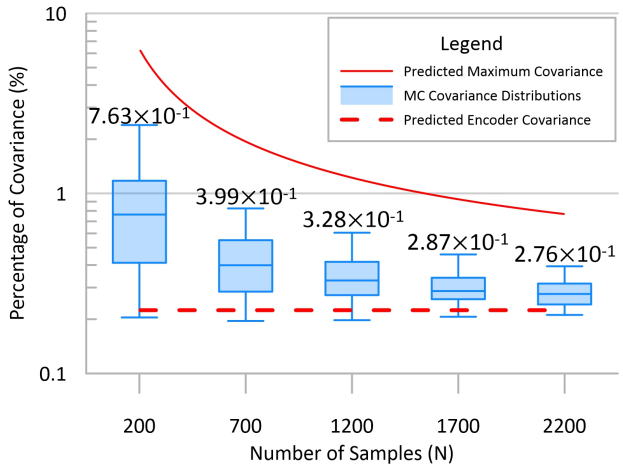

Figure 2.4 Evolution of the trace of expected pose-error covariance with respect to data set size. Values are displayed as a percentage of the expected pose-error covariance found at the minimum necessary calibration data set of twelve 6 DoF poses for the hybrid manipulator. Median values are listed above each distribution. 100 trials were conducted for each N value to generate the actual distributions (blue). Distributions predicted by (2.44) are pictured in red, and show convergence with actual results as $N \to \infty$.

The validation trials display overestimation of final pose covariance for the simulated manipulator. The large workspace volume covered by the simulated points results in a worst-case scenario, as the linear nature of the expected Jacobian cannot fully capture the highly non-linear behavior of the manipulator. As all trial values are bounded by the estimated pose covariance, conservative estimates for calibration data set sizes can be safely generated with (2.45).

2.4.3 Simulated Hybrid Manipulator Calibration

To more robustly test the calibration framework and ensure that convergence is observed over the entire workspace, repeated calibration trials are performed on copies of the perturbed model. A total of 100 trials are completed, with each trial using a 700 pose sub-set of the 20,000 simulated calibration poses. Jacobian dimensions in each trial are defined by (2.35) are $[4200 \times 68]$. The number of poses chosen for each sub-set is informed by the breakpoint for diminishing returns of expected covariance as displayed in Figure 2.4. Each subset is selected randomly without replacement and is generated at the beginning of each trial. Measurement uncertainty is added to each data set during the trial; uncertain data sets are not shared

between trials nor is uncertainty information permanently associated with any individual data point.

Each calibration trial typically reached exit conditions in 3 epochs. Standard Gauss–Newton steps described in (2.7) are taken with a pseudoinverse cutoff ratio of 1:500 used to permit calibration of less observable variables. An additional constraint and error pair corresponding to each calibrated unit quaternion is appended to the previously described calibration Jacobian to ensure that only steps that retain the unit quaternion format are taken.

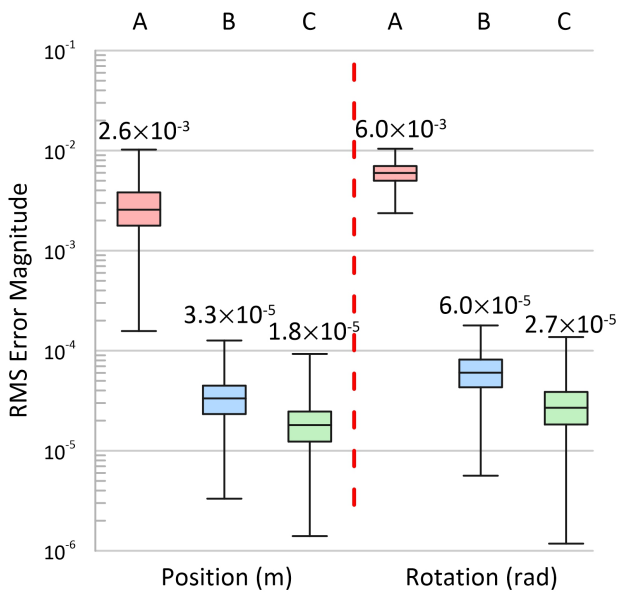

Figure 2.5 Validation data set error distributions for simulated hybrid manipulator calibration. Measurement uncertainty is added to each data point as described in Section 2.4.2. Initial error distributions (red, **A**) are significantly higher than calibrated error distributions (blue, **B**). Error distributions on the same validation data set without measurement uncertainty (green, **C**) indicate that the calibration procedure reduces error below the measurable uncertainty threshold. Median values are listed above each distribution, and a log axis scale is used to present the different magnitudes of data presented.

Each of the calibrated parameterizations is validated with the previously generated set of 2000 validation poses not used within the calibration process. Each trial utilizes the same baseline validation data set, although measurement uncertainty is added independently in each. Pose-error values for each trial are generated for validation data set in cases with and without added measurement uncertainty. A scalar metric of performance is found by separately taking the root-mean-square (RMS) values of the position and rotation components for each generated error vector. The distributions of the RMS pose-error residuals before and after calibration for all trials are displayed in Figure 2.5.

It is important to note that the error terms generated from validation poses without measurement uncertainty fall below those with measurement uncertainty, indicating that for well modelled high precision mechanisms such as parallel manipulators, pose-error becomes bounded by measurement uncertainty

during the fitting process. The calibration fitting process is capable of reducing kinematic pose-error below this measurement uncertainty threshold in cases with sufficiently large data sets. This can best be observed in simulated cases such as presented by merit of being able to generate perfect measurements.

2.4.4 Experimental Manipulator Description

The developed calibration approach is used to characterize a physical hybrid manipulator. Compared to the high-complexity simulation used for validating the calibration approach, this test case demonstrates the procedure's effectiveness with real measurement uncertainties introduced by the metrology system and a nominal parameterization based on a commercial parallel manipulator.

A simple hybrid manipulator was constructed using a commercially available 6-RRRPRR parallel manipulator with offset R-R joints (H-850 6-Axis Hexapod, Physik Instrumente, Karlsruhe, Germany. Commercial products or brand names are only mentioned to clarify what was done in this work. This is not an endorsement of any particular commercial product.)) and rotary stage (ACR240HT-ABS, IntelLiDrives, Philadelphia, PA, USA. Commercial products or brand names are only mentioned to clarify what was done in this work. This is not an endorsement of any particular commercial product.). Both robot components are fully calibrated individually, and represent the state-of-the-art calibration baseline to which we compare our methods.

Pictured in Figure 2.6, the robots were securely mounted together and affixed to a precision optical table. To facilitate multiple data collection methods, laser tracker spherical targets (Red Ring Reflector 0.5″, Leica Geosystems, Norcross, GA, USA. Commercial products or brand names are only mentioned to clarify what was done in this work. This is not an endorsement of any particular commercial product.) were mounted in an asymmetric pattern to the top of parallel manipulator.

2.4.4.1 Encoder Information

Encoder information for each of the actuated joints within the experimental hybrid manipulator is listed in Table 2.4 with calculated variance terms. Each of the legs of the parallel manipulator has identical construction and share a single row. Encoder counts are multiplied by any intermediate gearing to yield final effective resolution. Variance is calculated based on a uniform distribution of width matching one encoder count in the pose-error units of meters and radians.

Table 2.4 Actuated Joint Encoder and Variance Information.

Variable:	**Encoder Resolution**	**Variance**
Rotary Stage	2,097,152 counts/rot	7.4803×10^{-13} rad^2
Prismatic Leg	40,960 counts/mm	4.9671×10^{-17} m^2

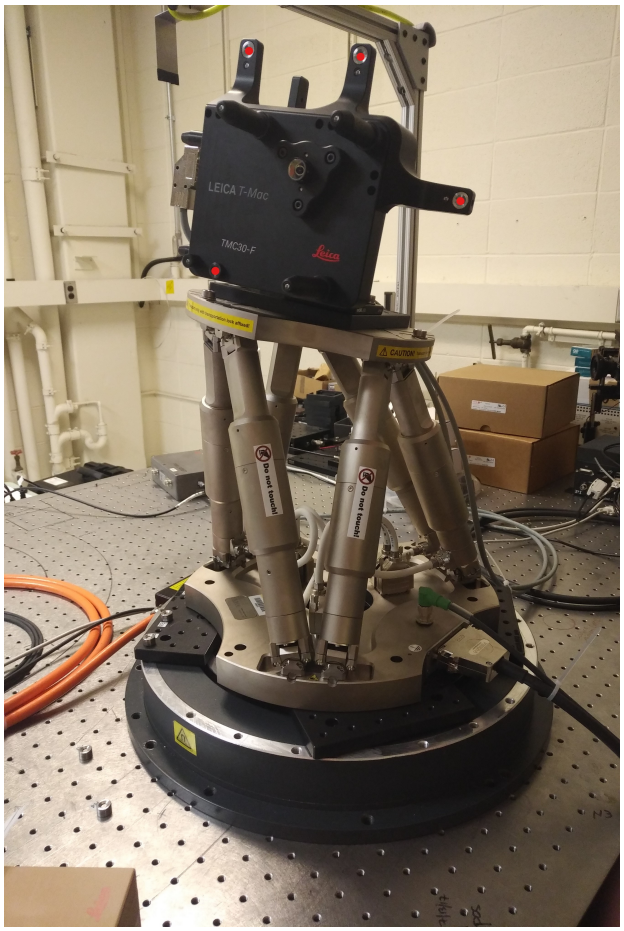

Figure 2.6 Experimental 7 DoF hybrid robotic manipulator constructed from a 6-RRRPRR parallel manipulator with offset R-R joints mounted on a precision rotary stage. Spherical laser tracker target positions are marked with red. Laser tracker is not in view and is positioned approximately 2 meters from the manipulator without visual obstructions.

2.4.4.2 Identification of Coordinate Systems

Consistent world and end-effector frames are necessary for calibration. Although the laser tracker used for pose measurements within this work (Leica Absolute Tracker AT960, Leica Geosystems, Norcross, GA, USA. Commercial products or brand names are only mentioned to clarify what was done in this work. This is not an endorsement of any particular commercial product.) generates a measurement frame, the points can be recorded in reference to an arbitrarily positioned world frame. A coordinate frame with the z-axis nominally centered and normal to the rotary stage motion was defined using 3 DoF measurements recorded during motion. This world frame is referenced to static spherical target monuments (Leica Red-Ring Reflector 0.5“ (Commercial products or brand names are only mentioned to clarify what was done in this work. NIST does not endorse commercial products. Other products may work as well or better.)) attached

to the table in Figure 2.6 and serves as the nominal proximal frame for the hybrid robot model. Frame errors compensated for by positioning the proximal frame with a calibrated offset.

The frame generated by a 6 DoF target at the home position served as the virtual end-effector for the hybrid manipulator and is used to determine the nominal distal offset. To allow for multiple measurement methods, this frame is also referenced to the spatial locations of the four spherical target nests integrated in the sensor.

2.4.4.3 Kinematic Model and Parameter Identification

The parallel manipulator kinematic model is implemented as described above, with parameterization listed in Appendix 2.8. Offsets at the proximal and distal ends of the hybrid manipulator and between manipulator components are calibrated to compensate for the poorly defined initial states. Parameters for each of the manipulators were estimated with physical measurements and available CAD models.

Identifiable parameters within the kinematic model are determined by singular value analysis. Although singular values below a specified threshold of are removed during the pseudoinverse generation process, it is important to reduce the model to a minimal state for increased effectiveness of the calibration process and reduced computation time.

A concatenated calibration Jacobian is generated from an experimental data set described below. To ensure appropriate parameter steps, the column scaling is applied to the Jacobians such that a unitary parameter change would result in an RMS error change of 1×10^{-5} [111]. By identifying the parameters listed as primary components in the $\mathbf{V}$ columns associated with the singular values with a condition number below 1:500, the parameter list is reduced significantly. Several parameters related to parallel member link lengths are retained despite falling below this value for model completeness and to test the impacts of different condition number cutoff points during calibration. It is noted by inspection that many of the poorly identifiable parameters removed overlap with either retained kinematic parameters or passive joint components within individual parallel members. The limited workspace of the experimental parallel manipulator results in the lack of rigorous exercise of all degrees of freedom on parallel members leading to poor identifiability. The permitted condition number is expanded to 1:1000 in the calibration experiments in the interest of capturing some of these poorly identifiable degrees of freedom in the hybrid manipulator throughout the experiments below. A total of 53 kinematic parameters were calibrated, of which 48 were incorporated in the parallel manipulator and evenly distributed to the constituent parallel members. A listing of the calibrated parameters within this case study is found in Table 2.9.

2.4.5 Experimental Pose Data Collection

To allow for accurate measurement of the pose of the robotic manipulator, sets of four laser tracker spherical targets are mounted asymmetrically to the end-effector as shown in Figure 2.6. Each target is measured in 3 DoF by the laser tracker system previously detailed and a 6 DoF end-effector pose is generated by fitting each point cloud to a nominal relationship of the mounting points to a virtual frame definition. A total of 200 randomized poses are generated for the hybrid manipulator within the supported motion ranges such that all of the spherical targets remain in view of the laser tracker system. The hybrid manipulator home position is recorded in this manner and included in the data set. The motion of the rotary stage is constrained to $\pm\frac{\pi}{4}$ radians to prevent cable breakage.

Laser tracker measurement uncertainty is dependent on the distance between the spherical target and the measurement head with manufacturer specification $\pm 7.5\ \mu\text{m} + 3\ \mu\text{m/m}$ for 3 DoF points [112]. A 3×3 covariance matrix $\mathbf{\Sigma}$ is returned by the data collection software for each point measurement, which is converted to mean standard deviation using (2.40). The resultant distribution of uncertainty values calculated in this manner is displayed in Figure 2.7, with low variation observed due to the small workspace of the experimental manipulator.

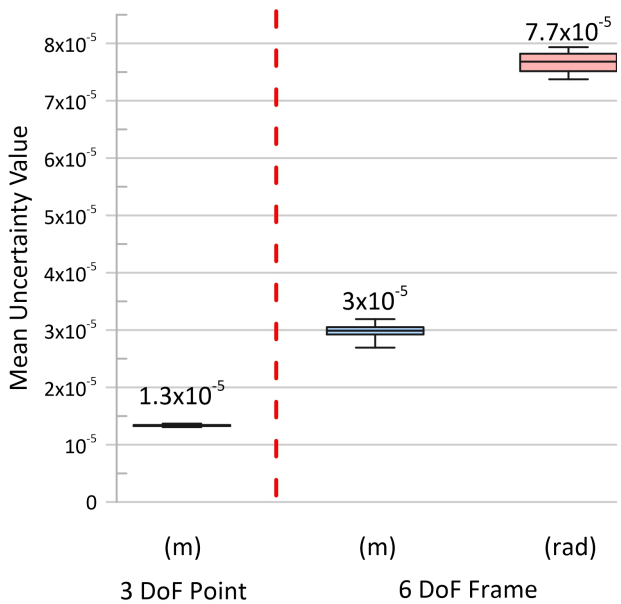

Figure 2.7 Mean uncertainty distributions for the collected data set of 800 point measurements (3 DoF) and the resultant 200 reconstructed frames (6 DoF) used in the experimental calibration of Section 2.4.6. Mean uncertainties are defined as the square root of the trace of a covariance matrix divided by its degrees of freedom (2.40). In the case of the 6 DoF frame reconstruction, the position terms and rotation terms are considered separately to illustrate the relative magnitude of the components. Median values are listed above each distribution.

Encoder values for controllable joint parameters are converted into appropriate input variables θ, with rotary stage position reported with units of radians and parallel manipulator leg-lengths reported with units of millimeters.

2.4.5.1 Frame Reconstruction and Uncertainty

Pose reconstruction is implemented as SVD-based point cloud fitting [113], which calculates the transform between two ordered sets of 3D points while minimizing the least squares error. Provided a known home position in the world frame, the transform between a point groups collected at the hybrid manipulator home position and a calibration pose is used to determine the final pose.

Sets of 3D point measurements acquired by a laser tracker can be used to construct 6 DoF pose measurements. The calculation of pose uncertainties of a 6 DoF pose derived from a set of N point (3D) measurements is detailed below.

For a series of N point measurements, the final covariance matrix for a single pose is represented as

$$\boldsymbol{\Sigma}_m = \begin{bmatrix} \boldsymbol{\Sigma}_1 & \mathbf{0} & \dots & \mathbf{0} \\ \mathbf{0} & \boldsymbol{\Sigma}_2 & \dots & \mathbf{0} \\ \vdots & \vdots & \ddots & \vdots \\ \mathbf{0} & \mathbf{0} & \dots & \boldsymbol{\Sigma}_N \end{bmatrix}, \tag{2.46}$$

where $\boldsymbol{\Sigma}$ is a 3×3 covariance matrix for a point indicated by the subscript.

The relationship between the combined covariances and pose-error as defined in (2.4) is facilitated by representing the transform of a manipulator in the $\boldsymbol{p}\&\boldsymbol{q}$ format detailed in Appendix 2.7. The calibration Jacobian defined for this construct can be utilized to model the uncertainties of the least squares fitting process as

$$\mathbf{J}_{\mathrm{p}} = \frac{\partial \mathbf{e}}{\partial \boldsymbol{\tau}} \left(\frac{\partial \mathbf{p}}{\partial \boldsymbol{\tau}'} \right)^{\dagger} \tag{2.47}$$

where $\frac{\partial \mathbf{e}}{\partial \boldsymbol{\tau}}$ is the $[6 \times 7]$ analytical Jacobian for a $\boldsymbol{p}\&\boldsymbol{q}$ offset link representing the optimal transform as specified in Appendix 2.7. Individual point measurements relative to the frame are added to the $\boldsymbol{p}\&\boldsymbol{q}$ offset separately, with the resulting combinations used to generate an analytical Jacobian at each point. The Jacobian rows related to the position error terms are vertically concatenated to form $\frac{\partial \mathbf{p}}{\partial \boldsymbol{\tau}'}$, a $[3N \times 7]$ matrix where N is the number of 3D point measurements included in point group $\mathbf{p}$.

The combined Jacobian $\mathbf{J}_{\mathrm{p}}$ are used to propagate the measurement covariance using form (2.38) as

$$\boldsymbol{\Sigma}_p = \mathbf{J}_p \boldsymbol{\Sigma}_m \mathbf{J}_p^{\top}, \tag{2.48}$$

where $\boldsymbol{\Sigma}_p$ is a 6×6 matrix which represents the final measurement uncertainties and couplings present in each 6 DoF pose. The order of the terms corresponds to that found within the standard pose-error vector within this work (2.4). The uncertainty distributions for the reconstructed frames used in this calibration

are displayed in Figure 2.7. For the reconstructed frames, the uncertainties associated with the rotation parameters are significantly higher than those related to position terms.

2.4.6 Experimental Hybrid Manipulator Calibration

Calibration of the as-assembled hybrid manipulator was conducted in a two step process. First, errors introduced during assembly are compensated for by calibrating pose offsets introduced between the manipulator components and at the distal and proximal ends of the manipulator. The nominal parameters of the rotary stage and parallel manipulator are not calibrated in this case to preserve the baseline accuracy of the components. Using the full data set inclusive of manipulator home position, this calibration process yields 118 μm RMS position error and 182 μrad RMS rotation error. This offset compensation case is considered representative of the hybrid manipulator accuracy without the calibration techniques developed in this work.

The second step expands the scope of the calibration to include kinematic parameters of the rotary stage and parallel manipulator components in addition to the pose offsets identified in the prior step. Calibration was conducted using a random selection with no replacement of 70% of the data set collected inclusive of the manipulator home position and rounded up. For the subset of 141 poses, calibration Jacobian dimensions as defined by (2.35) are $[846 \times 53]$. The calibration terminated after three epochs upon reaching the parameter change exit condition, with 91.1 μm RMS position error and 64.1 μrad rotation error using a singular value cutoff ratio of 1:1000. The updated parameterization was validated with the remaining 30% of the poses from the original data set that were not used within the calibration process, resulting in 90.4 μm RMS position error and 76.8 μrad rotation error. The calibration process was repeated with the complete 201 point data set, achieving a final 91.1 μm RMS position error and 71.2 μrad rotation error. This represents a 46.7% reduction in error compared to the baseline assembly offset calibration case.

Pose-error distributions for the validation data set are generated for the calibrated and uncalibrated hybrid manipulator and converted into scalar distributions by separately taking the RMS of the position and rotation components of the error vector at each pose. The resultant distributions are displayed in Figure 2.8 and exist near the identified measurement uncertainties for the laser tracker system. Measurement uncertainty cannot be stripped from the measurements outside of simulation, but it is anticipated that the real performance of the calibration falls below the measurement uncertainty of the laser tracker.

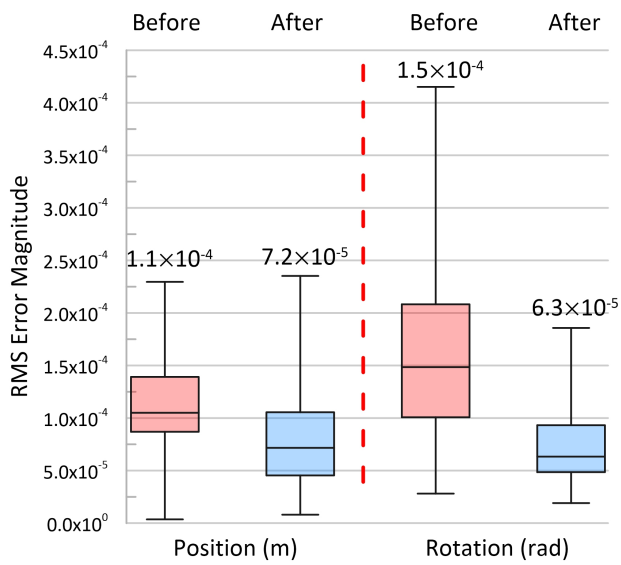

Figure 2.8 Experimental error distributions for validation data set of 60 poses. Significantly larger pose-error distributions exist for the parallel manipulator in both position and rotation using manufacturer calibration (red) when compared to equivalent calibrated quantities (blue). Median values are listed above each distribution.

2.4.7 Comparison to Alternate Calibration Methods

Kinematic loop closure calibration methods are implemented on the parallel manipulator portion of the hybrid manipulator. These established methods have been adapted to the parallel manipulator geometry of interest as demonstrated in [114], but have been widely implemented for use on canonical Stewart Platform manipulator designs [34] and other novel parallel mechanisms [88]. Each implementation minimizes a scalar representation of the position error found within specified kinematic chains, referred to as Position Vector Loop Closure (PVLC) in this work. Within this work, a basic implementation in which the position error between the end effector of each parallel leg $m \in \mathbf{M}$ and the manipulator transform $\mathbf{T}_{\text{parallel}}$ at each measurement is minimized with serial Jacobians generated using the passive joint parameters $\boldsymbol{\psi}$ found by solving the inverse kinematics to reach the measured $\mathbf{T}_{\text{parallel}}$ and actual leg length measurements $\boldsymbol{\phi}$. This configuration is chosen to most closely match contemporary literature. After the loop closure calibration has been completed, the serial manipulator offset calibration is repeated to ensure convergence.

The Nelder–Mead simplex method has been implemented in contemporary literature for final optimization of a novel 6 DoF parallel manipulator after coarse calibration has been completed [93]. This approach is implemented using the MATLAB general minimization function `fminsearch`, with evaluation function corresponding to the RMS of the total pose-error vector $\mathbf{E}$. As no options are specified in the corresponding work, default termination options are retained.

Contemporary literature has implemented Hybrid Genetic Algorithm (HGA) fitting on a variety of parallel manipulators with comparisons to alternate calibration approaches [91]. This approach is composed of genetic algorithm minimization followed by gradient-based constrained minimization facilitated by the MATLAB optimization functions `ga` and `fmincon`, respectively. The option settings are adjusted to a crossover fraction of 0.7, a population size of 100 with 3000 maximum generations. Function tolerance is specified to 1×10^{-100} , with hybrid function specified to use SQP. As the use of genetic algorithm methods greatly impacts computational performance, a trial calibration is also performed with only the gradient-based `fmincon` function for comparison purposes. Options are identical to the prior case. Parallel computation is enabled to improve optimization performance for both related test cases.

The final pose-error found by each of the described calibration approaches and associated computation time are listed and compared to both the baseline hybrid manipulator parameterization and our approach (Constrained NLS) in Table 2.5. In the Nelder–Mead, HGA, and fmincon cases, the pose-error of the manipulator was not reduced from the baseline parameterization. Results for these comparisons are discussed in the following section.

Table 2.5 Alternate Calibration Method Comparison.

Calibration Type	**RMS Pos. Error (μm)**	**RMS Rot. Error (μrad)**	**Runtime * (s)**
Constrained NLS	91.1	71.2	14.9
Serial NLS † [25]	118	182	10.8
PVLC ‡ [88–90]	133	168	104
Nelder–Mead [93]	118	182	5150
HGA [91]	118	182	6280
fmincon [91]	118	182	161

* Single run timing on MATLAB 2018b with Intel-i7-4700MQ CPU@2.40GHz and 32 GB Memory, † Calibration of assembly offsets using serial manipulator techniques to reach baseline parameter set, ‡ Best result with early termination.

2.5 Discussion

2.5.1 Alternate Calibration Methods

To compare our calibration approach to the methods outlined above, it is important to note operational behavior of each type. As [88] and later [81] noted, the closed loop calibration method without passive joint measurements can fail to converge for some parameter sets. Similar behavior was found in the experimental calibration of the hybrid manipulator, with pose-error of the manipulator increasing as the position-based loop residuals were reduced. This behavior matches the prior observations that such methods were very sensitive to measurement noise. Simple cases in which the measured end-effector position of the parallel manipulator are used to perform loop closure on individual kinematic chains cannot generally be applied

unless parameter sets are carefully selected and tested and typically only minimize position components of the total pose-error of interest. Slow convergence is noted due to the updates to the estimated passive joint parameters and lack of consideration for such changes in each kinematic parameter update step.

Non-gradient optimization methods based on the Nelder–Mead simplex algorithm have been implemented within the MATLAB environment over the selected parameter set with an evaluation function corresponding to the RMS of the total pose-error residuals. The evaluation function was not improved on a relevant scale during calibration , with 1.1709×10^{-17} of calculated RMS reduction, and exited after 438 iterations after convergence. Two factors hamper the effectiveness of this direct-search method: the large dimensionality of the calibrated kinematic parameters, which greatly slows the performance of the search, and the presence of a local minima at the initial minimization conditions created by the baseline calibration pass. Although simplified kinematic parameter sets can be used to improve the performance of this method, the high dimensionality and very nonlinear behavior of parallel manipulators makes this approach unsuitable for general use.

The hybrid genetic algorithm fitting method is a general optimization method employed over the selected parameter set with the evaluation function to be minimized corresponding to the RMS of the total pose-error residuals. When implemented with the options detailed in [91], the genetic algorithm component did not reduce pose-error from the baseline case, and the subsequent `fmincon` constrained optimization routine exited after one iteration due to minimum step tolerances below the specified 1e-7. Once again, the local minima of the starting conditions generated by the baseline serial pose-error calibration case are difficult to escape. Parallelization helps offset the cost of the genetic algorithm component, but computation time is longer than any other minimization method due to its inclusion.

A direct call to `fmincon` yields identical results significantly faster. This method uses minimization methods on a gradient numerically calculated for the evaluation function. This gradient-based approach suffers from compressing the pose-error dimensions and the direct computation approach, in which parameter steps are used to approximate the gradient. As seen in the Serial NLS calibration case, parameter updates can increase position error while reducing rotation error. When evaluating the total pose-error vector as a scalar quantity, this information is lost. The direct computation of this gradient on a highly nonlinear system compounds the problem, resulting in early termination due to step sizes falling below the specified threshold of 1×10^{-7} .

2.5.2 Application Overview

The calibration and kinematic framework presented is modular and can be applied to any robot manipulator construction. Extensive testing on cases with multiple parallel manipulators or nested parallel

constructions are outside of the scope of the intended application of this work and are omitted from consideration during validation process. Case-by-case evaluation must be conducted to determine an efficient implementation for these algorithms.

2.5.3 Uncertainty Conclusions

The calibration process in both simulated and experimental cases yielded calibrated pose uncertainty near that of the measurement system when validation poses with measurement uncertainty were used. In the case of the simulated data without measurement uncertainty, it is noted that the pose-error falls significantly below this mark, indicating that the calibration procedure is capable of reducing error below the measurable threshold. As all real measurements contain uncertainty, this motivates the modelling of post-calibration uncertainty to inform pose selection and data set size to reach desired uncertainty levels below measurable levels. Although this process cannot impact the pose uncertainty caused by discrete encoder counts, it minimizes the uncertainty added by physical phenomenon such as gravitational loading and bending effects that are captured in pose measurements. Pose-error introduced by these phenomenon are captured during data collection and minimized by the kinematic parameter calibration, resulting in parameters that best capture the kinematic performance of the manipulator but may not directly correspond to physical dimensions.

In the experimental test case, the calibrated uncertainty remains above the measurement uncertainty values. The limited workspace of the experimental hybrid manipulator does not permit all joints to be extensively exercised, resulting in low identifiability of the parameters during the calibration process. Joint motion is further limited by the data collection process as all spherical targets must maintain line-of-sight with the measurement system. Alternate configurations that permit additional joint motion during measurement, such as altering spherical target placement or incorporating measurements from a secondary laser tracker unit, will increase parameter identifiability and reduce final calibrated uncertainty.

2.5.4 Future Work

The pose covariance model discussed in this work as a method of determining post-calibration pose uncertainty can be extended to include all possible poses through simultaneous fitting of the measurement uncertainty model. Given a series of pose measurements with pose uncertainty, a cyclic fitting process such as expectation-maximization can be applied to a parameterized representation of the measurement system during the calibration process [115]. The resultant model can be used to characterize measurement uncertainty - and therefore calibrated pose uncertainty - over the entire workspace. This can be used to determine more accurate bounds for estimated calibration data set sizes or pose selection and path

planning that minimizes known uncertainty.

2.6 Conclusions

A unified and computationally efficient calibration framework based on null space constraint propagation was developed that extends established serial manipulator techniques to parallel and hybrid manipulators composed of both parallel and serial manipulators. Kinematic models based on this approach were presented and validated on both simulated and experimental hybrid manipulators. Notably, a reduction to 91.1 μm RMS position error and 71.2 μrad RMS rotation error was observed using the methods outlined in this work. A generalized uncertainty estimation framework was also developed that can accurately characterize the residual uncertainty found at calibrated poses or those measured with known uncertainty. This model was used to guide the calibration data set size selection to meet desired uncertainty levels in the case studies.

2.7 Point-Quaternion Links

It is useful to have a serial link representation to model 6 DoF offsets between actuated links. A convenient vector-based parameterization of this lies in the point and quaternion ($\boldsymbol{p}\&\boldsymbol{q}$) pair. Given a basic homogeneous transformation matrix

$$\mathbf{T} = \begin{bmatrix} \mathbf{R} & \mathbf{d} \\ \mathbf{0} & 1 \end{bmatrix}, \tag{2.49}$$

the equivalent $\boldsymbol{p}\&\boldsymbol{q}$ representation is defined as

$$\boldsymbol{\tau} = \begin{bmatrix} \mathbf{d} \\ \mathbf{Q} \end{bmatrix} \tag{2.50}$$

where $\mathbf{Q} \leftrightarrow \mathbf{R}$. The quaternion vector $\boldsymbol{Q}$ contains all related terms arranged as

$$\mathbf{Q} = \begin{bmatrix} q_0 \\ q_1 \\ q_2 \\ q_3 \end{bmatrix}, \tag{2.51}$$

with related subset vector $\mathbf{q}$ containing only terms q_1, q_2, q_3.

Conversions to quaternion space from rotation matrices and vice versa are detailed in [116]. For compactness in later formulas, the components of the $\boldsymbol{p}\&\boldsymbol{q}$ pair are emplaced into a $[7 \times 1]$ vector as

$$\boldsymbol{\tau} = \begin{bmatrix} p_x & p_y & p_z & \boldsymbol{Q}^\top \end{bmatrix}^\top. \tag{2.52}$$

For calibration purposes, the Jacobian relating the $\boldsymbol{p}\&\boldsymbol{q}$ parameter vector $\boldsymbol{\tau}$ to the pose-error defined in (2.4) relative to the end-effector frame is defined as

$$\mathbf{J}_{\boldsymbol{\tau}} = \begin{bmatrix} {}^L\mathbf{R}_\ell & \mathbf{v} \\ \mathbf{0} & {}^L\mathbf{R}_{\ell-1}\boldsymbol{\omega} \end{bmatrix}, \tag{2.53}$$

where $\boldsymbol{\omega}$ reflects the rotation generated by adjusting the quaternion as

$$\boldsymbol{\omega} = 2\begin{bmatrix}-\mathbf{q} & q_0\mathbf{I} - [\mathbf{q}]_\times\end{bmatrix} \tag{2.54}$$

and $\mathbf{v}$ reflects the translation resulting from the rotation as

$$\mathbf{v} = -\,{}^{L}\mathbf{R}_{\ell-1}\left[{}^{\ell-1}\mathbf{d}_{\ell-1\to L}\right]_\times \boldsymbol{\omega}. \tag{2.55}$$

This Jacobian must be converted from the distal frame to the world frame as detailed in (2.34).

2.8 Supplementary Case Study Information

In this work, the moving links of serial manipulators are represented with a combination of classic Denavit–Hartenberg [20] and Hayati [21] parameters to allow for enhanced calibration sensitivity across links with both perpendicular and parallel end frames. Point-Quaternion links are used for all calibrated offsets. Manipulator model link types are abbreviated for use in this appendix according to Table 2.6.

Table 2.6 Link Type Abbreviations.

Link Type	**Motion Type**	**Abbreviation**	**Offset Parameter**
Denavit–Hartenberg	Rotation	DHR	θ
	Prismatic	DHP	d
Hayati	Rotation	HR	θ
	Prismatic	HP	d
Point-Quaternion Offset	None	PQ	None

The symbolic definitions of the analytical pose-error Jacobians based on [25] for each of the link representations used in this work are presented below in Table 2.7 to aid in implementation. Each symbolic term produces a $[6 \times 1]$ vector with elements ordered as (2.4). The γ term offsets the active joint position, and uses the same Jacobian definition as the offset parameter identified in Table 2.6.

Table 2.7 Symbolic Jacobian Definitions.

Parameter	$\boldsymbol{a}$	$\boldsymbol{\alpha}$	$\boldsymbol{\beta}$	$\boldsymbol{d}$	$\boldsymbol{\theta}$
Denavit–Hartenberg [20]	$\begin{bmatrix}\mathbf{x}_n^i \\ 0\end{bmatrix}$	$\begin{bmatrix}\mathbf{x}_n^i \times \mathbf{b}_n^i \\ \mathbf{x}_n^i\end{bmatrix}$	NA	$\begin{bmatrix}\mathbf{z}_{n-1}^i \\ 0\end{bmatrix}$	$\begin{bmatrix}\mathbf{z}_{n-1}^i \times \mathbf{b}_{n-1}^i \\ \mathbf{z}_{n-1}^i\end{bmatrix}$
Hayati [21]	$\begin{bmatrix}\mathbf{x}_n^{'i} \\ 0\end{bmatrix}$	$\begin{bmatrix}\mathbf{x}_n^{'i} \times \mathbf{b}_n^i \\ \mathbf{x}_n^{'i}\end{bmatrix}$	$\begin{bmatrix}\mathbf{y}_n^i \times \mathbf{b}_n^i \\ \mathbf{y}_n^i\end{bmatrix}$	NA	$\begin{bmatrix}\mathbf{z}_{n-1}^i \times \mathbf{b}_{n-1}^i \\ \mathbf{z}_{n-1}^i\end{bmatrix}$

Within these expressions, $\mathbf{b}_n^i$ is a vector from the nth coordinate system to the distal frame of the manipulator at pose i, and $\mathbf{x}_n^i$ and $\mathbf{z}_n^i$ are the first and third columns of the rotation matrix from the distal frame to the current link frame, respectively.

Tabulated descriptions of the hybrid manipulator models calibrated in Sections 2.4.3 and 2.4.6 are listed below to provide more complete case study information. Values associated with each kinematic parameter are omitted.

Cells marked with '1' indicate that the parameter is calibrated, while '0' indicates an uncalibrated parameter. Blank cells indicate that parameters are not present in the link designated at the current row. Active and passive joint variables are designated with an 'A' or 'P', respectively. No quaternion parameters $\mathbf{Q}$ are calibrated in the presented case studies, with the associated column is omitted for spacing purposes. All 6 parallel members have identical construction and calibrated parameters, but parameter values are not linked.

Simulated case study parameters are indicated in Table 2.8, in which a total of 68 kinematic parameters are calibrated, of which 48 are incorporated in the parallel manipulator. Experimental case study parameters are indicated in Table 2.9, in which a total of 53 kinematic parameters are calibrated, of which 48 are incorporated in the parallel manipulator. The initial experimental calibration case that exclusively adjusted offset links was expanded to include all $\mathbf{p}$ and $\mathbf{Q}$ components.

Table 2.8 Simulated Hybrid Manipulator Parameters.

Link	**Type**	**Variable**						
		$\boldsymbol{a}$	$\boldsymbol{\alpha}$	$\boldsymbol{\beta}$	$\boldsymbol{d}$	$\boldsymbol{\theta}$	$\boldsymbol{\gamma}$	$\mathbf{p}$
Serial Arm	DHR	1	1		1	A	1	
	HR	1	1	1		A	1	
	DHR	1	1		1	A	1	
	DHR	1	1		1	A	1	
	DHR	1	1		1	A	1	
	HR	0	0	0		A	0	
Parallel Member	PQ							[1,1,0]
	DHR	1	0		0	P	0	
	DHR	0	0		0	P	0	
	HP	0	0	0	A	0	1	
	DHR	0	0		0	P		
	DHR	1	0		0	P		
	DHR	0	1		0	P		
	PQ							[1,1,0]

As both the simulated and experimental studies use the same parallel manipulator construction, example concatenated Jacobian blocks $\mathbf{J}_{\boldsymbol{\phi}}, \mathbf{J}_{\boldsymbol{\psi}}, \mathbf{J}_{\boldsymbol{\theta}}$ for this system are provided guidance for translating the parameters found in Table 2.8 and Table 2.9. Links are labelled relative to their position in the parallel member kinematic chain $\forall\, m \in \mathbf{M}$.

$$\mathbf{J}_{\boldsymbol{\phi},m} = \begin{bmatrix} J_{\mathbf{p},m,1} & J_{a,m,2} & J_{\gamma,m,4} & J_{1,m,6} & J_{\alpha,m,7} & J_{\mathbf{p},m,8} \end{bmatrix} \tag{2.56}$$

$$\mathbf{J}_{\boldsymbol{\psi},m} = \begin{bmatrix} J_{\theta,m,2} & J_{\theta,m,3} & J_{\theta,m,5} & J_{\theta,m,6} & J_{\theta,m,7} \end{bmatrix} \tag{2.57}$$

$$\mathbf{J}_{\boldsymbol{\theta},m} = \begin{bmatrix} J_{d,m,4} \end{bmatrix} \tag{2.58}$$

Table 2.9 Experimental hybrid manipulator parameters.

Link	**Type**	**Variable**						
		$\boldsymbol{a}$	$\boldsymbol{\alpha}$	$\boldsymbol{\beta}$	$\boldsymbol{d}$	$\boldsymbol{\theta}$	$\boldsymbol{\gamma}$	$\mathbf{p}$
Proximal Offset	PQ							[1,1,0]
Rotary Stage	HR	1	0	0		A	0	
Int. Offset	PQ							[0,0,1]
Parallel Member	PQ							[1,1,0]
	DHR	1	0		0	P	0	
	DHR	0	0		0	P	0	
	HP	0	0	0	A	0	1	
	DHR	0	0		0	P		
	DHR	1	0		0	P		
	DHR	0	1		0	P		
	PQ							[1,1,0]
Distal Offset	PQ							[0,0,1]

CHAPTER 3

CALIBRATING UNCERTAINTY IN ROBOT KINEMATICS AND POSE MEASUREMENTS WITH EXPECTATION-MAXIMIZATION

A paper in review by the NIST Editorial Review Board before of submission to IEEE Transactions on Robotics.

Benjamin L. Moser [4], Joshua A. Gordon [5] and Andrew J. Petruska [6]

3.1 Abstract

We present a method to validate the measurement uncertainty of a metrology instrument without *a priori* estimates in the context of a kinematic calibration using Expectation-Maximization methods and extend our results to characterize post-calibration pose uncertainty for the manipulator throughout a workspace. This technique permits the robot kinematic model to be fitted simultaneously with a parameterized uncertainty model derived from direct-drive laser tracker kinematics. We demonstrate the performance of this algorithm in a simulated and experimental setting, achieving $6.4\,\mu m$ position and $70.8\,\mu rad$ rotation error for kinematic calibration and statistically validating the fitted uncertainty model for points throughout the calibrated workspace.

3.2 Introduction

Robotic systems are increasingly implemented for high accuracy positioning applications in the manufacturing and scientific fields. High frequency antenna metrology presents a contemporary ultra-high-precision use case for robotic positioning. Many state-of-the-art robotic antenna ranges rely on industrial manipulators, e.g. the hybrid manipulator in Figure 3.1, which exhibit an attractive combination of cost, work volume, and ease of integration [4, 13]. As measurement frequency increases, the one hundredth of a wavelength ($\frac{\lambda}{100}$) positioning accuracy metric for antenna pattern reconstruction [15] often exceeds the typical positioning accuracy specifications of the constituent robotic manipulators. External feedback systems [7, 14] and kinematic calibration [58] are implemented to achieve the required positioning accuracy during scanning. The final pose uncertainty relies on the measurement uncertainty of the position

[4] PhD Candidate in Mechanical Engineering at Colorado School of Mines in Golden, CO. Primary author responsible for study conceptualization, system hardware/software design, experimental design, overseeing and conducting data collections, analyses, results interpretation, and manuscript preparation.

[5] Group Leader for the Electromagnetic Fields Group at the National Institute of Standards and Technology in Boulder, CO. Responsible for project administration, system hardware acquisition, and manuscript revisions

[6] Associate Professor and Director of M^{3}Robotics Laboratory in Mechanical Engineering at Colorado School of Mines in Golden, CO. Advisor to primary author. Responsible for project administration, study conceptualization, results interpretation, and manuscript revision.

feedback or position measurements and is a critical input for the antenna pattern reconstruction. Accordingly, it is necessary to validate the performance of these complex, multi-robot systems by characterizing this measurement uncertainty beyond manufacturer-supplied specifications. This work's contribution is methods to create a model fit for pose measurement uncertainty in the context of a robotic kinematic calibration to provide enhanced positioning accuracy with estimates of pose measurement uncertainty in a workspace of interest.

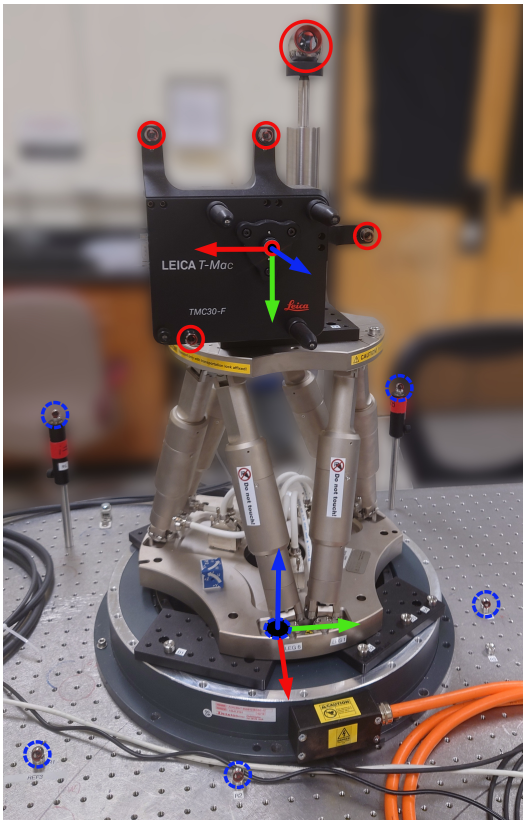

Figure 3.1 7 Degree of Freedom (DoF) hybrid robot manipulator used as the basis for simulated and experimental studies. We fit kinematic parameters and a laser tracker uncertainty model simultaneously using an EM algorithm. World frame is aligned axially with rotary stage motion and referenced to 5 statically mounted SMRs indicated with blue dashed line. End effector frame is referenced to 5 SMRs indicated with red solid line. A laser tracker (out of frame) is positioned to provide visibility of all targets.

Unlike traditional calibration approaches that use the standard, conservative, pose-independent, measurement uncertainties for the weighted-least-squares calibration, we propose here to use Expectation-Maximization (EM) to calibrate measurement uncertainty models in parallel with the robotic parameterization. Then we propose that these calibrated uncertainty models can be statistically verified with validation data sets and compared to the reported measurement uncertainty to quantify the quality of the resulting calibration. Linearized uncertainty propagation allows post-calibration pose uncertainty to be

evaluated over the calibrated workspace and inform typical robot operation without additional feedback from external metrology systems. These techniques assist in determining the ultimate measurement bounds for a given robotic antenna range and minimizing final antenna pattern uncertainty when integrated into digital-twin environments [13] or cases with highly-reconfigurable robot positioning [14].

The primary contribution of this work is a demonstration of measurement uncertainty modelling and fitting during simulated and experimental kinematic calibrations using our EM algorithm. Our technical contribution consists of the creation of a first-order uncertainty model for a direct drive laser tracker, the extension of existing 6 Degree of Freedom (DoF) calibration techniques to a series 3 DoF point measurements to directly link measurements to the calibration process, and the use of uncertainty propagation techniques to combine the uncertainties associated with a series of 3 DoF measurements into 6 DoF space for total pose analysis. Our studies show that our approach can retrieve measurement uncertainty fits that match manufacturer specifications using only calibration fitting residuals. This technique permits rapid estimation or validation of measurement uncertainty statistics from general calibration pose data sets.

Table 3.1 Notation summary. Matrix size is displayed in brackets before description and subscripts provide contextual definitions.

Symbol	**Description**
$\mathbf{R}$	[3×3] Rotation matrix
$\mathbf{d}$	[3×1] Cartesian displacement vector
$\mathbf{T}$	[4×4] Homogeneous transformation matrix
$\boldsymbol{\tau}$	[7×1] Position and Quaternion transform
$\mathbf{e}$	Pose-error vector
$\mathbf{J}$	Jacobian matrix
ϕ	Vector of all kinematic parameters
θ	Vector of all actuator inputs
v	Subscript denoting velocity Jacobian
A	Number of robot links
B	Metrology Instrument Measurement Frame
L	Local projected measurement frame
K	Number of ϕ terms for a link
M	Number of measurement poses within a data set
N	Number of points contained in a point bundle
p	Subscript denoting pose-error

This paper is structured as follows. We first detail the algorithm for the fitting methodology, focusing on the uncertainty modelling and the subsequent reconstruction of 6 DoF pose information from a series of 3 DoF point measurements. We then validate the model on a simulated and experimental test case using a high precision 7 DoF hybrid robotic system and laser tracker measurements. For convenience, the notion used throughout this paper is summarized in Table 3.1.

3.3 Methods

3.3.1 Uncertainty Propagation

We form an estimate of the total pose covariance of the robot manipulator by combining uncertainty sources propagated into the pose-error space using appropriate Jacobians. Within this work, we focus on the uncertainty contributed by the effective measurement uncertainty and encoder quantization. The total pose covariance estimate at any pose is given as

$$\mathbf{\Sigma}_{\text{est}} = \mathbf{J}_{\phi}\mathbf{\Sigma}_{\phi}\mathbf{J}_{\phi}^{\top} + \mathbf{J}_{\text{v}}\mathbf{\Sigma}_{\theta}\mathbf{J}_{\text{v}}^{\top}, \tag{3.1}$$

where $\mathbf{J}_{\phi}$ is the pose-error Jacobian for the robot kinematic parameters, $\mathbf{J}_{\text{v}}$ is the pose-error Jacobian for the robot joint parameters, and $\mathbf{\Sigma}_{\theta}$ is the covariance matrix generated from the encoder resolution and gearing. Kinematic parameter covariance $\mathbf{\Sigma}_{\phi}$ is defined as

$$\mathbf{\Sigma}_{\phi} = \mathbf{J}_{\phi}^{\dagger}\mathbf{\Sigma}_{p}\left(\mathbf{J}_{\phi}^{\dagger}\right)^{\top}, \tag{3.2}$$

where $\mathbf{\Sigma}_{p}$ is the measurement covariance for a particular calibration pose. By substituting (3.2) into (3.1), $\mathbf{\Sigma}_{p}$ is found as

$$\mathbf{\Sigma}_{p} = \mathbf{\Sigma}_{\text{est}} - \mathbf{J}_{\text{v}}\mathbf{\Sigma}_{\theta}\mathbf{J}_{\text{v}}^{\top}. \tag{3.3}$$

To calculate the Jacobian components for the uncertainty propagation, we utilize analytical pose-error Jacobians based on a common serial calibration framework [25]. This analytical approach reduces computation time and produces more accurate results than direct computation, and has been extended to parallel and hybrid manipulators [117]. Additional modelled uncertainty components can be directly added into the covariance estimate (3.1) and extended to (3.3).

3.3.2 Data Acquisition and Processing

3.3.2.1 Direct Drive Laser Tracker Kinematics

Common measurement instruments used in robot kinematic calibration include laser trackers, stereo photogrammetry systems, and draw wire distance sensors. Any metrology instrument with an associated measurement uncertainty model can be used with our EM fitting approach; within this work we demonstrate our algorithm using measurements collected using a direct drive laser tracker system. This instrument provides 3D position measurements or full 6D pose measurements with integrated computer vision systems. A significant body of work has emerged to characterize the performance of these instruments with the intent of standardizing performance metrics and expectations across the industry [59, 118].

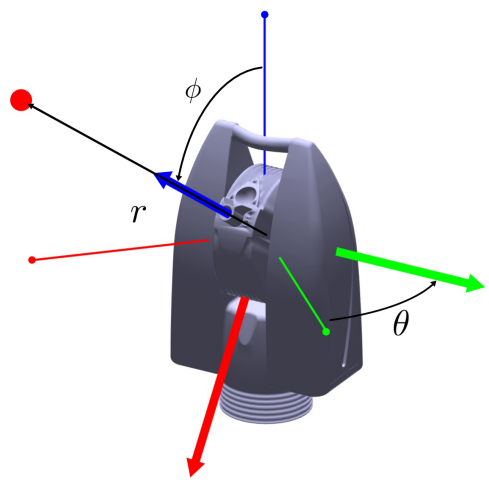

Figure 3.2 An example of the rotation of a direct-drive metrology instrument (${}^{B}\boldsymbol{R}_{L}$) to achieve measurement of a point denoted by the red sphere. A similar direct drive laser tracker system is used to collect point measurements within this work.

3D point measurements collected by a direct drive laser tracker are natively described with the parameters θ, ϕ, r as displayed in Figure 3.2. Given an arbitrary point $\boldsymbol{d}$ in the instrument frame B, these quantities can be directly calculated using the inverse kinematics as

$$\hat{\boldsymbol{d}} = \frac{\boldsymbol{d}}{\|\boldsymbol{d}\|} \tag{3.4}$$

$$\theta = \arctan \frac{\hat{\boldsymbol{d}}_2}{\hat{\boldsymbol{d}}_1} \tag{3.5}$$

$$\phi = 2 \arctan \sqrt{\frac{1 - \hat{\boldsymbol{d}}_3}{1 + \hat{\boldsymbol{d}}_3}} \tag{3.6}$$

$$r = \|\boldsymbol{d}\|. \tag{3.7}$$

The rotation for data normalization is produced by combining a rotation about the Z and Y axes with angular components θ, ϕ respectively as

$${}^{B}\mathbf{R}_{L} = \boldsymbol{Z}(\theta)\,\boldsymbol{Y}(\phi)\,, \tag{3.8}$$

where $\boldsymbol{Z}$ and $\boldsymbol{Y}$ indicate relative rotations about the Z and Y axes. To achieve a rotation between the calibration world frame (0) to the local frame (L), rotations are chained as

$$\tilde{\mathbf{R}} = {}^{L}\mathbf{R}_{0} = {}^{B}\mathbf{R}_{L}^{\top}\,{}^{B}\mathbf{R}_{0}, \tag{3.9}$$

where $\tilde{\mathbf{R}}$ is used as a compact expression for the rotation between any associated point and the original world frame.

3.3.2.2 Point Bundles

We measure robot pose by collecting sets of 3 DoF point measurements from Spherically Mounted Retroreflectors (SMR) laser tracker targets with a know relationship to an end effector frame of interest. For ease of storage and manipulation, each set is stored as "point bundles" in this work, with a series of N points concatenated into a $[3N \times 1]$ array as

$$\mathcal{P} = \begin{bmatrix} \mathbf{d}_1 \\ \vdots \\ \mathbf{d}_N \end{bmatrix}. \tag{3.10}$$

The nominal configuration of the point bundle is recorded in the end effector frame and is used in calibration and analysis operations. Examples of typical point bundle configurations are world frame monuments statically mounted in a working environment and measurement locations mounted on the end effector of a robotic manipulator.

3.3.3 Frame Generation and Covariance

A best-fit transform between a nominal point bundle and one measured at a particular manipulator pose is used to create 6 DoF poses for use in calibration [113]. A RANSAC algorithm [119] is used to fit in cases where duplicate or missing points are present in a point bundle.

If individual 3D measurement covariances for each point bundle measurement are known, a composite 6D covariance matrix can be calculated to define the full pose uncertainty of this resulting transform [117].

3.3.3.1 Point Bundle Residuals

Point-errors are calculated for the point bundle as the difference between measured and calculated positions as

$$\mathbf{e}_p = \mathcal{P}_{\text{meas}} - \mathcal{P}_{\text{calc}} = \begin{bmatrix} e_1 \\ \vdots \\ e_N \end{bmatrix}, \tag{3.11}$$

where $\mathbf{e}_p$ is a $[3N \times 1]$ vector and individual error vectors e_n are $[3 \times 1]$.

The construction of a direct-drive metrology instrument produces directional measurement uncertainties based on the orientation of the head relative to the point being measured. For a series of non-coincident point measurements such as those present in this work, the changing rotation prevents direct comparison of point residuals as shown in Figure 3.3. To permit residual fitting and analysis in the

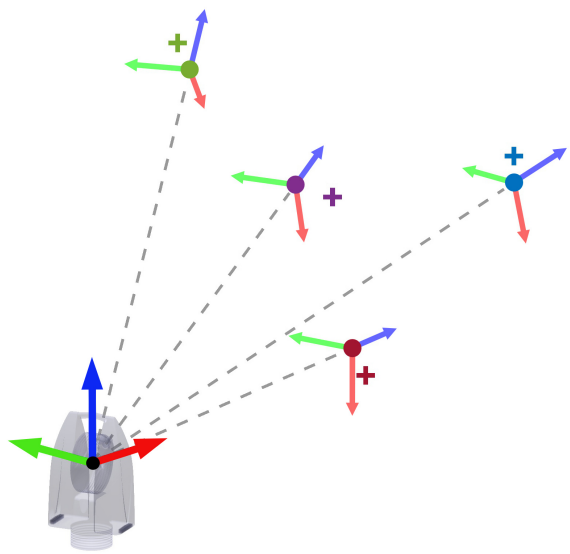

Figure 3.3 Representation of the measurement frames in which point measurement error is evaluated to fit uncertainty model. Solid dots indicate the point positions calculated with the fitted kinematic model, while the crosses indicate the associate real measurement collected. Each residual is individually evaluated in the projected measurement frame projected from the metrology system.

local measurement frame, each residual is rotated as

$$\tilde{\mathbf{e}}_p = \begin{bmatrix} \tilde{\mathbf{R}}_1 & & 0 \\ & \ddots & \\ 0 & & \tilde{\mathbf{R}}_N \end{bmatrix} \mathbf{e}_p. \tag{3.12}$$

Point residuals are vertically concatenated for use in the EM fitting process. The residuals for a series of M bundle measurements is represented as

$$\mathbf{E}_{\mathcal{P}} = \begin{bmatrix} \mathbf{e}_{p,1} \\ \vdots \\ \mathbf{e}_{p,M} \end{bmatrix}. \tag{3.13}$$

3.3.4 Expectation-Maximization Algorithm

This error is calculated of concatenated calculated using robot forward kinematics and

3.3.4.1 Expectation - Uncertainty-Weighted Kinematic Calibration

Weighted kinematic calibration can be described with the general minimization problem

$$\arg\min_{\phi} \|\mathbf{W}(\boldsymbol{\gamma}, \boldsymbol{\alpha})\, \mathbf{E}(\boldsymbol{\theta}, \boldsymbol{\phi}, \mathcal{P})\|^2, \tag{3.14}$$

where $\mathbf{W}$ is a weighting matrix covariance model parameterized with inputs $\boldsymbol{alpha}, \boldsymbol{gamma}$, and $\mathbf{E}$ is the concatenated point-bundle error for all measured poses used in the calibration (3.13) with inputs of robot

joint values $\boldsymbol{\theta}$, point bundle measurements $\mathcal{P}$, and manipulator kinematic parameters $\boldsymbol{\phi}$. The EM fitting process is initialized with estimates for the robot kinematic parameters ($\boldsymbol{\phi}$), but not covariance model parameters (α, γ). Each fitting epoch begins with a kinematic calibration, or the Expectation step, using Weighted-Least-Squares fitting. For a set of measurements M, we construct this problem as

$$\Delta\boldsymbol{\phi} = \left(\mathbf{J}_{\phi|\mathcal{P}}^{\top}\boldsymbol{W}\mathbf{J}_{\phi|\mathcal{P}}\right)^{-1}\left(\mathbf{J}_{\phi|\mathcal{P}}^{\top}\boldsymbol{W}\mathbf{E}_{\mathcal{P}}\right), \tag{3.15}$$

where weighting matrix $\boldsymbol{W}$ is initialized as identity in the first epoch and subsequently calculated in the Maximization process for all following epochs.

To map the relationship between kinematic parameters and 3D point bundle error, the 6 DoF pose-error kinematic parameter Jacobian $\mathbf{J}_{\phi}$ is converted to the vectorized 3D point bundle space by use of intermediate point-and-quaternion Jacobians previously demonstrated for covariance conversions [117]. This process uses analytical Jacobians to prevent loss of accuracy during the conversion process, and the final Jacobian is expressed as

$$\mathbf{J}_{\phi|\mathcal{P}} = \frac{\partial\mathbf{e}_p}{\partial\boldsymbol{\tau}}\left(\frac{\partial\mathbf{e}}{\partial\boldsymbol{\tau}}\right)^{\dagger}\mathbf{J}_{\phi}, \tag{3.16}$$

where $\boldsymbol{\tau}$ is the point-and-quaternion representation of the current end effector pose in world frame, $\mathbf{e}$ is 6 DoF pose-error, and $\mathbf{e}_p$ is 3 DoF point bundle error defined above.

The $\Delta\boldsymbol{\phi}$ is used to update the kinematic parameters as

$$\boldsymbol{\phi}_{i+1} = \boldsymbol{\phi}_i + \Delta\boldsymbol{\phi}, \tag{3.17}$$

where i is the current loop of the kinematic parameter fitting process. The concatenated point bundle pose error vector $\mathbf{E}_{\mathcal{P}}$ defined (3.13) is recalculated using the updated kinematic parameters, with the process repeating until convergence is achieved.

3.3.4.2 Maximization - Covariance Estimation

In the case of normally distributed measurement error and a fitted kinematic model, the residuals of the model fit are representative of manipulator pose uncertainty (3.3). We fit a parameterized covariance model to the residuals with the minimization problem

$$\underset{\gamma,\alpha}{\arg\min}\,\|\mathbf{W}\left(\boldsymbol{\gamma},\boldsymbol{\alpha}\right) - \mathbf{E}\left(\boldsymbol{\theta},\tilde{\boldsymbol{\phi}},\mathcal{P}\right)\|^2, \tag{3.18}$$

where $\tilde{\boldsymbol{\phi}}$ is the kinematic parameter estimate produced by the Expectation step. In general, these residuals are also inclusive of all un-modelled uncertainty sources, which can lead to an inflated total uncertainty compared to the accuracy of the measurement instrument itself. However, these residuals are representative of the total uncertainty within the post-calibrated robot kinematic model.

The elements of the estimated covariance kernel Σ_{est} are parameterized in an element-wise manner for each of the D measured DoF as

$$\Sigma_{\text{est}} = \begin{bmatrix} \sigma_{11} & \dots & \sigma_{1D} \\ \vdots & \ddots & \vdots \\ \sigma_{D1} & \dots & \sigma_{DD} \end{bmatrix} \tag{3.19}$$

$$\sigma_{ij} = \gamma_{ij} + \alpha_{ij}\boldsymbol{r} \tag{3.20}$$

where γ and α are the offset and range scaling parameters, respectively, and $\boldsymbol{r}$ is the distance to the measurement from laser tracker coordinate system as shown in Figure 3.2. By scaling the α terms by the magnitude of this vector, measurement effects proportionate to the range are captured. As the covariance terms are positive semi-definite, $\sigma_{D1} = \sigma 1D$, resulting on only $(D^2 + D)/2$ unique terms for fitting that are extracted as the upper or lower triangular matrix of the elements. A vectorized representation of the parameters is stored as

$$\boldsymbol{\varsigma} = \begin{bmatrix} \text{vec}\left(\boldsymbol{\gamma}\right) \\ \text{vec}\left(\boldsymbol{\alpha}\right) \end{bmatrix}, \tag{3.21}$$

with final dimensions of $\left[(D^2 + D)/2 \times 1\right]$.

Each individual point measurement across all point bundles and measurements $i \in NM$, the relationship between the covariance parameters vector $\boldsymbol{\varsigma}$ produces the linear relationship

$$\mathbf{A}_{\boldsymbol{\varsigma},i} = \begin{bmatrix} \mathbf{I} & \mathbf{I}\boldsymbol{r}_i \end{bmatrix}. \tag{3.22}$$

Point bundle residuals are calculated by transforming the nominal end effector point bundle to the 6 DoF end effector pose produced at each of the input joint configurations and taking the difference to the measured point. Each point residual is rotated to the native instrument frame (3.12) to permit the scatter matrix calculation (3.23) and subsequent parameterized fitting process. Point-wise scatter matrices are calculated from each of the resulting measurement frame point-error residuals and have unique elements vectorized in the order of (3.21) as

$$\Sigma_i = \tilde{e}_i \tilde{e}_i^\top \tag{3.23}$$

$$\mathbf{b}_i = \text{vec}\left(\Sigma_i\right). \tag{3.24}$$

Components $\mathbf{A}_i$ and $\mathbf{b}_i$ are vertically concatenated and used to produce a fit for the parameterized uncertainty model $\boldsymbol{\varsigma}$. In order to produce a model valid over the complete measurement workspace, the parameters corresponding to the variance terms of (3.19) are found using non-negative least squares fitting [120]. If covariance terms are included in the model, ordinary LS fitting is used to calculate the terms.

Due to the orthogonal construction of the metrology equipment used within this work, we only consider the measurement variance terms, reducing the dimension of $\boldsymbol{\varsigma}$ to $[6 \times 1]$. In cases where little variation exists for the values of $\boldsymbol{r}$ across the measurement data set, the covariance parameters $\boldsymbol{\gamma}, \boldsymbol{\alpha}$ may not be distinguishable from each other and provide a local uncertainty approximation valid in the workspace in which the data was collected.

After a fitted uncertainty model is obtained, the kernel is recalculated for each calculated point position (3.19) and rotated back into the original residual frame. The variances from the block diagonal matrix of the point measurement covariance estimates are extracted and normalized such that the largest value is unitary to prevent numerical issues due to the very small values typically produced by precision metrology equipment. These values are diagonalized and inverted to produce the weighting matrix $\boldsymbol{W}$ for the next epoch. The percent change between the calculated covariance parameters $\boldsymbol{s}$ for the current and previous epoch are calculated and serve as the primary exit condition for the EM fitting process. Once this difference falls below a specified convergence tolerance, e.g. 0.01%, the process is completed.

3.4 Studies

3.4.1 System Configuration

3.4.1.1 Robotic Manipulator

A high precision 7 DoF hybrid robot system is used as the experimental setup for this work. Displayed in Figure 3.1, the manipulator is composed of a 6-RRRPRR Parallel Kinematic Manipulator (PKM) with offset R-R joints (H-850 6-Axis Hexapod, Physik Instrumente, Karlsruhe, Germany) [1] mounted to a rotary stage (ACR240HT-ABS, IntelLiDrives, Philadelphia, PA, USA.)[1]. The manipulator is securely affixed to a research grade optical table. Effective encoder specifications incorporating any gear ratio effects are listed for each component in Table 3.2.

Table 3.2 Robot Encoder Specification

Variable	Encoder Resolution	Variance
Rotary Stage	2,097,152 counts/rot	7.4803×10^{-13} rad^2
Prismatic Leg	40,960 counts/mm	4.9671×10^{-17} m^2

The kinematic model for this hybrid manipulator is constructed using Denavit–Hartenberg, Hayati, and Point-and-Quaternion links as described in [20, 21, 117]. To increase parameter identifiability within the kinematic model, some parameters are removed from the calibration process.

[1]Commercial products or brand names are only mentioned to clarify what was done in this work. This is not an endorsement of any particular commercial product.

3.4.1.2 Metrology Instruments and Configuration

Measurement data is collected as 3D points by a laser tracker system (Leica Absolute Tracker AT960, Leica Geosystems, Norcross, GA, USA) [2] measuring precision SMR targets (Red Ring Reflector 0.5" & Red Ring Reflector 1.5", Leica Geosystems, Norcross, GA, USA) [2] mounted to the optical table and to the robot end effector. Point measurements are collected and stored using the software package Spatial Analyzer[2], with measurements returned in the native instrument frame in spherical coordinates and then processed into Cartesian coordinates in the designated world frame. All point measurements are collected with front-back face data measurement with time of 1 s per face with points averaged to produce the composite result. The equipment manufacturer provides nominal specifications for the performance of the laser tracker in accordance with ASTM B89.4.19-2006 of ± 7.5 μm + 3 μm/m for 3D points [112].

3.4.1.3 Coordinate Systems

Two coordinate systems are configured relative to clouds of 3D points within this work. The world coordinate system for simulated and experimental measurements is created by establishing a best-fit circle of measured points collected during rotary stage motion. The transform is configured to be coincident to the center point of the circle, with the normal of the planar fit used as the Z axis and the X axis configured to be aligned with the optical table used to mount the manipulator. This frame is referenced to a series of five SMR monuments statically mounted to the optical table.

The end effector frame of interest on the manipulator is defined to be coincident to a 6D laser tracker measurement system (TMC30-F, Leica Geosystems, Norcross, GA, USA)[2] with integrated SMR mount locations with manufacturer-specified locations. At the manipulator home position, the frame produced by a measurement of this system is referenced to four integrated SMR locations and one external reflector securely mounted to the end effector of the robot using optical components.

The nominal positions of the world coordinate system and the end effector coordinate system with SMR locations are displayed in Figure 3.1. During measurements, each frame is reconstructed from a series of point measurements using the best-fit transform between the nominal point groups and the corresponding measurements [113]. Individual 3D point measurement covariance matrices can be used to create a composite 6D covariance matrix describing the uncertainty of the transformed frame [117].

3.4.1.4 Target Poses

We create a shared set of target poses for both a simulated and experimental study. For this we generate a set of 200 random feasible configurations of the hybrid manipulator from which subsets will be

[2]Commercial products or brand names are only mentioned to clarify what was done in this work. This is not an endorsement of any particular commercial product.

used for calibration and validation. The validation data set used in the simulation is constructed as a set of 200 random feasible configurations from the PKM. For each of the configurations in the calibration and validation data set, the serial rotator position is solved to align the SMR targets mounted on the hybrid manipulator with the laser tracker to minimize orientation adjustments.

3.4.2 Simulated Study

To validate the algorithm and experimental design, a simulated test case of the EM fitting algorithm is implemented.

3.4.2.1 Uncertainties

Measurement uncertainty is modelled as (3.19) and (3.20), with baseline distribution arbitrarily defined with strictly variance terms for both $\boldsymbol{\alpha}$ and $\boldsymbol{\gamma}$ listed in Table 3.3. These parameters are arbitrarily chosen distinct values to assist in result interpretation, but are scaled such that each component has a similar final magnitude of contribution to the total simulated point measurement uncertainty. Nominal kinematic and uncertainty model parameters are perturbed from their initial values using uniform distributions listed in Table 3.4.

Table 3.3 Simulated Study Uncertainty Parameters

Variable	**Units**	σ^2_{X}	σ^2_{Y}	σ^2_{Z}
$\boldsymbol{\gamma}_0$	m^2	1×10^{-10}	2×10^{-10}	3×10^{-10}
$\boldsymbol{\alpha}_0$	m^2/m	5×10^{-11}	6×10^{-11}	7×10^{-11}
$\boldsymbol{\gamma}_{\mathrm{f}}$	m^2	-	-	-
$\boldsymbol{\alpha}_{\mathrm{f}}$	m^2/m	1.997×10^{-10}	2.323×10^{-10}	2.921×10^{-10}

Table 3.4 Simulated Manufacturing Error Intervals.

Manipulator Type	**Position (μm)**	**Angle (°)**
Serial	± 127	± 0.5
Parallel	± 25.4	± 0.1

3.4.2.2 Fitting Results

The EM process exited after 3 epochs, with final 6 DoF RMS pose-error of 12.5 μm position, 116 μrad rotation for the 141 pose calibration data set and 14.2 μm position, 120 μrad rotation error for the 61 pose validation data set. Fitted uncertainty parameters are listed in Table 3.3. The effects of the static variance $\boldsymbol{\gamma}$ and the range-dependent variance $\boldsymbol{\alpha}$ were captured by only the range-dependent variable in the fitting results due to the small range in $\boldsymbol{r}$ values (2.463 m to 2.680 m) produced during the motion of this

manipulator, but does not significantly impact the accuracy of the final variance evaluation throughout the calibrated workspace.

3.4.3 Experimental Study

3.4.3.1 Data Collection & Analysis

We extend our methods to the physical robot configuration after simulation. The physical system is moved to each of the 200 previously generated poses of the target data sets. In addition to the SMR targets located on the end effector of the manipulator, the monument locations used to establish the location of the world frame are remeasured before each pose. After reaching the target pose, SMR orientation is checked to ensure visibility by the laser tracker system and individual SMR targets are reoriented to be visible to the laser tracker. A conservative settling time of 10 s was introduced between robot motion completion and data collection initialization to prevent transient dynamic motion from being captured in the point measurements.

Point data was captured for each of the SMR targets using the AT960 laser tracker with a 1 s duration. Laser tracker orientation and point data collection was controlled programatically to reduce operational interaction and error. Acquisition failures occurred when the laser tracker was unable to establish a lock on a SMR target or retained a lock on a prior target resulting in a point measurement failure. All point bundles containing an acquisition failure contain sufficient information to produce a valid best-fit frame, with the frequency of the data acquisition failures is reported on a point-wise and pooled basis in Table 3.5.

Table 3.5 Measurement Acquisition Failures

World Frame						
Label:	T4	R1	R2	R4	T2	Impacted $\mathcal{P}$
# Meas.:	10	5	4	1	5	23
End Effector						
Label:	pt1	pt2	pt3	pt4	P5	Impacted $\mathcal{P}$
# Meas.:	3	2	3	2	3	13

End effector point bundle data is processed into best-fit frames [113]. Evaluation of the residuals from the fitting process reveals normal distributions with little covariance, corresponding with the expected distributions.

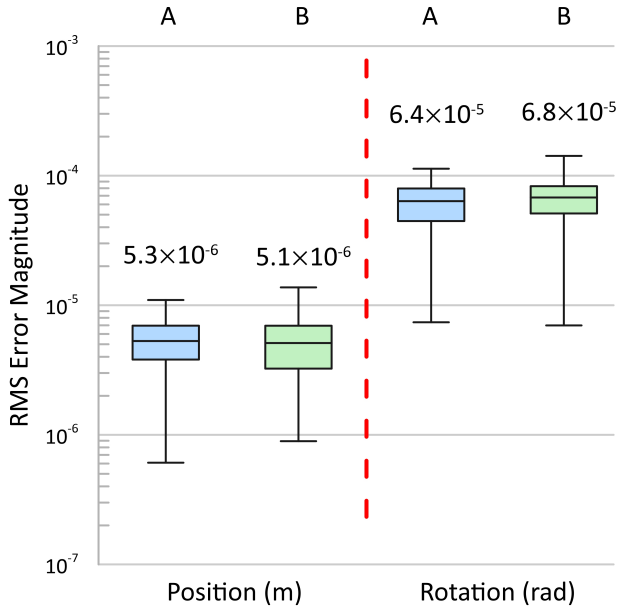

Figure 3.4 RMS pose-error distributions for experimental kinematic calibration study calculated from best-fit 6 DoF frames generated from measured point bundles. The calibration data set of 141 points (blue, **A**) and validation data set of 61 points (green, **B**) have similar means and distributions. Median values are listed above each distribution, and a log axis scale is used to present the different magnitudes of data presented.

3.4.3.2 Fitting Results

The calibration process utilized a randomly selected subset of 141 of the measured poses and exited after 4 epochs, with final 6 DoF RMS pose-error of 6.0 μm position, 66.6 $\mu\, rad$ rotation for the calibration data set and 6.4 μm position, 70.8 μrad rotation error for the validation data set. Fitted uncertainty parameters are listed in Table 3.6. The final error distributions for both calibration and validation data sets are displayed in Figure 3.4. All variance is fitted to the range-dependent variable $\boldsymbol{\alpha}$, similarly to the simulation case which shares a low total range of motion.

Table 3.6 Experimental Study Fitted Uncertainty Parameters

Variable	**Units**	σ_{X}^2	σ_{Y}^2	σ_{Z}^2
$\boldsymbol{\gamma}$	m^2	-	-	-
$\boldsymbol{\alpha}$	m^2/m	2.779×10^{-11}	3.384×10^{-11}	3.484×10^{-11}

Hypothesis testing is conducted to compare the point bundle fitting residuals produced with the calibration and validation data sets to verify that the fitted variance parameters can be applied across the calibrated workspace. Each dimension of the residual terms (X,Y,Z) were compared using the two-sample Anderson-Darling test [121], with no statistically significant differences found at $p = 0.05$. The distribution

for both data sets across all dimensions are displayed in Figure 3.5.

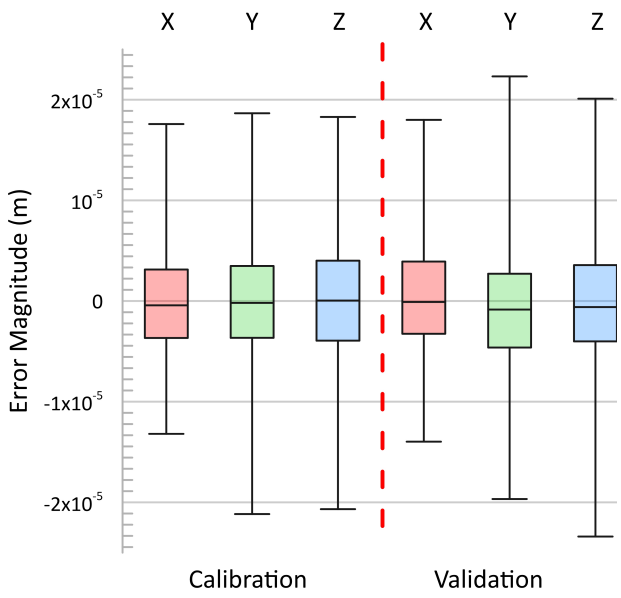

Figure 3.5 Grouped point measurement residuals from experimental study reported in measurement frames and normalized by dividing by point-wise measurement distance to allow direct comparison to fitted α variance.

3.5 Discussion

The results of the experimental study demonstrate that the residual-based parameterized uncertainty model can be used to accurately estimate the post-calibration uncertainty within our work volume, and provide good agreement with manufacturer measurement uncertainty specifications. Although the limited motion range of the robot manipulator prevents static uncertainty sources from being distinguishable from the range-dependent sources in our test cases, the use of non-negative least squares fitting provides a robust method for creating an appropriate local model of measurement uncertainty that can be applied throughout the calibrated workspace. In larger manipulator configurations, such as those incorporating industrial serial manipulators, such static components may become observable. As the additional work volume also accentuates many of sources of uncertainty un-modelled in this work that contribute to the overall fitted covariance magnitude, particularly lever arm effects, environmental stability for metrology measurements, and backlash conditions. Pose data from such systems can help characterize the magnitude of each of these contributions in a typical environment and present areas in which the simplified uncertainty model can be expanded to provide additional accuracy and insights over the complete workspace.

Future work can implement the parameterized variance model to quickly and accurately calculate uncertainty metrics for 3 DoF point bundles and 6 DoF fitted frames within the calibrated workspace to

facilitate the selection of robot configurations and poses that minimize total pose uncertainty. For example, the position of the metrology instrument used to collect measurement pose information can be adjusted to provide better post-calibration certainty of final pose, or motion of a robot manipulator can be constrained to remain in an area of low uncertainty during a process that requires high accuracy. Regardless of the application, the fitted uncertainty model provides a powerful tool for known pose uncertainty that can be virtually evaluated with low computational cost throughout a robot workspace.

3.6 Conclusion

We demonstrate an Expectation-Maximization approach to simultaneously fit an instrument-based measurement uncertainty model during uncertainty-weighted non-linear least-squared kinematic calibration. We detail the implementation of this algorithm for a direct-drive laser tracker system without a loss of general applicability to other metrology instrument uncertainty models. To facilitate the measurement uncertainty fitting on this system, we implement a method to move from the standard 6 DoF pose-error calibration space to 3 DoF point bundle. Our studies show that the EM algorithm can retrieve fitted measurement uncertainty estimates that provide strong agreement with manufacturer specifications only from calibration fitting residuals, providing a novel approach for validating specified performance or estimating the performance where specifications are not present. This removes the requirement for pre-existing uncertainty estimates previously found in WLS fitting approaches in kinematic calibration and provides an avenue for expanded uncertainty-aware planning for robot manipulators.

CHAPTER 4

ROBOTIC ANTENNA RANGE SCAN GENERATION WITH HIERARCHICAL OBJECTIVE MINIMIZATION AND MEASUREMENT ORDER OPTIMIZATION

A paper in preparation for the IEEE Transactions on Antennas and Propagation.

Benjamin L. Moser [7], Joshua A. Gordon [8] and Andrew J. Petruska [9]

4.1 Abstract

Robotic antenna range performance over canonical scans is enhanced through the use of a hierarchical inverse kinematics pipeline including travelling salesman problem pose ordering. The performance of this robot-focused positioning approach is compared to existing approaches in a series of simulated studies based on the state-of-the-art NIST LAPS system. Secondary objectives relevant to the open loop operation of the system were implemented, with an average reduction of 34.6% for joint excursion metrics found when performing canonical extrapolation, planar, and spherical test cases with an small average decrease of scanning motion 1.8% time. An average increase of the lower priority measurement uncertainty objective of 15.7% was found. Significant expansions of scan geometries over system integrator specifications were also successfully tested, increasing the maximum extrapolation size from $6\,m$ to $9\,m$, maximum planar scan size from $3\,m \times 3\,m$ to $8\,m \times 8\,m$, and maximum spherical scan radius from $1\,m$ to $4\,m$. Implementation of these inverse kinematic techniques can dramatically improve the scanning capabilities of current and future robotic antenna range installations.

4.2 Introduction

Robotic positioning systems have recently been embraced for state-of-the-art antenna metrology scanning facilities due to the flexibility and cost relative to traditional positioning systems. Robotic metrology systems are typically overactuated to permit compatibility with a broad range of antenna geometries, with research and commercial configurations with 7 Degree of Freedom (DoF) [14], 8 DoF [8, 122], and 13 DoF [4, 12, 13]. Despite the commonality of higher DoF robotic positioning systems, current scan approaches mimic the motions of low DoF, specialized scanning systems such as

[7] PhD Candidate in Mechanical Engineering at Colorado School of Mines in Golden, CO. Primary author responsible for study conceptualization, system hardware/software design, experimental design, overseeing and conducting data collections, analyses, results interpretation, and manuscript preparation.

[8] Group Leader for the Electromagnetic Fields Group at the National Institute of Standards and Technology in Boulder, CO. Responsible for project administration, system hardware acquisition, and manuscript revisions

[9] Associate Professor and Director of M^{3}Robotics Laboratory in Mechanical Engineering at Colorado School of Mines in Golden, CO. Advisor to primary author. Responsible for project administration, study conceptualization, results interpretation, and manuscript revision.

roll-over-azimuth positioners for pose selection. While advantageous for the purposes of visual recognition of scan behavior, only subset of the available motion is used, resulting in joints being used for static or near-static positioning roles during the scan. We describe and implement an inverse kinematics pipeline for use in antenna metrology tasks that more fully utilizes the positioning capabilities of the constituent robotic manipulators to provide additional flexibility, faster scanning speed, and improved operation when considering secondary objectives.

We focus on reproducing canonical antenna scans in this work, encompassing extrapolation, planar, and spherical test cases. Descriptions of typical measurement devices, spacings, and configurations are standardized and readily available [9], with traditional positioning systems only capable of performing one scan type with a single non-trivial configuration present at each desired pose. Common scan approaches are ordered in a human-oriented manner, with positioners performing a sweep in one coordinate direction while indexing a second coordinate, and the traditional positioning systems are designed around this motion. Robotic manipulators have recently been introduced as flexible positioning systems [4, 12], superceding the capabilities of older antenna ranges by permitting multiple scan types to be performed on a single range. Scans performed on these newer systems currently directly replicate the motion of legacy manipulators, constraining the possible solutions and artificially reducing the maximum measureable scanning surface dimensions as displayed in Figure 4.1. Non-canonical scan geometries have been proposed to expand the scanning capabilities [18], but still retain the constrained scanning behavior inherited from traditional positioning systems. Integration of robot-focused motion planning is beginning to emerge for antenna metrology applications, boosting scan efficiency through spline-based generation [123] and travelling salesman problem (TSP) ordering of a maximum determinant sampling grid [19], but continue traditional scan geometry placement and inverse kinematics (IK) solutions calculated for each individual manipulator component separately.

Robotic inverse kinematics is the process in which a joint configuration that moves the end effector to a desired pose is found, and represents a critical part of standard positioning task. Serial robotic mechanisms with up to 6 DoF often have analytical solutions which directly solve for configurations to satisfy a particular end effector pose, while non-trivial manipulators with higher DoF typically rely on numerical methods due to the presence of an infinite solution space [61, 107]. These numerical methods locally linearize the relationship between the active joints of the robot and the end effector pose and use minimization methods to find a valid configuration that satisfies the desired end effector pose. Contemporary state-of-the-art solvers use parallel runs of standard nonlinear least-squares and constrained optimization solvers, such as SQP, to achieve a higher generation success rate in complex, high DoF cases [62]. This process has been modified to use of analytical gradients for faster computation speed [63].

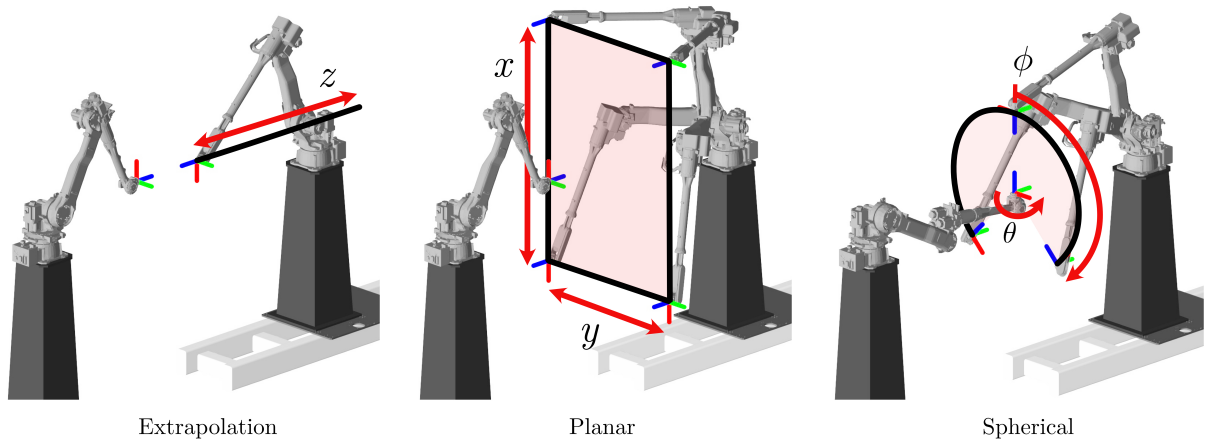

Figure 4.1 Visual representation of current scanning configurations on the LAPS system. Existing scan implementations constrain motion to reproduce positioner motion of specialized antenna manipulators along the indicated axes, using a small subset of available joints during operation. Extreme joint angles, visible on the spherical example, ultimately limit possible scan sizes in these configurations. Our inverse kinematics solution approach removes this constraint, resulting in larger possible scan sizes with lower joint excursion.

Generalized analytical Jacobians that permit parallel mechanisms to be solved in the same contextual framework as serial mechanisms are available [117], permitting these approaches to be extended to all common manipulator types found in robotic antenna metrology ranges.

Robotic antenna ranges are typically constructed from two distinct kinematic chains of industrial robotic manipulators, representing a high total DoF control case when used for relative positioning tasks. When referenced to a single world frame, these robots are currently controlled as distinct components, using the solution from one to constrain the solution from another [4, 124]. By splitting the problem, the task complexity is reduced, which permits the use of manufacturer-provided IK solutions native to each robot controller. Although less convenient from an IK calculation perspective, the larger solution space offered by considering the robotic kinematic chains as a holistic unit provides opportunities for the optimization of secondary tasks useful for antenna metrology. Techniques for the implementation of additional objectives have been explored in the context of humanoid robotics with very high DoF, with focus on center-of-mass management, gaze control, and gait factors [68, 70, 72], and are typically implemented using hierarchical task frameworks to ensure that objectives of lower priority are minimized without interfering with preceding objectives.

The dual-arm geometry found on humanoid robots is very similar to the kinematic chains used in robotic antenna ranges, with prior work similarly viewing the kinematic chains as a holistic unit for the purposes of self-touch calibration [125]. The use of this approach requires the implementation and

conversion of all used parameterizations, limiting its applicability to the broad range of manipulators found in the robotic antenna ranges. To remove this limitation, we formulate a generalized approach for representing a system composed of two robotic kinematic chains as a single kinematic chain with applicability to relative IK solutions and calibration such as those found in antenna scanning tasks. The access to the complete, high DoF joint solution space of the dual robot system permits the use of hierarchical task frameworks for antenna scan generation.

Such hierarchical inverse kinematics have several common variations, including pure equality objectives [65–67], a primary inequality objective [72], and a complete cascade of inequality objectives[69]. Each of these approaches have varying computational demands, which limit real-time planning applications commonly found in adaptive humanoid or mobile robot control, although efficient active set solvers have been developed to facilitate faster computation [70]. Recent work has developed IK methods to apply similar secondary constraints with respect to path continuity and singularity avoidance to non-over-actuated mechanisms using objective weighting [126]. As the inverse kinematics for antenna metrology are pre-computed for utilization in a static environment without strict timing constraints, we rely on a standard QP cascade methods outlined in [69].

Solutions for each desired pose are calculated in canonical order, but the IK solutions incorporating secondary objectives may result in large, inefficient motions between adjacent canonical poses. To reduce repetitive joint motions, the need for secondary backlash correction moves during operation, and total scan time we propose the use of the travelling salesman problem (TSP) to determine pose ordering. Many approaches for solving this NP hard problem have been formulated and compared [127], with modern heuristic methods permitting the fast and accurate solutions necessary for large data sets similar to those generated for antenna scanning purposes. We utilize an implementation of the state-of-the-art Lin-Kerrigan-Helsguan heuristic solver within this work [128–130].

This paper is structured as follow. We first present methods to view robotic positioning systems composed of two kinematic chains as a single kinematic chains for combined inverse kinematic solving. We then formulate and solve the inverse kinematics to perform canonical scanning tasks with hierarchical optimization to optimize for a selection of secondary objectives identified as impactful to contemporary antenna scanning. Finally, we implement an inter-pose motion weighting scheme with regard to joint motion timing inclusive of backlash correction motion of joints that are not gravity loaded as the input for the asymmetrical travelling salesman problem (ATSP). The performance of our implemented antenna scan generation pipeline is quantified and compared to existing state-of-the-art implementations in a simulated 13 DoF robotic antenna system. Notation used in this work is summarized in Table 4.1.

The primary contribution of this work is a demonstration of the feasibility and applicability of hierarchical inverse kinematics for general antenna metrology purposes. Our technical contribution is the formulation of methods to holistically solve the inverse kinematics of two distinct kinematic chains operating as a single unit, the integration of parametric uncertainty models to generate uncertainty-aware positioning, and the weight generation scheme for implementation with existing ATSP solvers. Our studies show that our approach provides benefits for antenna metrology ranges with robotic positioners by effectively utilizing the redundant DoF to perform secondary tasks and improve antenna scan speed by efficient pose ordering.

Table 4.1 Notation summary. Matrix size is displayed in brackets before description and subscripts provide contextual definitions.

Symbol	Description
$\mathbf{R}$	[3×3] Rotation matrix
$\mathbf{d}$	[3×1] Cartesian displacement vector
$\mathbf{T}$	[4×4] Homogeneous transformation matrix
$\boldsymbol{\tau}$	[7×1] Position and Quaternion transform
$\mathbf{L}$	Vector of links
$\mathbf{e}$	Error vector
$\mathbf{J}$	Jacobian matrix
$\mathcal{C}$	Objective Jacobian
ϕ	Vector of kinematic parameters
θ	Vector of actuator inputs
v	Subscript denoting velocity Jacobian

4.3 Methods

4.3.1 Dual Manipulator Relative Jacobian

The LAPS robot antenna positioning system is composed of two industrial serial manipulators and an actuated linear rail for a total of 13 DoF. Typical inverse kinematic solution approaches consider each manipulator as an individual unit, satisfying end effector pose constraints on a 6 DoF and 7 DoF solution space. To project secondary objectives onto the manipulator for relative positioning tasks such as antenna scan geometries, this process overconstrains the IK solution space, reducing the available null space from 7 DoF to only 1 DoF. As such, it is advantageous to represent the holistic manipulator as a single serial chain, allowing Jacobian generation and subsequent IK operations to be performed in a single solution space. Limited prior work exists for this operation, with similar techniques accomplished by link substitution with an inverted notation. Inverted notations must be developed for each parameterization and conversions between standard and inverted links add secondary overhead to the solution process. To permit the use of the mature standard parameterizations throughout the entirety of our planning space, we instead introduce a simple transformation procedure to permit holistic Jacobian generation.

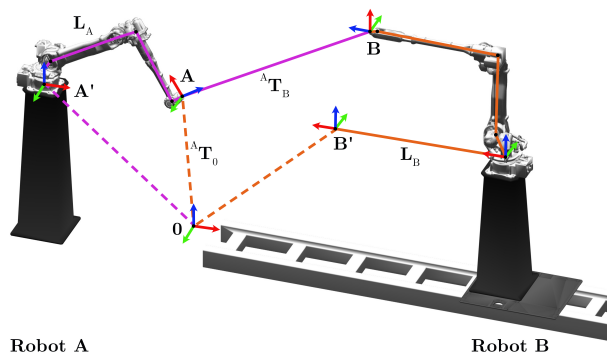

Figure 4.2 Holistic Jacobian generation for two individual manipulators is accomplished by introducing static offsets and relative rotations without the use of an inverted link notation. Relative transforms can be efficiently calculated using this technique, with secondary objectives introduced by using the larger null space present with holistic control.

Provided two robot manipulators represented as a series of links positioned relative to the world frame, ${}^{0}\mathbf{L}_{\mathrm{A}}$ and ${}^{0}\mathbf{L}_{\mathrm{B}}$, we find the relative transforms between the end effector of Robot A and the world frame (${}^{A}\mathbf{T}_{0}$) and between the end effector of Robot A and Robot B (${}^{A}\mathbf{T}_{B}$). We convert these transforms into point and quaternion offset link notation and append them to the existing link arrays as shown in Figure 4.2. Velocity Jacobians are then calculated in the world frame for each manipulator as

$$\tilde{\mathbf{J}}_{v,A} = \mathbf{J}_v\left(\left[{}^{0}\mathbf{L}_A\, {}^{A}\tau_B\right], \theta_A\right) \tag{4.1}$$

$$\tilde{\mathbf{J}}_{v,B} = \mathbf{J}_v\left(\left[{}^{A}\tau_0\, {}^{0}\mathbf{L}_B\right], \theta_B\right). \tag{4.2}$$

The holistic velocity Jacobian describing relative motion between frame A and B is formed by concatenating the Jacobian components and rotating into the desired frame as

$$\mathbf{J}_{v,A\to B} = \left[-{}^{A}\mathbf{R}_B\tilde{\mathbf{J}}_{v,A}\ \ \tilde{\mathbf{J}}_{v,B}\right]. \tag{4.3}$$

Although useful for our IK calculation purposes, the relative Jacobian formulation should not be used for dynamic calculation purposes without additional considerations due to the adjusted frame of reference it uses. The use of non-inverted notation permits dynamics-related algorithms and objectives to be integrated using the individual, non-relative Jacobians for each of the constituent manipulator chains.

4.3.2 Hierarchical Inverse Kinematics Implementation

Robot inverse kinematics are solved using hierarchical task formulation to optimize for secondary objectives during an antenna metrology scanning task. Also referred to as a task priority strategy, this is achieved by projecting the task into the null space of all preceding tasks to permit minimization without

interfering with higher priority tasks. This process can be represented as a general minimization problem as

$$\begin{aligned} \underset{\theta_k}{\arg\min} \quad & \|\mathbf{e}_k(\boldsymbol{\theta}_k)\|^2 \\ \text{subject to} \quad & \|\bar{\mathbf{e}}_{k-1}(\theta_k)\|^2 \leq \|\bar{\mathbf{e}}_{k-1}(\theta_{k-1})\|^2, \end{aligned} \tag{4.4}$$

where task error functions $\mathbf{e}$ have priority represented with subscript k and $\bar{\mathbf{e}}$ represents the concatenated evaluations of all higher priority task error functions. The highest priority task is always evaluated at zero error by hypothesis.

We adapt the general form outlined in [67] to iteratively solve inverse kinematics in manipulator joint space θ as

$$\Delta\theta_i = \Delta\theta_{i-1} + \mathcal{N}(\mathbf{J}_{i-1})\,\mathbf{J}_i\mathcal{N}(\mathbf{J}_{i-1})^{\dagger}(\mathbf{e}_i - \mathbf{J}_i\Delta\theta_{i-1}), \tag{4.5}$$

where $\Delta\theta$ is the current joint configuration step. Steps can be iteratively calculated using this approach with general minimization solvers as

$$w_i = \underset{w_i}{\arg\min}\,\|\mathbf{J}_i\mathcal{N}(\mathbf{J}_{i-1})\,w_i + \mathbf{J}_i\Delta\theta_{i-1} - \mathbf{e}_i\|^2, \tag{4.6}$$

where w_i is a vector in the constrained null space created from all higher priority tasks. This vector is re-projected into joint configuration space as

$$\Delta\theta_i = \mathcal{N}(\mathbf{J}_{i-1})\,w_i + \Delta\theta_{i-1}. \tag{4.7}$$

Within this work, we use the MATLAB `fmincon` function with the implemented SQP solver [131]. As the robotic manipulators are highly nonlinear systems, joint configuration space solutions must be recalculated throughout motion, as the linearizations input into the solver do not remain valid over the entire motion. In both solver cases, joint angle vector θ is incremented by scaling the normalized length of the final vector $\Delta\theta$ to meet an arbitrarily small step size. This is done to prevent large motions that would exceed the region of valid linearization of the joint kinematics described by the Jacobians.

4.3.3 Hierarchical Objectives

A series of objectives useful for antenna metrology purposes are implemented within this work, and outlined in the order of priority during the solution process within subsequent studies.

4.3.3.1 Pose Error Objective and Joint Limit Constraint

The primary objective of the antenna metrology inverse kinematics is to reproduce the desired transform between the Antenna Under Test (AUT) and the measurement probe to satisfy the canonical scanning pattern transforms. For this purpose, we use the velocity Jacobian calculated as (4.3) in the

solver frameworks outlined in (4.5) and (4.6).

We consider the joint limit bounds as constraints when using a general minimization solver, saturating joint velocities to a permissible band equivalent to the remaining joint travel from the current position in the pose error task as

$$D\Delta\theta_i \leq f \tag{4.8}$$

where θ is the starting joint configuration and

$$D = \begin{bmatrix} \mathbf{I} \\ -\mathbf{I} \end{bmatrix}, f = \begin{bmatrix} \theta_{\max} - \theta_0 \\ -\theta_{\min} + \theta_0 \end{bmatrix}. \tag{4.9}$$

The constraint is projected into the null space of subsequent objectives as

$$D_i = D\mathcal{N}\left(\mathbf{J}_{i-1}\right) \tag{4.10}$$
$$f_i = f - D\Delta\theta_{i-1} \tag{4.11}$$

.

4.3.3.2 Joint Excursion Objective

Joint motion from a specified starting configuration is minimized as a scalar value with error term and Jacobian described as

$$\mathbf{e}_{\text{excursion}} = 0.5\left(\theta_{0,i} - \theta_i\right)^2 \tag{4.12}$$
$$\mathcal{C}_{\text{excursion}} = \lambda_i \theta_i \tag{4.13}$$

where active joint components are represented in units of m and rad are treated equivalently. To minimize a percentage of total joint motion, weighting parameter λ should be set as the inverse of the total controllable joint width $(\theta_{\max} - \theta_{\min})^{-1}$.

4.3.3.3 Metrology Measurement Uncertainty Objective

Uncertainty for common metrology instruments can be parametrically modelled. Within this work, we focus on minimizing the measurement uncertainty of the direct-drive laser tracker for closed-loop position control found in high-frequency robotic antenna ranges. As this uncertainty is range-dependent, the uncertainty minimization problem takes the form of a measurement distance minimization between the location of the laser tracker and the measurement target. In cases with a single reflector element is present, such as 6 DoF targets (Leica TMAC) [10], this problem is formulated as

[10] Commercial products or brand names are only mentioned to clarify what was done in this work. This is not an endorsement of any particular commercial product.

$$\mathbf{e}_{\text{meas}} = \begin{bmatrix} \|\mathbf{d}_{\text{A}}\| \\ \|\mathbf{d}_{\text{B}}\| \end{bmatrix} \tag{4.14}$$

$$\mathcal{C}_{\text{meas}} = \begin{bmatrix} \mathbf{J}_{\text{meas,A}} & \mathbf{0} \\ \mathbf{0} & \mathbf{J}_{\text{meas,B}} \end{bmatrix}, \tag{4.15}$$

where distance Jacobians are calculated for each individual manipulator as

$$\mathbf{J}_{\text{meas}} = \frac{\mathbf{d}^\top}{\|\mathbf{d}\|} \frac{\partial \mathbf{d}}{\partial \boldsymbol{\theta}} \tag{4.16}$$

where $\mathbf{d}$ is the distance vector between the metrology instrument and the robot end effector denoted with the subscript and $\|\mathbf{d}\|$ is the scalar value of the respective distance vector. The elements $\frac{\partial \mathbf{p}}{\partial \boldsymbol{\theta}}$ are position pose-error rows extracted from the velocity Jacobian $\mathbf{J}_v$ calculated for the individual kinematic chain of the robot denoted by the subscript.

4.3.4 Asymmetrical Travelling Salesman Problem Ordering

Run time for the generated IK poses is optimized through the use of ordering using the LKH-3 library [128–130]. Due to the presence of backlash during motion in the robots, we construct a weighting model that leverages Asymmetric TSP methods as a backlash minimization and mitigation approach. The LKH heuristic presents significant performance increases over analytical approaches without significant sacrifice of final accuracy, and effectively processes typical antenna scan geometries of 1,000 to 10,000 poses.

4.3.4.1 Weight Generation

An asymmetrical weighting matrix for TSP ordering is created by simulating the motion time between two joint configurations using a trapezoidal joint velocity profile, yielding a per-joint motion time of

$$t_{\text{motion}} = \frac{\dot{\theta}}{\ddot{\theta}} + \frac{|\theta_j - \theta_i|}{\dot{\theta}}, \tag{4.17}$$

where i is the initial joint location and j is the joint destination. In cases where backlash on specified joint exist, backlash compensation moves are inserted by first moving to perturbed position $\theta_j + \delta$ to remove the influence of backlash on positioning before moving to the specified pose θ_j. By evaluating each joint motion for n of N inputs, we construct the TSP weighting matrix as

$$W_{i,j} = \max\left(t_{\text{motion},n} + k_n t_{\text{backlash},n}\right), \tag{4.18}$$

where boolean term k_n controls whether backlash is considered for a joint. The presence of backlash compensation moves produces asymmetrical weights for a set of joint motions that create minimum weighting conditions when few joints require backlash correction. This results in cases where segments

continuous motion without backlash are selected for, minimizing the total number of corrective moves required.

As the multi-robot antenna positioning system operates in a shared workspace, the possibility of collision between robots during repositioning exists. The likelihood of collision is minimized due to the workspace of the chamber being empty to retain anechoic performance during measurements, with the TSP ordering providing additional safety by enforcing minimal interpose motion. Motion is validated to be collision free during simulation before being implemented on the robots, with unexpected collision avoidance handled by the manufacturer-implemented Functional Safety Unit. Joint motion is accomplished using strict joint angle interpolation with a trapezoidal velocity profile.

4.3.5 Command Streaming

The final set of poses generated during the inverse kinematics process is stored as an ordered list of joint encoder counts and streamed to the robot controller to avoid local job file storage constraints. The MotoCom SDK is integrated with a master LabView control framework to sequentially send joint poses generated by the IK pipeline and trigger VNA data collection. VNA measurements can be reordered for processing with commercially available near-field processing software.

4.4 Studies

4.4.1 System Configuration

The principle robotic positioning system analyzed in this work is modelled after the Large Antenna Positioning System (LAPS) at NIST Boulder [12]. The system is composed of two robotic manipulators: A Motoman MH50-35 6 DoF arm, and a Motoman MH50-20 6 DoF arm mounted on a $7\,m$ linear rail. When used for relative positioning tasks such as antenna metrology, LAPS represents a 13 DoF system well-suited for the hierarchical objective framework presented in this work.

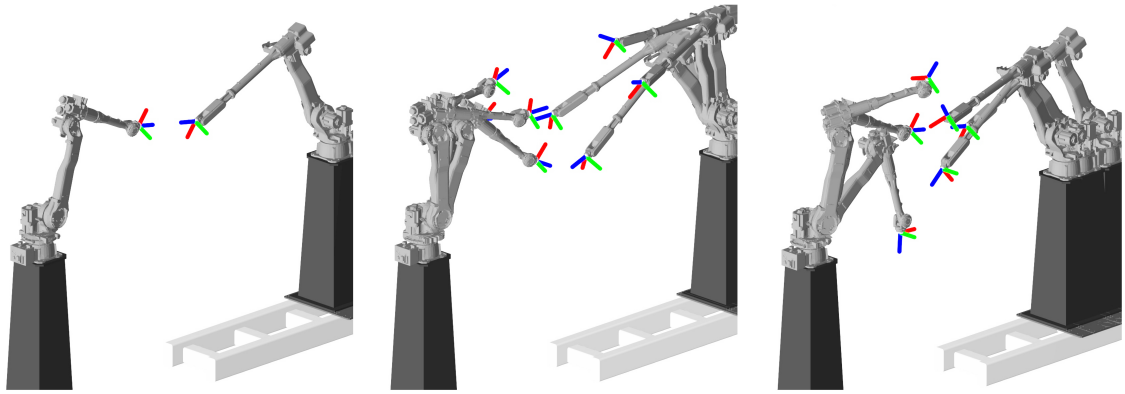

Extrapolation Planar Spherical

Figure 4.3 Visual representation of scanning configurations calculated with the hierarchical inverse kinematics framework. When compared to existing scan implementations shown in Figure 4.1, lower total joint motion is used to reach each pose. The absence of extreme joint angles permits faster motion with larger scan sizes.

4.4.2 Simulated Study

We generate quantitative comparisons of complete motion timing and secondary objective evaluations between current antenna metrology scanning techniques and our proposed scan generation framework using the simulated LAPS system with several representative scans. Current scanning techniques visualized in Figure 4.1 are representative of those implemented by the system integrator and are capable of producing extrapolation, planar, and spherical scans using subsets of the available DoF of the LAPS system.

Table 4.2 Antenna Scan Configurations

Scan Tag	**Scan Type**	**Scan Size**	**Step Size**	N_{meas}
Extrap3334	Extrap.	$z_0 = 1\,m$ $z = 5\,m$	- $1.5\,mm$	3334
Planar4096	Planar	$x = 256\,mm$ $y = 256\,mm$	$4\,mm$ $4\,mm$	4096
Sphere2044	Spherical	$r = 1\,m$ $\phi = 360°$ θ=135°	- 5° 5°	2044
ExtrapMax	Extrap.	$z_0 = 1\,m$ $z = 9\,m$	- $1\,m$	10
PlanarMax	Planar	$x = 8\,m$ $y = 8\,m$	$2\,m$ $2\,m$	25
SphereMax	Spherical	$r = 4\,m$ $\phi = 270°$ θ=180°	- 45° 90°	36

Table 4.3 Simulated Antenna Scan Results

	Poses Solved(%)		Joint Excursion (rad)			Meas. Distance (m)			Motion Time (s)			Motion Time Backlash Comp. (s)		
Scan	Standard	HOpt	Standard	HOpt	% Diff	Standard	HOpt	% Diff	Standard	HOpt	% Diff	Standard	HOpt	% Diff
Extrap3334	100	100	0.6322	0.4912	-22.3	3.2998	3.0142	-8.6	1339	873	-34.8	1339.0	1784.3	33.3
Planar4096	100	100	0.6956	0.5383	-22.6	2.5504	3.0346	19.0	1699	1701	0.1	2717.8	1893.8	-30.3
Sphere2044	100	100	1.2895	0.5298	-58.9	2.7742	3.7933	36.7	1027	873	-15.0	1655.7	1517.1	-8.4
ExtrapMax	70	100	-	0.5809	-	-	4.6987	-	-	10	-	-	12.4	-
PlanarMax	36	100	-	0.5011	-	-	3.8588	-	-	24	-	-	22.0	-
SphereMax	25	100	-	0.7631	-	-	3.7644	-	-	56	-	-	17.8	-

Each study configuration was generated as an ordered list of transforms equivalent to the canonical scan surface. For the standard scans, joints were initialized to system integrator specified locations and only specified joints were permitted to move. When solving with the hierarchical inverse kinematics framework, the general minimization formulation with joint limit constraints was implemented using the SQP solver in the MATLAB `fmincon` optimization function [131]. The LKH-3 solver was configured with 10 maximum runs, with computation time limit of 240 s per run for TSP pose ordering. Study scan configuration details are listed in Table 4.2, with max bound test cases used to illustrate the expanded positioning capabilities of the IK pipeline but not necessarily representative of the ultimate positioning limits of the system. Poses generated in this manner for the investigated scan types are displayed in Figure 4.3. The results of each simulation are reported across the three hierarchical objectives outlined in this work, motion execution times, and backlash instances in Table 4.3.

We additionally provide approximate scan geometry maxima comparisons between the approaches in Table 4.2. This list does not represent a comprehensive limit analysis, but compares the existing system integrator specified scan geometry bounds with maximum tested scan geometry bounds to illustrate flexibility gained through the use of the presented IK pipeline.

4.5 Discussion

The hierarchical objective framework functioned as expected in the trials, with reductions in joint excursion found for test cases compared to the standard configuration. The measurement distance objective, correlated with measurement uncertainty, increased in the planar and spherical test cases which required poses that could not be solved to minimize both objectives. As implemented, the lowest priority objective was only improved when it would not interfere with the higher levels, resulting in increased evaluations in cases with complex motion. The motion time cost of the more complex motion was mitigated through the use of TSP ordering, resulting in only minor increases across all scans compared to standard measurement cases. Standard scanning configurations were not capable of completing scans with larger geometries of interest, indicating the benefits of utilizing our IK pipeline. Although this is not a comprehensive test of all possible geometries or the ultimate maxima of the scans, we feel that it displays

the exceptional functionality gains made possible with our approach.

Future work involves the experimental validation of the proposed inverse kinematics pipeline when compared to existing scan implementations on the NIST robotics systems. This will permit the direct comparison between scanning results using well-characterized horns and will be compared against measured results from other National Metrology Institutes. As the placement of the joint excursion at higher priority levels dramatically reduced the ability for lower level objectives to be minimized, alternate equipment configurations that permit this task to be removed or reduced to a lower priority should be explored. Additional secondary objectives useful during antenna scanning, such as measurement system orientation and AUT/probe orientation restrictions will be developed to increase the applicability to other contemporary robotic antenna ranges. By expanding the library of secondary objective formulations, the full capabilities of the implemented hierarchical task framework can be realized.

4.6 Conclusion

We quantitatively demonstrate that improvements in secondary objectives useful to contemporary robotic antenna positioning systems can be realized through the use of a robot-focused inverse kinematics pipeline with efficient pose ordering. In simulated positioning tasks based on the state-of-the-art NIST LAPS system, an average reduction of 34.6% for joint excursion metrics was found when performing canonical extrapolation, planar, and spherical test cases with an small average decrease of scanning motion 1.8% time including backlash compensation moves. An average increase of the lower priority measurement uncertainty objective of 15.7% was found. Significant expansions of the system integrator scan geometries were also successfully tested, increasing maximum extrapolation size from $6\,m$ to $9\,m$, maximum planar scan size from $3\,m \times 3\,m$ to $8\,m \times 8\,m$, and maximum spherical scan radius from $1\,m$ to $4\,m$. Implementation of these inverse kinematic techniques can dramatically improve the scanning capabilities of current and future robotic antenna range installations.

CHAPTER 5

CONCLUSIONS & FUTURE DIRECTIONS

The goal of this Ph.D. research was to advance the state-of-the-art of robotic antenna metrology by enhancing the relative probe positioning capabilities of existing installations. This work achieves this objective by demonstrating improved positioning accuracy and flexibility on current robotic antenna range hardware with quantified position uncertainties. Specifically, we extended mature calibration techniques to general manipulator cases, modelled and validated pose uncertainty measurements, and implemented a combined hierarchical inverse kinematics pipeline with efficient pose ordering. These techniques support NIST's mission to provide traceable antenna calibration services for all sectors in the United States and promotes the adoption of robotics within the antenna metrology community.

5.0.1 Contributions

The present research investigated methods to enhance positioning performance for robotic antenna ranges through calibration, uncertainty characterization, and scan pose selection. Through experimental and simulated studies, we demonstrate the potential of these techniques to increase robotic antenna range flexibility by meeting the positioning accuracy required for higher maximum measurement frequencies and permitting the implementation of novel scan geometries on existing manipulator hardware. Specifically, key contributions of this work include:

1. Developed an approach for constrained calibration of general rigid parallel and hybrid mechanisms. By adapting mature serial robot calibration techniques with null space constraint projection, complex manipulators relevant to antenna metrology ranges can be calibrated.

2. Established methods for generating analytical Jacobians for arbitrary mechanisms for use in kinematics and calibration minimization. This improves computation speed and accuracy compared to prior implementations that rely on numerical approximation. This process can be used in a recursive manner to generate Jacobians for novel hybrid manipulators.

3. Quantified post-calibration pose measurement uncertainty based on measurement uncertainty. We implement linearized uncertainty propagation for encoder and pose measurement uncertainty components using analytical manipulator Jacobians.

4. Presented a method for fitting parameteric uncertainty models simultaneously with kinematic parameters. We use Expectation-Maximization fitting to incorporate uncertainty estimates into a

kinematic calibration. Improvements to post-calibration accuracy are found using this technique.

5. Implemented a hierarchical inverse kinematics pipeline for antenna pose generation. We develop techniques for viewing two distinct serial kinematic chains as a single high-DoF manipulator and efficiently order them using ATSP. Secondary objectives to minimize joint excursion and pose measurement uncertainty are implemented and evaluated. Visualization software is used to verify results and promote adoption.

6. Demonstrated expanded scanning geometries on existing antenna ranges. We generate poses for canonical antenna scan geometries larger than current methods support using hierarchical relative inverse kinematics. This expands supported antenna types and frequencies that can be characterized on an individual range.

7. Expanded the flexibility of antenna scanning software at NIST. We developed a unified control application for the robotic and antenna components in LabView. This application expands the flexibility of the antenna ranges to support existing and novel antenna scans by removing controller limitations present in the prior implementation. This software was used to collect measurements for the BIPM, CMC reinstatement plan for NIST 63100S antenna measurement service.

5.0.2 Future Work

There are many directions for future research to increase the impact for the antenna metrology community. The experimental configuration used to evaluate the performance of our calibration techniques, composed of a high precision hexapod and rotary stage, represents one of two kinematic chains used in the high frequency CROMMA antenna range at NIST [4]. Evaluating the impacts of extending the calibration to the complete configuration would provide valuable insights for possible operation without the use of external laser tracker feedback. Our present results indicate post-calibration positioning accuracy comparable to the uncertainty of the laser tracker can be achieved. Therefore, comparison of measured antenna patterns in cases with and without external feedback are important.

Automating methods of evaluating the offsets between the robot end effector and the aperture for the AUT and probe as mounted would boost scanning efficiency. Camera-based contactless probing has been explored in this space [57], but requires external pose feedback and positioning systems to be used. A similar configuration mounted in the antenna range could directly utilize the motion capabilities of robots to establish the offset and orientation of common antenna types. This process could eliminate the possibility of introducing alignment errors while moving the antenna fixture and seamlessly integrate with calibrated parametric models for each manipulator.

To validate the performance of our inverse kinematics pipeline, experimental scans comparing standard configurations to our proposed solutions are needed. Due to the differences in standards and requirements related to the canonical scan types simulated (Extrapolation, Planar, Spherical), such evaluations need to be conducted on an individual basis to provide additional value to the antenna metrology community.

An exciting direction of research for the inverse kinematic pipeline would be to integrate multiple antenna measurements for each pose dictated by the canonical scan to evaluate room reflections. Although robotic antenna ranges are located in anechoic chambers, absorber treatment cannot fully cover the manipulators without impeding motion. By collecting measurements of the same AUT-Probe transform at various locations in the chamber, the effects from room and robot reflections can be evaluated. This sampling approach is not possible with the standard robotic antenna range scanning configurations, but can be accomplished with our inverse kinematics pipeline.

Finally, the positioning accuracy found in current robotic antenna ranges presents difficulties for terahertz-band measurements [132]. The post-calibration RMS positioning accuracy found in this work addresses these difficulties, meeting conservative fractional wavelength positioning requirements ($\frac{\lambda}{50}$) of 6 μm at frequencies of 1 THz. This exceeds the prior testing limitations for the CROMMA system [4] and opens up the possibility of conducting sub-mmWave antenna metrology.

REFERENCES

[1] R.C. Baird, A.C. Newell, and C.F. Stubenrauch. A brief history of near-field measurements of antennas at the national bureau of standards. *IEEE Transactions on Antennas and Propagation*, 36 (6):727–733, jun 1988. doi: 10.1109/8.1173.

[2] Constantine Balanis. *Modern Antenna Handbook*. John Wiley & Sons, 2008.

[3] David R Novotny, Joshua A Gordon, Michael Shane Allman, Jeff R Guerrieri, and Alexandra E Curtin. Three antenna ranges based on articulated robotic arms at the national institute of standards and technology: Usability for over-the-air and standard near-field measurements. In *2017 IEEE Conference on Antenna Measurements & Applications (CAMA)*, pages 1–4. IEEE, 2017.

[4] J. A. Gordon, D. R. Novotny, M. H. Francis, R. C. Wittmann, M. L. Butler, A. E. Curtin, and J. R. Guerrieri. Millimeter-wave near-field measurements using coordinated robotics. *IEEE Trans. Antennas Propag.*, 63(12):5351–5362, December 2015. ISSN 0018-926X. doi: 10.1109/TAP.2015.2496110.

[5] John Hatzis, Patrick Pelland, and Greg Hindman. Implementation of a combination planar and spherical near-field antenna measurement system using an industrial 6-axis robot. In *AMTA 2016 Proceedings*. IEEE, October 2016. doi: 10.1109/amtap.2016.7806306.

[6] R. Moch, T. M. Gemmer, and D. Heberling. Spherical antenna measurements performed in a robot-based mm-wave test range. In *2021 15th European Conference on Antennas and Propagation (EuCAP)*. IEEE, March 2021. doi: 10.23919/eucap51087.2021.9411359.

[7] David Novotny, Jeffrey Guerrieri, and Joshua Gordon. Antenna alignment and positional validation of a mmwave antenna system using 6d coordinate metrology. In *2014 Proceedings of the Antenna Measurement Techniques Association*, 2014-10-13 2014. URL https://tsapps.nist.gov/publication/get_pdf.cfm?pub_id=917086.

[8] R. Moch and D. Heberling. Pointwise probe correction applied to a robot-based mm- wave antenna test range. In *2021 Antenna Measurement Techniques Association Symposium (AMTA)*, pages 1–4. IEEE, October 2021. doi: 10.23919/amta52830.2021.9620575.

[9] Constantine A. Balanis. *Antenna Theory: Analysis and Design*. Wiley John + Sons, 4 edition, April 2016. ISBN 1118642066.

[10] Nikola Petrovic, Tommy Gunnarsson, Nadine Joachimowicz, and Magnus Otterskog. Robot controlled data acquisition system for microwave imaging. In *2009 3rd European Conference on Antennas and Propagation*, pages 3356–3360, 2009.

[11] Linus Boehm, Frank Boegelsack, Martin Hitzler, and Christian Waldschmidt. An automated millimeter-wave antenna measurement setup using a robotic arm. In *2015 IEEE International Symposium on Antennas and Propagation &amp USNC/URSI National Radio Science Meeting*. IEEE, July 2015. doi: 10.1109/aps.2015.7305444.

[12] David Novotny, Josh Gordon, Michael Allman, Jeffrey Guerrieri, Alexandra Curtin, Kim Hassett, George McAdams, and Quang Ton. The multi-robot large antenna positioning system for over-the-air testing at the national institute of standards and technology1. In *Proceedings of the Antenna Measurement Techniques Association, Atlanta, GA, US*. Proceedings of the Antenna Measurement Techniques Association, Atlanta, GA, US, 2017-12-31 05:12:00 2017. URL https://tsapps.nist.gov/publication/get_pdf.cfm?pub_id=923969.

[13] D. M. Lewis, J. Bommer, G. E. Hindman, and S. F. Gregson. Traditional to modern antenna test environments: The impact of robotics and computational electromagnetic simulation on modern antenna measurements. In *2021 15th European Conference on Antennas and Propagation (EuCAP)*. IEEE, March 2021. doi: 10.23919/eucap51087.2021.9411068.

[14] Peter A. Slater, James M. Downey, Marie T. Piasecki, and Bryan L. Schoenholz. Portable laser guided robotic metrology system. In *2019 Antenna Measurement Techniques Association Symposium (AMTA)*. IEEE, October 2019. doi: 10.23919/amtap.2019.8906337.

[15] Ronald Wittmann, Bradley Alpert, and Michael Francis. Spherical near-field antenna measurements using nonideal measurement locations. In *2002 Proceedings of the Antenna Measurement Techniques Association*, 2002-11-08 00:11:00 2002.

[16] Carmen Matos, Jennifer Humanchuk, and Nima Ghalichechian. Robotically-controlled antenna measurement system for millimeter-wave applications. *Microwave and Optical Technology Letters*, 63 (5):1520–1525, December 2020. doi: 10.1002/mop.32773.

[17] R. Moch and D. Heberling. Robot-based antenna and radar measurement system at the rwth aachen university. In *2020 Antenna Measurement Techniques Association Symposium (AMTA)*, pages 1–5, 2020.

[18] Daniel Janse van Rensburg, Brett Walkenhorst, Quang Ton, and John Demas. A robotic near-field antenna test system relying on non-canonical transformation techniques. In *2019 Antenna Measurement Techniques Association Symposium (AMTA)*. IEEE, October 2019. doi: 10.23919/amtap.2019.8906358.

[19] R. Moch and D. Heberling. Maximum determinant sampling using spline-based trajectories in a robot-based mm-wave antenna test range. In *2022 Antenna Measurement Techniques Association Symposium (AMTA)*. IEEE, October 2022. doi: 10.23919/amta55213.2022.9954952.

[20] Richard S Hartenberg and Jacques Denavit. A kinematic notation for lower pair mechanisms based on matrices. *J. Appl. Mech.*, 77(2):215–221, 1955.

[21] S. Hayati, K. Tso, and G. Roston. Robot geometry calibration. In *Proc. IEEE Int. Conf. Robot. Autom.*, pages 947–951 vol.2, April 1988. doi: 10.1109/ROBOT.1988.12181.

[22] Koichiro Okamura and F.C. Park. Kinematic calibration using the product of exponentials formula. *Robotica*, 14(4):415–421, July 1996. doi: 10.1017/s0263574700019810.

[23] I-Ming Chen, Guilin Yang, Chee Tat Tan, and Song Huat Yeo. Local POE model for robot kinematic calibration. *Mech. Mach. Theory*, 36(11-12):1215–1239, November 2001. doi: 10.1016/s0094-114x(01)00048-9.

[24] Morris R. Driels and Uday S. Pathre. Significance of observation strategy on the design of robot calibration experiments. *Journal of Robotic Systems*, 7(2):197–223, April 1990. doi: 10.1002/rob.4620070206.

[25] D. J. Bennett and J. M. Hollerbach. Autonomous calibration of single-loop closed kinematic chains formed by manipulators with passive endpoint constraints. *IEEE Trans. Robot. Automation*, 7(5): 597–606, October 1991. doi: 10.1109/70.97871.

[26] M. Ikits and J.M. Hollerbach. Kinematic calibration using a plane constraint. In *Proc. IEEE Int. Conf. Robot. Autom.* IEEE, 1997. doi: 10.1109/robot.1997.606774.

[27] W.K. Veitschegger and C.-H. Wu. Robot calibration and compensation. *IEEE J. Robot. Autom.*, 4 (6):643–656, 1988. doi: 10.1109/56.9302.

[28] Bruno Siciliano and Oussama Khatib. *Springer Handbook of Robotics*. Springer, Berlin, second edition, 2008. ISBN 9783540239574.

[29] V. E. Gough. Universal tyre test machine. *Proc. FISITA 9th Int. Technical Congr., London, 1962*, pages 117–137, 1962.

[30] D. Stewart. A platform with six degrees of freedom. *Proc. Inst. Mech. Eng.*, 180(1):371–386, August 1965. ISSN 0020-3483. doi: 10.1243/pime_proc_1965_180_029_02. URL https://doi.org/10.1243/PIME_PROC_1965_180_029_02.

[31] Ka C. Cheok, James L. Overholt, and Ronald R. Beck. Exact methods for determining the kinematics of a stewart platform using additional displacement sensors. *J. Robotic Syst.*, 10(5):689–707, August 1992. ISSN 0741-2223. doi: 10.1002/rob.4620100508. URL https://doi.org/10.1002/rob.4620100508.

[32] K. Liu, J. M. Fitzgerald, and F. L. Lewis. Kinematic analysis of a stewart platform manipulator. *IEEE Trans. Ind. Electron.*, 40(2):282–293, April 1993. ISSN 0278-0046. doi: 10.1109/41.222651.

[33] O. Masory, J. Wang, and H. Zhuang. On the accuracy of a stewart platform. ii. kinematic calibration and compensation. In *Proc. IEEE Int. Conf. Robot. Autom.*, pages 725–731 vol.1, May 1993. doi: 10.1109/ROBOT.1993.292064.

[34] Hanqi Zhuang, Jiahua Yan, and Oren Masory. Calibration of stewart platforms and other parallel manipulators by minimizing inverse kinematic residuals. *J. Robot. Syst.*, 15(7):395–405, 1998. doi: 10.1002/(sici)1097-4563(199807)15:7⟨395::aid-rob2⟩3.0.co;2-h.

[35] Se-Kyong Song and Dong-Soo Kwon. Efficient formulation approach for the forward kinematics of 3-6 parallel mechanisms. *Adv. Rob.*, 16(2):191–215, January 2002. ISSN 0169-1864. doi: 10.1163/156855302760064237. URL https://doi.org/10.1163/156855302760064237.

[36] L. Ren, Z. Feng, and J. K. Mills. A self-tuning iterative calculation approach for the forward kinematics of a stewart-gough platform. In *Int. Conf. Mechatron. Autom.*, pages 2018–2023, June 2006. doi: 10.1109/ICMA.2006.257583.

[37] Marcel Verner, Fengfeng Xi, and Chris Mechefske. Optimal calibration of parallel kinematic machines. *J. Mech. Des.*, 127(1):62–69, January 2005. doi: 10.1115/1.1828461.

[38] Hanqi Zhuang and Zvi S. Roth. Method for kinematic calibration of stewart platforms. *J. Robot. Syst.*, 10(3):391–405, 1993. doi: 10.1002/rob.4620100306. URL https://onlinelibrary.wiley.com/doi/abs/10.1002/rob.4620100306.

[39] Hanqi Zhuang and Lixin Liu. Self-calibration of a class of parallel manipulators. In *Proc. IEEE Int. Conf. Robot. Autom.* IEEE, 1996. doi: 10.1109/robot.1996.506838.

[40] Rene Mayer and Matthieu P. Oliviers. Global kinematic calibration of a stewart platform. In *Proc. ASME Dyn. Syst. Control Div.*, volume 57, January 1995.

[41] Kok-Soon Chai, Ken Young, and Ian Tuersley. A practical calibration process using partial information for a commercial stewart platform. *Robotica*, 20(3):315–322, May 2002. doi: 10.1017/s0263574701004027.

[42] Gao Meng, Li Tiemin, and Yin Wensheng. Calibration method and experiment of stewart platform using a laser tracker. In *Proc. IEEE Int. Conf. Syst. Man. Cybern.*, volume 3, pages 2797–2802 vol.3, October 2003. doi: 10.1109/ICSMC.2003.1244309.

[43] Lucas Campos, Francis Bourbonnais, Ilian A. Bonev, and Pascal Bigras. Development of a five-bar parallel robot with large workspace. In *Volume 2: 34th Annual Mechanisms and Robotics Conference, Parts A and B*. ASMEDC, January 2010. doi: 10.1115/detc2010-28962.

[44] L. Ghorbani and V. E. Omurlu. Forward kinematics of a 6x6 upu parallel mechanism by anfis method. In *Int. Conf. Control Eng. Inf. Technol. (CEIT)*, pages 1–6, October 2018. doi: 10.1109/CEIT.2018.8751887.

[45] Claire Dumas, Stéphane Caro, Sébastien Garnier, and Benoît Furet. Joint stiffness identification of six-revolute industrial serial robots. *Robotics and Computer-Integrated Manufacturing*, 27(4):881–888, August 2011. doi: 10.1016/j.rcim.2011.02.003.

[46] Michael Ruderman, Torsten Bertram, and Makoto Iwasaki. Modeling, observation, and control of hysteresis torsion in elastic robot joints. *Mechatronics*, 24(5):407–415, August 2014. doi: 10.1016/j.mechatronics.2014.02.009.

[47] Yingjie Guo, Huiyue Dong, and Yinglin Ke. Stiffness-oriented posture optimization in robotic machining applications. *Robotics and Computer-Integrated Manufacturing*, 35:69–76, October 2015. doi: 10.1016/j.rcim.2015.02.006.

[48] Alexandr Klimchik, Benoit Furet, Stéphane Caro, and Anatol Pashkevich. Identification of the manipulator stiffness model parameters in industrial environment. *Mechanism and Machine Theory*, 90:1–22, August 2015. doi: 10.1016/j.mechmachtheory.2015.03.002.

[49] Jorge Santolaria, José-Antonio Yagüe, Roberto Jiménez, and Juan-José Aguilar. Calibration-based thermal error model for articulated arm coordinate measuring machines. *Precision Engineering*, 33 (4):476–485, October 2009. doi: 10.1016/j.precisioneng.2009.01.002.

[50] Emanuele Lubrano and Reymond Clavel. Thermal calibration of a 3 DOF ultra high-precision robot operating in industrial environment. In *2010 IEEE International Conference on Robotics and Automation*. IEEE, May 2010. doi: 10.1109/robot.2010.5509279.

[51] Rui Li and Yang Zhao. Dynamic error compensation for industrial robot based on thermal effect model. *Measurement*, 88:113–120, June 2016. doi: 10.1016/j.measurement.2016.02.038.

[52] Jean-Michel Renders, Eric Rossignol, Marc Becquet, Raymond Hanus, et al. Kinematic calibration and geometrical parameter identification for robots. *IEEE Trans. Robot. Autom.*, 7(6):721–732, 1991.

[53] Wang Jian and Masory Oren. On the accuracy of a stewart platform—part i: The effect of manufacturing tolerances. In *IEEE Int. Conf. Robot. Autom.*, pages 114–120, 1993.

[54] DE Whitney, CA Lozinski, and Johnathan M Rourke. Industrial robot forward calibration method and results. *J. Dyn. Syst. Meas. Control*, 1986.

[55] Jigien Chen and Lih-Ming Chao. Positioning error analysis for robot manipulators with all rotary joints. *IEEE J. Robot. Autom.*, 3(6):539–545, 1987.

[56] Chris Lightcap, Samuel Hamner, Tony Schmitz, and Scott Banks. Improved positioning accuracy of the pa10-6ce robot with geometric and flexibility calibration. *IEEE Trans. Robot.*, 24(2):452–456, 2008.

[57] Joshua A. Gordon and Steven S. Borenstein. An invisible-stylus-based coordinate measurement system via scaled orthographic projection. *Precis. Eng.*, 56:211–222, March 2019. doi: 10.1016/j.precisioneng.2018.12.002.

[58] Michael S Allman, D Novotny, Joshua Gordon, Alex Curtin, and S Sandwidth. Serial robotic arm joint characterization measurements for antenna metrology. *AMTA 2017 Proceedings*, pages 381–387, 2017.

[59] Bala Muralikrishnan, Steve Phillips, and Daniel Sawyer. Laser trackers for large-scale dimensional metrology: A review. *Precis. Eng.*, 44:13–28, 2016.

[60] Jorge Santolaria and Manuel Ginés. Uncertainty estimation in robot kinematic calibration. *Robotics and Computer-Integrated Manufacturing*, 29(2):370–384, April 2013. doi: 10.1016/j.rcim.2012.09.007.

[61] J. J. Uicker, J. Denavit, and R. S. Hartenberg. An iterative method for the displacement analysis of spatial mechanisms. *Journal of Applied Mechanics*, 31(2):309–314, June 1964. doi: 10.1115/1.3629602.

[62] Patrick Beeson and Barrett Ames. TRAC-IK: An open-source library for improved solving of generic inverse kinematics. In *2015 IEEE-RAS 15th International Conference on Humanoid Robots (Humanoids)*. IEEE, November 2015. doi: 10.1109/humanoids.2015.7363472.

[63] Neil T Dantam. Robust and efficient forward, differential, and inverse kinematics using dual quaternions. *The International Journal of Robotics Research*, 40(10-11):1087–1105, July 2020. doi: 10.1177/0278364920931948.

[64] Stefano Chiaverini, Giuseppe Oriolo, and Anthony A. Maciejewski. Redundant robots. In *Springer Handbook of Robotics*, pages 221–242. Springer International Publishing, 2016. doi: 10.1007/978-3-319-32552-1_10.

[65] A. Liégeois. Automatic supervisory control of the configuration and behavior of multibody mechanisms. *IEEE Transactions on Systems, Man, and Cybernetics*, 7(12):868–871, 1977. doi: 10.1109/tsmc.1977.4309644.

[66] Yoshihiko Nakamura and Hideo Hanafusa. Optimal redundancy control of robot manipulators. *The International Journal of Robotics Research*, 6(1):32–42, March 1987. doi: 10.1177/027836498700600103.

[67] Bruno Siciliano. Kinematic control of redundant robot manipulators: A tutorial. *Journal of Intelligent and Robotic Systems*, 3(3):201–212, 1990. doi: 10.1007/bf00126069.

[68] Adrien Escande, Nicolas Mansard, and Pierre-Brice Wieber. Fast resolution of hierarchized inverse kinematics with inequality constraints. In *2010 IEEE International Conference on Robotics and Automation*. IEEE, May 2010. doi: 10.1109/robot.2010.5509953.

[69] Oussama Kanoun, Florent Lamiraux, and Pierre-Brice Wieber. Kinematic control of redundant manipulators: Generalizing the task-priority framework to inequality task. *IEEE Transactions on Robotics*, 27(4):785–792, August 2011. doi: 10.1109/tro.2011.2142450.

[70] Adrien Escande, Nicolas Mansard, and Pierre-Brice Wieber. Hierarchical quadratic programming: Fast online humanoid-robot motion generation. *The International Journal of Robotics Research*, 33 (7):1006–1028, May 2014. doi: 10.1177/0278364914521306.

[71] Luis Sentis and Oussama Khatib. Synthesis of whole-body behaviors through hierarchical control of behavioral primitives. *International Journal of Humanoid Robotics*, 2(04):505–518, 2005.

[72] Martin de Lasa, Igor Mordatch, and Aaron Hertzmann. Feature-based locomotion controllers. *ACM Transactions on Graphics*, 29(4):1–10, July 2010. doi: 10.1145/1778765.1781157.

[73] James J Kuffner and Steven M LaValle. Rrt-connect: An efficient approach to single-query path planning. In *Proceedings 2000 ICRA. Millennium Conference. IEEE International Conference on Robotics and Automation. Symposia Proceedings (Cat. No. 00CH37065)*, volume 2, pages 995–1001. IEEE, 2000.

[74] Sertac Karaman and Emilio Frazzoli. Sampling-based algorithms for optimal motion planning. *The international journal of robotics research*, 30(7):846–894, 2011.

[75] Zachary Kingston, Mark Moll, and Lydia E. Kavraki. Sampling-based methods for motion planning with constraints. *Annual Review of Control, Robotics, and Autonomous Systems*, 1(1):159–185, May 2018. doi: 10.1146/annurev-control-060117-105226.

[76] Todd W. Danko, Kenneth P. Chaney, and Paul Y. Oh. A parallel manipulator for mobile manipulating UAVs. In *IEEE Int. Conf. Technol. Pract. Robot Appl. (TePRA)*. IEEE, May 2015. doi: 10.1109/tepra.2015.7219682.

[77] Ha si-ao-qi-er Han, Chun-Yang Han, Zhen-Bang Xu, Ming-Chao Zhu, Yang Yu, and Qing-Wen Wu. Kinematics analysis and testing of novel 6-p-RR-r-RR parallel platform with offset RR-joints. *Proc. Inst. Mech. Eng. C: J. Mech. Eng. Sci.*, 233(10):3512–3530, December 2018. doi: 10.1177/0954406218817001.

[78] Tanio K. Tanev. Kinematics of a hybrid (parallel-serial) robot manipulator. *Mech. Mach. Theory*, 35 (9):1183 – 1196, 2000. ISSN 0094-114X. doi: https://doi.org/10.1016/S0094-114X(99)00073-7. URL http://www.sciencedirect.com/science/article/pii/S0094114X99000737.

[79] Serdar Kucuk and Baris Doruk Gungor. Inverse kinematics solution of a new hybrid robot manipulator proposed for medical purposes. IEEE, October 2016. doi: 10.1109/tiptekno.2016.7863076.

[80] Rainer Gloess and Brian Lula. Challenges of extreme load hexapod design and modularization for large ground-based telescopes. In *SPIE Proceedings*. SPIE, July 2010. doi: 10.1117/12.858156.

[81] Charles W. Wampler. Forward displacement analysis of general six-in-parallel sps (stewart) platform manipulators using soma coordinates. *Mech. Mach. Theory*, 31(3):331 – 337, 1996. ISSN 0094-114X. doi: https://doi.org/10.1016/0094-114X(95)00068-A. URL http://www.sciencedirect.com/science/article/pii/0094114X9500068A.

[82] J. Merlet. Direct kinematics of parallel manipulators. *IEEE Trans. Robot. Autom.*, 9(6):842–846, December 1993. ISSN 1042-296X. doi: 10.1109/70.265928.

[83] P. R. McAree and R. W. Daniel. A fast, robust solution to the stewart platform forward kinematics. *J. Robot. Syst.*, 13(7), 1996.

[84] Louis J. Everett. Forward calibration of closed-loop jointed manipulators. *Int. J. Robot. Res.*, 8(4): 85–91, August 1989. doi: 10.1177/027836498900800405.

[85] Stefan Staicu. Dynamics of the 6-6 stewart parallel manipulator. *Robot. Comput.-Integr. Manuf.*, 27 (1):212–220, February 2011. doi: 10.1016/j.rcim.2010.07.011.

[86] Arkadeep Narayan Chaudhury and Ashitava Ghosal. Optimum design of multi-degree-of-freedom closed-loop mechanisms and parallel manipulators for a prescribed workspace using monte carlo method. *Mech. Mach. Theory*, 118:115–138, December 2017. doi: 10.1016/j.mechmachtheory.2017.07.021.

[87] W. Khalil and S. Besnard. Self calibration of stewart-gough parallel robots without extra sensors. *IEEE Trans. Robot. Autom.*, 15(6):1116–1121, 1999. doi: 10.1109/70.817674.

[88] J.M. Hollerbach and D.M. Lokhorst. Closed-loop kinematic calibration of the RSI 6-DOF hand controller. *IEEE Trans. Robot. Autom.*, 11(3):352–359, June 1995. doi: 10.1109/70.388777.

[89] C. W. Wampler, J.M. Hollerbach, and T. Arai. An implicit loop method for kinematic calibration and its application to closed-chain mechanisms. *IEEE Trans. Robot. Autom.*, 11(5):710–724, 1995. doi: 10.1109/70.466613.

[90] Chunyang Han, Yang Yu, Zhenbang Xu, Xiaoming Wang, Peng Yu, and Xiaoqin Zhou. Complete kinematic calibration of a 6-RRRPRR parallel kinematic machine based on the optimal measurement configurations. *Proc. Inst. Mech. Eng. C: J. Mech. Eng. Sci.*, 234(1):121–136, September 2019. doi: 10.1177/0954406219869985.

[91] Tao Sun, Binbin Lian, Shuofei Yang, and Yimin Song. Kinematic calibration of serial and parallel robots based on finite and instantaneous screw theory. *IEEE Trans. Robot.*, 36(3):816–834, June 2020. doi: 10.1109/tro.2020.2969028.

[92] S. Ibaraki, T. Yokawa, Y. Kakino, M. Nakagawa, and T. Matsushita. Kinematic calibration on a parallel kinematic machine tool of the stewart platform by circular tests. In *Proc. 2004 Am. Control Conf.* IEEE, 2004. doi: 10.23919/acc.2004.1386770.

[93] Jia-Feng Wu, Rui Zhang, Rui-He Wang, and Ying-Xue Yao. A systematic optimization approach for the calibration of parallel kinematics machine tools by a laser tracker. *Int. J. Mach. Tools Manuf.*, 86:1–11, November 2014. doi: 10.1016/j.ijmachtools.2014.06.003.

[94] Tao Sun, Yapu Zhai, Yimin Song, and Jiateng Zhang. Kinematic calibration of a 3-DoF rotational parallel manipulator using laser tracker. *Robot. Comp.-Integr. Man.*, 41:78–91, October 2016. doi: 10.1016/j.rcim.2016.02.008.

[95] Yimin Song, Jiateng Zhang, Binbin Lian, and Tao Sun. Kinematic calibration of a 5-DoF parallel kinematic machine. *Precis. Eng.*, 45:242–261, July 2016. doi: 10.1016/j.precisioneng.2016.03.002.

[96] Peng Huang, Jinsong Wang, Liping Wang, and Rui Yao. Kinematical calibration of a hybrid machine tool with regularization method. *Int. J. Mach. Tools Manuf.*, 51(3):210–220, March 2011. doi: 10.1016/j.ijmachtools.2010.11.009.

[97] Yuzhe Liu, Jun Wu, Liping Wang, and Jinsong Wang. Parameter identification algorithm of kinematic calibration in parallel manipulators. *Adv. Mech. Eng.*, 8(9):168781401666790, September 2016. doi: 10.1177/1687814016667908.

[98] Genliang Chen, Lingyu Kong, Qinchuan Li, Hao Wang, and Zhongqin Lin. Complete, minimal and continuous error models for the kinematic calibration of parallel manipulators based on POE formula. *Mech. Mach. Theory*, 121:844–856, March 2018. doi: 10.1016/j.mechmachtheory.2017.11.003.

[99] Bernhard Jokiel, John C. Ziegert, and Lothar Bieg. Uncertainty propagation in calibration of parallel kinematic machines. *Precision Engineering*, 25(1):48–55, January 2001. doi: 10.1016/s0141-6359(00)00055-6.

[100] Richard M. Murray, Zexiang Li, and S. Shankar Sastry. *A Mathematical Introduction to Robotic Manipulation*. CRC Press, December 1994. doi: 10.1201/9781315136370.

[101] Jan Magnus. *Matrix differential calculus with applications in statistics and econometrics*. John Wiley & Sons, Inc, Hoboken, NJ, 2019. ISBN 9781119541202.

[102] John Hollerbach, Wisama Khalil, and Maxime Gautier. *Springer Handbook of Robotics*, chapter Model Identification, pages 321–344. Springer, second edition, 2008.

[103] Kenneth Levenberg. A method for the solution of certain non-linear problems in least squares. *Q. Appl. Math.*, 2(2):164–168, July 1944. doi: 10.1090/qam/10666.

[104] Joseph-Frédéric Bonnans, Jean Charles Gilbert, Claude Lemarechal, and Claudia A. Sagastizábal. *Numerical Optimization: Theoretical and Practical Aspects*. Springer Berlin Heidelberg, September 2006. ISBN 354035445X. URL https://www.ebook.de/de/product/5741326/joseph_frederic_bonnans_jean_charles_gilbert_claude_lemarechal_claudia_a_sagastizabal_numerical_optimization.html.

[105] M. Raghavan. The stewart platform of general geometry has 40 configurations. *J. Mech. Des.*, 115 (2):277–282, June 1993. doi: 10.1115/1.2919188.

[106] Kenneth Hoffman and Ray Kunze. *Linear algebra*. Prentice-Hall, Englewood Cliffs, NJ, second edition, 1971. ISBN 9780135367971.

[107] Bruno Siciliano, Lorenzo Sciavicco, Luigi Villani, and Giuseppe Oriolo. *Robotics: Modelling, Planning and Control*. Springer London, October 2010. ISBN 1849966346. URL https://www.ebook.de/de/product/13994410/giuseppe_oriolo_lorenzo_sciavicco_bruno_siciliano_luigi_villani_robotics.html.

[108] Barry N. Taylor and Chris E. Kuyatt. Guidelines for evaluating and expressing the uncertainty of nist measurement results. *NIST Technical Note 1297*, 1994.

[109] J. Wang and O. Masory. On the accuracy of a stewart platform. i. the effect of manufacturing tolerances. Proc. IEEE Int. Conf. Robot. Autom., 1993. doi: 10.1109/robot.1993.291970.

[110] John Wishart. The generalised product moment distribution in samples from a normal multivariate population. *Biometrika*, 20A(1-2):32–52, 1928. doi: 10.1093/biomet/20a.1-2.32.

[111] Klaus Schröer. *Robot Calibration*, chapter Theory of kinematic modelling and numerical procedures for robot calibration, pages 157–196. Chapman & Hall, 1993.

[112] Hexagon Manufacturing. *Leica Absolute Tracker AT960 Data Sheet*. Cedar House, 78 Portsmouth Road Cobham, Surrey KT11 1AN United Kingdom, 2016.

[113] K.S. Arun, T.S. Huang, and Steven Blostein. Least-squares fitting of two 3-d point sets. *IEEE Trans. Pattern Anal. Mach. Intell.*, PAMI-9:698 – 700, October 1987. doi: 10.1109/TPAMI.1987.4767965.

[114] Tian Huang, Dong Zhao, Fuwen Yin, Wenjie Tian, and Derek G. Chetwynd. Kinematic calibration of a 6-DOF hybrid robot by considering multicollinearity in the identification jacobian. *Mech. Mach. Theory*, 131:371–384, January 2019. doi: 10.1016/j.mechmachtheory.2018.10.008.

[115] Arthur P Dempster, Nan M Laird, and Donald B Rubin. Maximum likelihood from incomplete data via the em algorithm. *J. R. Statist. Soc. B*, 39(1):1–22, January 1977.

[116] M.D. Shuster, J.L. Junkins, and American Astronautical Society. *A Survey of Attitude Representations*. Journal of the astronautical sciences. American Astronautical Society, 1993. URL https://books.google.com/books?id=kIznZwEACAAJ.

[117] Benjamin L. Moser, Joshua A. Gordon, and Andrew J. Petruska. Unified parameterization and calibration of serial, parallel, and hybrid manipulators. *Robotics*, 10(4):124, November 2021. doi: 10.3390/robotics10040124.

[118] ISO. Iso/iec guide 98-3:2008/suppl 1:2008 uncertainty of measurement — part 3: Guide to the expression of uncertainty in measurement (gum:1995) — supplement 1: Propagation of distributions using a monte carlo method, November 2008.

[119] Martin A. Fischler and Robert C. Bolles. Random sample consensus. *Communications of the ACM*, 24(6):381–395, June 1981. doi: 10.1145/358669.358692.

[120] Charles L. Lawson and Richard J. Hanson. *Solving Least Square Problems*. Society for Industrial and Applied Mathematics, January 1995. ISBN 0898713560. URL https://www.ebook.de/de/product/7285518/charles_l_lawson_richard_j_hanson_solving_least_square_problems.html.

[121] A. N. Pettitt. A two-sample anderson-darling rank statistic. *Biometrika*, 63(1):161–168, 1976. doi: 10.1093/biomet/63.1.161.

[122] NSI-MI Technologies. *8-Axis Robotic Antenna Measurement System Data Sheet*. 1125 Satellite Blvd. NW,Ste. 100 Suwanee, GA 30024 USA, 2018.

[123] R. Moch and D. Heberling. Fast spline-based antenna measurements for robotic test ranges via pointwise probe correction. In *2022 16th European Conference on Antennas and Propagation (EuCAP)*. IEEE, March 2022. doi: 10.23919/eucap53622.2022.9769401.

[124] TJAK Tarn, A Bejczy, and Xiaoping Yun. Design of dynamic control of two cooperating robot arms: Closed chain formulation. In *Proceedings. 1987 IEEE International Conference on Robotics and Automation*, volume 4, pages 7–13. IEEE, Institute of Electrical and Electronics Engineers, 1987. doi: 10.1109/robot.1987.1088028.

[125] Alessandro Roncone, Matej Hoffmann, Ugo Pattacini, and Giorgio Metta. Automatic kinematic chain calibration using artificial skin: Self-touch in the iCub humanoid robot. In *2014 IEEE International Conference on Robotics and Automation (ICRA)*. IEEE, May 2014. doi: 10.1109/icra.2014.6907178.

[126] Daniel Rakita, Bilge Mutlu, and Michael Gleicher. Relaxedik: Real-time synthesis of accurate and feasible robot arm motion. In *Proceedings of Robotics: Science and Systems*, Pittsburgh, Pennsylvania, June 2018. doi: 10.15607/RSS.2018.XIV.043.

[127] Gregory Gutin and Abraham P Punnen. *The traveling salesman problem and its variations*, volume 12. Springer Science & Business Media, 2006.

[128] S. Lin and B. W. Kernighan. An effective heuristic algorithm for the traveling-salesman problem. *Operations Research*, 21(2):498–516, April 1973. doi: 10.1287/opre.21.2.498.

[129] Keld Helsgaun. An effective implementation of the lin–kernighan traveling salesman heuristic. *European Journal of Operational Research*, 126(1):106–130, October 2000. doi: 10.1016/s0377-2217(99)00284-2.

[130] Keld Helsgaun. General k-opt submoves for the lin–kernighan TSP heuristic. *Mathematical Programming Computation*, 1(2-3):119–163, July 2009. doi: 10.1007/s12532-009-0004-6.

[131] The MathWorks Inc. fmincon, optimization toolbox version: 9.3 (r2022a), 2022. URL https://www.mathworks.com.

[132] C. Culotta-Lopez, R. Moch, R. Wilke, and D. Heberling. On the influence of probe positioning errors due to mechanical uncertainties in spherical near-field measurements at terahertz frequencies in modern positioner systems. In *2019 PhotonIcs &amp Electromagnetics Research Symposium - Spring (PIERS-Spring)*. IEEE, June 2019. doi: 10.1109/piers-spring46901.2019.9017778.

APPENDIX A

RECURSIVE ANALYSIS OF COMPLEX MECHANISMS

The kinematics and calibration techniques for hybrid manipulators described in Chapter 2 can be extended to complex manipulator designs that include nested parallel components. We visualize an example implementation to demonstrate this process and facilitate integration.

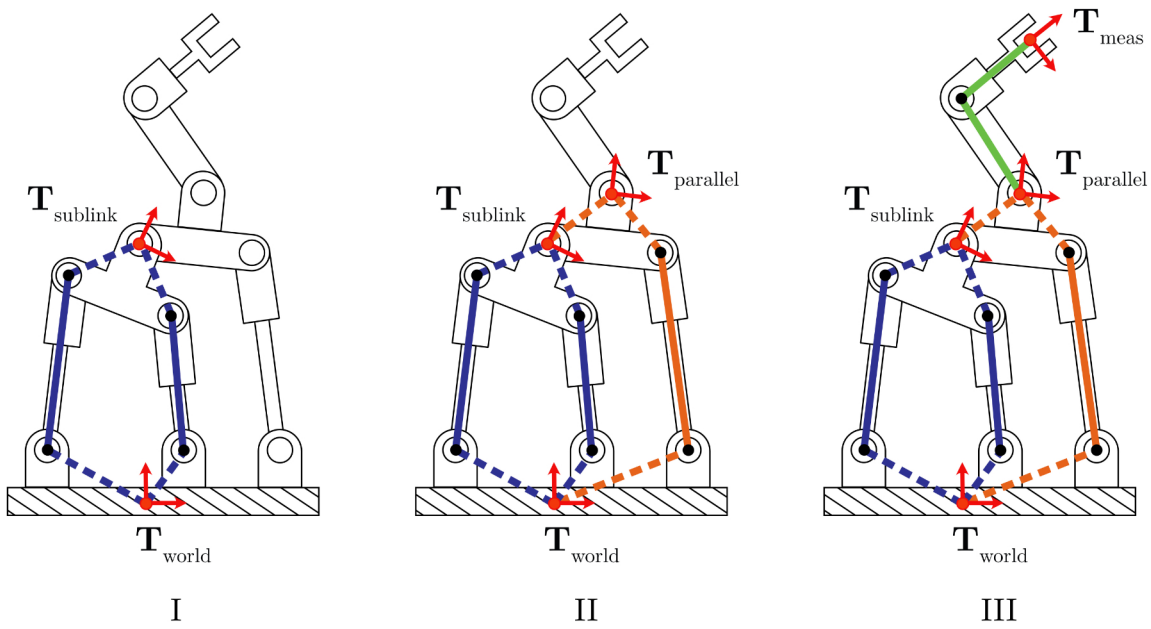

Figure A.1 Vidual representation of the analysis of complex manipulator cases. By identifying and evaluating low-level parallel components (I), serial-equivalent representations of these components can be used to facilitate analysis of nested parallel structures (II). Additional manipulator links added to the distal or proximal ends of the manipulator are evaluated in standard serial fashion (III).

Viewing Figure A.1, analysis of the manipulator begins by evaluating the simple parallel components forming closed kinematic loop. This subsection can be represented as a complete parallel manipulator to facilitate Jacobian generation at the current pose. Our implementation permits this substructure to be viewed as a serial-equivalent "parallel link" for the purposes of modular kinematics and calibration. Parallel links formed by the substructures can be used in the construction of larger parallel links, with the process continuing until the mechanism is described. Other serial or parallel links can be attached at the distal or proximal ends of the manipulator and are evaluated as a standard serial kinematic chain.

APPENDIX B

ROBOTIC ANTENNA RANGE CONTROL

A LabView control framework was implemented to provide a unified method to interface with the various robotic antenna range components and provide a source of unified measurement collection. The user interface is displayed in Figure B.1, and is designed for modular integration and operation with all NIST robotic antenna ranges.

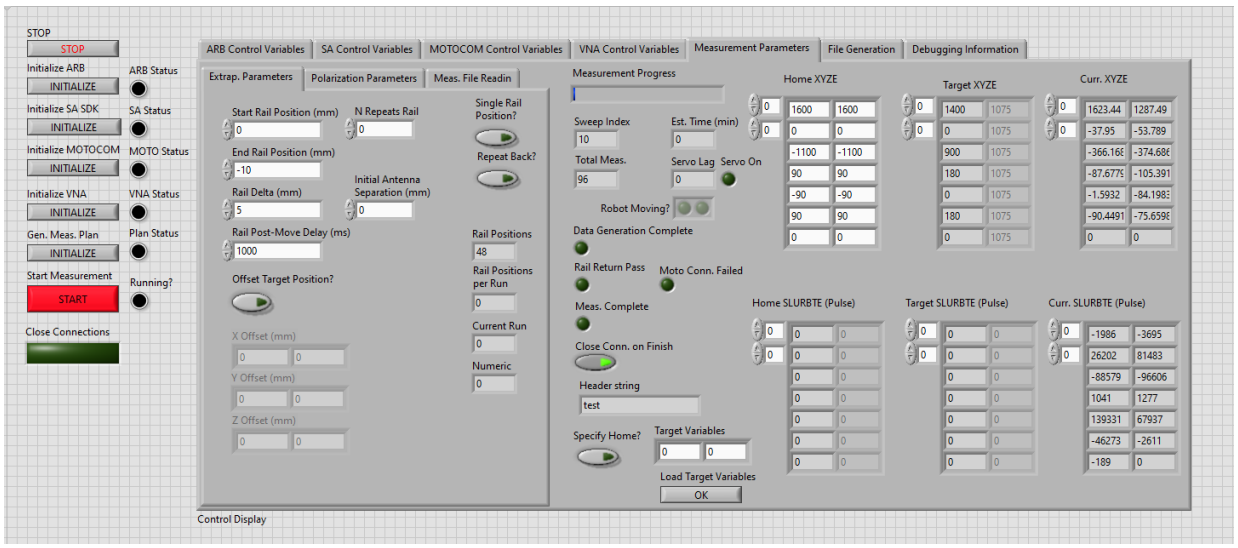

Figure B.1 Screen capture of the front panel of the LabView unified robotics antenna range control program.

Connections and control of robotic manipulators and antenna metrology equipment, such as VNAs, are made via SDK integration. The current version of this software supports the integrated generation of standard antenna range patterns, but relies on external MATLAB code to generate the hierarchical inverse kinematics solutions described in Chapter 4. System architecture is displayed in Figure B.2.

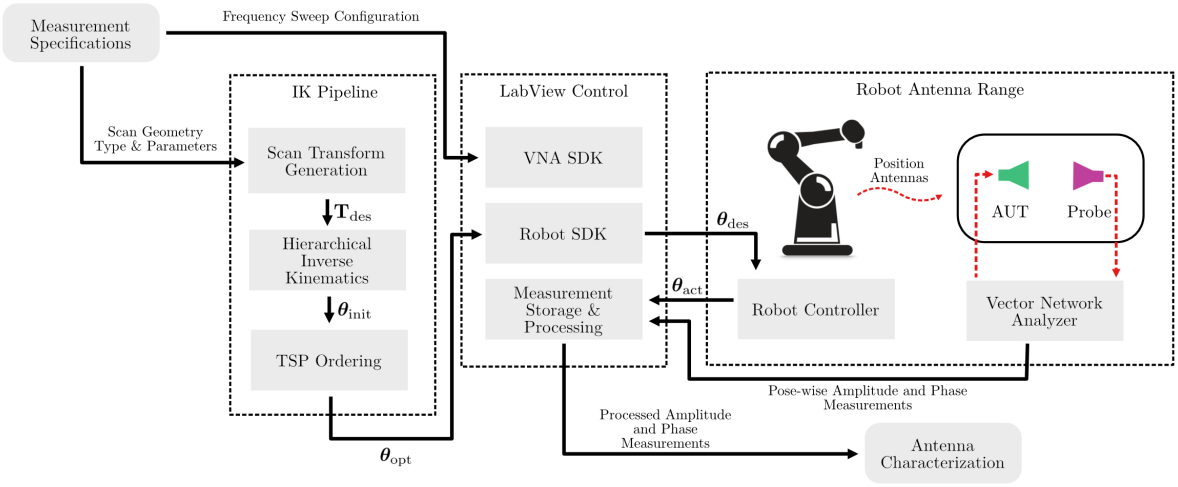

Figure B.2 Robotic antenna range control architecture. The LabView interface permits user control of critical components of the antenna range in a unified manner by integrating equipment SDKs.